Large-Scale Simulation of Modern Electric Power Systems

A Dissertation Presented for the

Doctor of Philosophy

Degree

The University of Tennessee, Knoxville

Hantao Cui

December 2018

© by Hantao Cui, 2018
All Rights Reserved.

Acknowledgements

Upon the completion of my dissertation and Ph.D. study, I would like to express my gratitude to those who have guided, helped and supported me during the past five years.

First, I would like to thank my advisor, Dr. Fangxing Li, with the deepest gratitude for his long-lasting guidance and persistent support. During the past five years, Dr. Li has continuously guided me through forming research ideas, developing research software, writing technical papers, and preparing this dissertation. I will always be grateful to Dr. Li for empowering me.

My sincere thanks go to Dr. Tomsovic, Dr. Yilu Liu and Dr. Mingzhou Jin for their time and efforts serving on my dissertation committee.

My special thanks also go to Dr. Yichen Zhang, Dr. Xin Fang, Dr. Qinran Hu, Dr. Xue Li, Dr. Linquan Bai, Dr. Haoyu Yuan, and Dr. Riyasat Azim for the countless times we discussed research topics. I would also like to thank Kellen Oleksak, Alec Yen, and Runsha Long for their contributions as undergraduate researchers.

I'm also grateful for all the faculty, staff, and students at the Center for Ultra-wide-area Resilient Electric Energy Transmission Networks (CURENT) for having an open and inclusive workplace culture. I am also grateful for being offered my first job at CURENT, years before my graduation, as a full-time research associate.

Finally, I owe my deepest gratitude to my parents, my girlfriend, Chen Xu, and my family. Their endless support made the completion of my Ph.D. study possible.

It is especially nice when the things we regard as beautiful are also regarded by other people as useful.

– Donald Knuth

Abstract

Computer simulation techniques are essential to electric power system studies to reduce risks and improve reliability. Modern power systems are undergoing significant changes with better monitoring and communication capabilities, higher levels of renewable penetration, and a considerable number of connected power electronics devices. There arises a pressing need for a testbed with structural and functional representations of modern power systems, including wide-area measurement, energy management, communication, and measurement-based control.

The topic of the dissertation, Large-Scale Simulation of Modern Electric Power Systems, is broad. This dissertation will cover two aspects of the topic. The first aspect is the design and implementation of a communication network enabled large-scale testbed (LTB) for wide-area measurement-based control verification. The second aspect is the modeling and control of voltage source converter (VSC) based multi-terminal dc (MTDC) networks.

In detail, the LTB section introduces the concepts and techniques that are being used in the current implementation. A proposal of a cyber-physical system (CPS) design for the next-generation LTB follows. The VSC MT-HVDC part covers a) the steady-state power flow analysis of ac/dc hybrid systems, b) positive-sequence transient dynamics models of VSC with inertia emulation and frequency response capability, and c) an application of multi-terminal dc for integrating offshore wind generation with inertial and frequency support.

The outcome in the testbed section includes an implementation of the CURENT LTB. A decoupled architecture enabled by distributed messaging environment allows for building up a simulation environment with modules for simulation, communication, energy management, and wide-area control. The LTB also features module interchangeability by adopting a unified communication format that makes the modules agnostic of each other. The testbed has successfully demonstrated state estimations, frequency control and damping control on the CURENT test systems.

In the VSC-based MTDC modeling section, the power flow model is able to handle systems with more than 10,000 buses at a calculation speed faster than MATLAB-based open-source packages. The transient models of the VSCs and the dc network demonstrate power transfer capability for inertial response and frequency control in a single grid and a multi-area grid with offshore wind generations.

Table of Contents

1 Introduction **1**

1.1 Background 1

1.2 Trends and Emerging Technologies in Modern Power Systems 2

1.3 Classical and Emerging Techniques for Power System Simulation . . . 4

1.4 Advances in Computer Simulation Techniques 6

1.5 Cyber-Physical Power System Simulations 9

1.6 Challenges of Modeling and Simulation of Large-Scale Power Electronics Interfaced Systems 11

1.7 Scope of this Dissertation 13

2 Large-Scale Testbed Design and Implementation **15**

2.1 Motivations and Goals 15

2.2 Overview of the Implemented LTB Platform 16

2.3 Design of Cyber-Physical Testbed for Power System Wide-Area Measurement-Based Control Using Open-Source Software 20

2.3.1 Decoupled Framework 21

2.3.2 Power Grid Simulator 22

2.3.3 Software-Defined Network Emulator 23

2.3.4 EMS Functions 24

2.3.5 Control Functions 25

2.4 Open-Source Implementation of CPS LTB 26

2.4.1 Decoupled Design . . . 26
2.4.2 Power Grid Simulator . . . 27
2.4.3 Software-Defined Network Emulator . . . 28
2.4.4 EMS Functions . . . 28
2.4.5 Control Functions . . . 29
2.5 Case Studies . . . 30
2.5.1 System Separation Control . . . 31
2.5.2 Hierarchical Voltage Control . . . 33
2.6 Remarks on this Chapter . . . 34

3 High Voltage Direct Current Transmission Systems 35
3.1 DC Network Model . . . 35
3.1.1 DC Nodes . . . 36
3.1.2 DC Device Abstraction . . . 36
3.2 Generalized VSC MT-HVDC Model . . . 37
3.2.1 VSC MT-HVDC Equivalent Circuit . . . 37
3.2.2 VSC MT-HVDC Power Flow Equations . . . 38
3.2.3 Voltage and Power Flow Control of Converters . . . 41
3.2.4 Summary of VSC Power Flow Model . . . 42
3.3 Formulating into Newton Power Flow . . . 43
3.3.1 Newton Method with Automatic Reactive Power Limit . . . 43
3.3.2 Incorporation of VSC MT-HVDC Model . . . 45
3.3.3 Automatic VSC Control and Limit Enforcing . . . 46
3.4 Case Studies and Results . . . 47
3.4.1 IEEE 14-Bus System . . . 47
3.4.2 Large Test Systems . . . 51
3.4.3 Conclusion . . . 53

4 Transient Models for VSC and MT-HVDC Networks 54
4.1 Classification of VSC-Based Interface . . . 54

4.1.1 Current-Source Controlled VSC . . . 55
4.1.2 Voltage-Source Controlled VSC . . . 56
4.2 Positive-Sequence Phasor-Domain Model . . . 57
4.2.1 Network Interfaces . . . 57
4.2.2 Current-Source Controlled VSC Modeling . . . 59
4.2.3 Voltage-Source Controlled VSC Modeling . . . 63
4.2.4 Possible Simplifications . . . 64
4.2.5 Modeling Local Frequency Control for VSC . . . 66
4.3 Dynamic Response of the Proposed Models . . . 68
4.3.1 Conclusions . . . 72

5 Provision of Emulated Inertia Through HVDC Networks 74
5.1 Modeling of Type IV Wind Generators . . . 74
5.1.1 Aerodynamics and Turbine Model . . . 75
5.1.2 Pitch Angle Control and Maximum Power Tracking . . . 75
5.1.3 Generator Model . . . 76
5.1.4 VSC Controller . . . 77
5.1.5 Inertia Emulation Control . . . 78
5.1.6 Simplified Off-Shore Wind Generators . . . 79
5.2 Inertia Emulation Controllers . . . 79
5.2.1 Local Signal Based Inertia Emulation . . . 80
5.2.2 Wide-Area Signal Based Inertia Emulation . . . 82
5.3 Provision and Allocation of Inertia Response . . . 83
5.3.1 Maximum Extractable Inertial Power . . . 84
5.3.2 Power Reduction Due to DC Voltage Drop . . . 84
5.3.3 Allocation of Inertial Power . . . 85
5.4 Case Studies . . . 87
5.4.1 Test System Setup . . . 87
5.4.2 Load Ramping in Area 2 . . . 88

5.4.3 Load Ramping in Area 1 94
5.5 Conclusion 100

6 Conclusions **101**
6.1 Main Contributions and Conclusions 101
6.2 Future Research Directions 102

Bibliography **104**

Appendix **116**

A Publications During Ph.D. Study **117**
A.1 Journal Papers 117
A.2 Conference Papers 118
A.3 Patent Applications 118

Vitae **119**

List of Tables

3.1 MT-HVDC VSC Set Points 48

3.2 Scenario 1: Base Case with $qG_2 \leq 0.4$ 48

3.3 Scenario 2: Base Case with $q_{G2} \leq 0.4$, VSC MT-HVDC Network . . . 49

3.4 Scenario 2: VSC MT-HVDC Solutions 49

3.5 Scenario 3: VSC MT-HVDC Solutions ($V_{sh3} \leq 1.05$) 50

3.6 Scenario 4: VSC MT-HVDC Solutions ($V_{sh3} \leq 1.05$ and $I_{sh4} \leq 0.15$) . 50

4.1 MT-HVDC VSC Set Points 68

List of Figures

2.1 LTB architecture overview 17
2.2 Data streaming amongst decoupled modules 18
2.3 Architecture design of the LTB incorporating power network, communication network, EMS, and control 21
2.4 Concept of the LTB for cyber-physical testing and cybersecurity studies 24
2.5 Process dispatch architecture in the proposed implementation 27
2.6 Visualization of the WECC 181-bus system frequency contour map after system separation 32
2.7 Simultaneous comparative visualization of hierarchical voltage control on the WECC 197-bus system 33

3.1 Generalized system with VSC MT-HVDC 38
3.2 AC voltage magnitude visualization for the CURENT North American System 52
3.3 Power injections on buses and VSC converter stations 52

4.1 Schematic diagram of a current-source controlled VSC connection. . . 56
4.2 Schematic diagram of a voltage-source controlled VSC connection. . . 57
4.3 VSC interface block diagram. 58
4.4 Full model of VSC interfaced to large-scale ac systems. Upper: current-source type VSC; Lower: voltage-source type VSC. 60
4.5 PLL block diagram. 61

4.6 Inertia emulation control loop for current-source VSC. 66
4.7 Inertia emulation control loop for voltage-source VSC. 67
4.8 Active power output at VSC 1 69
4.9 DC voltage at Node 1 70
4.10 Current injections at Nodes 1 and 2 71
4.11 Nodal current injections at Nodes 1 and 2 in Case 2 original parameters 71
4.12 Nodal current injections at Node 2 and the voltage profiles. Case 2´ uses modified parameters. 71
4.13 ac voltages in the dq-axis 72

5.1 Decentralized inertial power allocation controller on converter i . . . 86
5.2 Illustration of the four-area, four-terminal test system 87
5.3 VSC active power injections under local inertia emulation 88
5.4 Bus frequency under local inertia emulation 89
5.5 Bus voltage magnitude under local IE 89
5.6 WTG response characteristics under local IE 89
5.7 DC voltage at Node 1 under local IE 90
5.8 VSC active power injections under remote inertia emulation 92
5.9 Bus frequency under remote inertia emulation 92
5.10 Bus voltage magnitude under remote inertia emulation 92
5.11 WTG response characteristics under remote IE 93
5.12 DC voltage at Node 1 under remote IE 93
5.13 VSC active power injections under local inertia emulation 95
5.14 Bus frequency under remote local emulation 95
5.15 WTG response characteristics under local IE 96
5.16 DC voltage at Node 1 under local IE 96
5.17 VSC active power injections under remote inertia emulation 97
5.18 Bus frequency under remote IE 97
5.19 WTG response characteristics under remote IE 98

5.20 DC voltage at Node 1 under remote ROCOF-based IE 98
5.21 ROCOF at Bus 1-1 under Area 1 load ramping with remote ROCOF-based IE 99

Chapter 1

Introduction

1.1 Background

Every system in the universe runs on energy regardless of size. Human society, if seen as a system, is energized every time the utilization of energy advances. In ancient times, people relied on their own bodies and livestock for farm activities. The invention of the steam engine made possible energy conversion from chemical energies stored in materials to mechanical energy, and propelled the industrial revolution. The utilization of electricity further enabled the conversion from primary energy sources to electricity, which can be converted into other forms of energy conveniently.

The electric power system is the largest human-made system in terms of physical scale. Elaborate machines are designed and manufactured to generate electricity from mechanical energy stored in turbines, which are powered by primary energy sources. Transmission networks are built to enable efficient power delivery from generation centers to the broad landscape. Distribution networks are constructed to deliver power from the transmission network to households and industries. On the demand side, many apparatus and devices have been invented to transform electric energy into other forms.

Power system technologies have been evolving rapidly over the past century. In 1936, the first high voltage direct current (HVDC) transmission line was built in New York using mercury arc valves as rectifiers. In 1954, the first commercial nuclear power station was launched in Russia with an output of 5 MW. In the 1970s, solid-state devices such as the thyristor and gate turn-off thyristor became dominant in AC/DC conversions. Since the late 1980s, computer-assisted power system simulations have enabled the understanding of non-linear dynamics in large systems, allowing for the building of systems of an ever-growing size. In the last decade, the total capacity of renewable energy generation, whose concept was proposed more than a century ago, started to soar due to lowered manufacturing costs and worldwide government supports. The reliability of the power supply has been continuously improving, and the cost of electricity has been decreasing. Those trends will continue.

1.2 Trends and Emerging Technologies in Modern Power Systems

There are a few trends and promising technologies worth noticing in modern power systems. On the generation side, the price of natural gas has been driven to a historical low owing to advancements in shale gas extraction technology [18, 6]. The capacity of gas-fired generators has surpassed coal-fired ones in the United States, becoming the most significant source of electricity in the generation mix. Safety concerns and operation license expiration are causing nuclear generators, which constitute 20% of the total capacity, to retire. As a result, policymakers are paying close attention to generation adequacy and system reliability.

Renewable energy sources (RES), especially wind and photovoltaic (PV) generations, are enjoying a considerable increase in penetration level [25]. RES have low marginal costs in production but exert high volatility on the connected grid and might consequently reduce the security margin. A side effect of generator retirement and

renewables taking over the load is the reduction in system inertia, which is under heavy investigation both in the industry and in academia.

On the transmission side, the expansion of high-voltage ac transmission networks has been stagnant in the United States due to the reduced rate of demand growth. Measures to defer the construction of new lines, such as utilizing flexible AC transmission (FACT) devices, and incentivizing demand response programs [56], have been taken to postpone capital investments. Due to the geographical distribution of renewable energy resources, the need for transmitting energy over prolonged distances has been rising. High Voltage Direct Current (HVDC) transmission again emerges as a solution for wide-area energy transfer.

Modern power systems have also benefited from rapid advancements in micro-electronics and information technologies. In fact, interconnections can operate at an unprecedented scale with a narrower-than-ever stability margin largely due to modern telemetry and communication techniques. Area control centers can acquire telemetry data from the supervisory control and data acquisition (SCADA) system every few seconds. The synchrophasor initiative started in the last decade has been promoting the deployment of synchrophasors such as phasor measurement units (PMUs) and frequency disturbance recorders (FDRs). Precisely time-stamped synchrophasor measurement data are streaming into control centers for online analysis and controls. In recent years, PMU data has been applied in identifying faults, outages and inter-area oscillation in major interconnections. The use of PMU data for large-scale coordinated controls is also under research.

Finally, recent machine learning based artificial intelligence (AI) has proven its power in the Go game and computer vision. It has the potential to reshape the modern power system from short-term controls to mid-term scheduling and long-term planning. Combined with PMU data and analytical models, AI could make control decisions to minimize power outage risks, lower operating costs and create contingency plans.

1.3 Classical and Emerging Techniques for Power System Simulation

The power system dynamic models for time-domain transient simulation are described by a set of nonlinear differential algebraic equations (DAE):

$$\begin{aligned} \dot{x} &= f(x, y, \eta, u, t) \\ 0 &= g(x, y, \eta, u, t) \end{aligned} \tag{1.1}$$

The equation set includes the differential equations of devices such as generators and controllers, and network interfaces where the power devices are connected. Discrete variables u are introduced to represent discontinuous events such as switching. The equation set can be written in a quasi-linear state-space form as:

$$\dot{x} = f(x, u) = \boldsymbol{A} \cdot x + \boldsymbol{B} \cdot u \tag{1.2}$$

The goal of the transient simulation is to obtain the system trajectory after a large disturbance to examine whether the system is stable or not. There are typically two categories of solution approaches:

1. Analytical approaches based on Lyapunov's direct method, which attempts to construct a *Lyapunov's function* to infer the stability of the ODE system (1.1). Early work by [51] pointed out the difficulties of the direct methods, including characterizing the stability boundary and defining the local region of attraction around controlling unstable equilibrium points.

2. Numerical integration methods. The numerical solution of the differential equations involved is the key to computer-based power system transient simulation. The integration methods are categorized into partitioned and simultaneous methods. The partitioned method solves the differential equations and algebraic equations iteratively, while the simultaneous method "algebraizes"

the differential equations and solved one set of algebraic equations. Those fundamental techniques were introduced by [61] about four decades ago and still serves as the core of dynamic simulations.

Power system engineers have been developing computer tools for power system simulation and analysis. Besides the commercial tools, the community has developed open-source packages for research and education, such as PSAT [43], MATPOWER [73], MatDyn [13], DOME [45], GridDyn [33] and ANDES [16, 15]. Most of the cited references utilize numerical methods for power system simulation based on the DAE described in (1.1). A more recent and comprehensive reference on building computer tools for power system analysis as well as the transient models for dynamic studies can be found in [44].

Improvements to the traditional numerical integration are being studied in both the formulation and the solution approach. A semi-implicit formulation of DAEs is proposed in [46] to increase the computational efficiency of the Jacobians and allow for effortless switching between algebraic and state variables. The proposed formulation uses the following form:

$$\begin{aligned} T(x,y)\dot{x} &= f(x,y,\eta,u,t) \\ R(x,y)\dot{x} &= g(x,y,\eta,u,t) \end{aligned} \tag{1.3}$$

where $T(x,y)$ and $R(x,y)$ are time-variant, neither necessarily full diagonal nor full rank matrices. Regarding solution approaches, hybrid methods are proposed in recent literature by introducing analytical preemptions into numerical integration. Hybrid methods allow for the use of comparatively larger integration time steps in numerical integration. One direction of research is to approximate the analytical solutions to the DAE problem using infinite terms of some series expansion [23].

1.4 Advances in Computer Simulation Techniques

Simulation techniques have been widely applied to scientific and engineering systems as an approach to reduce testing risks and minimize development costs. The dynamics of the power system are categorized into electromagnetic transients (EMT) and electro-mechanical transients (referred to as "transient") based on the model and time step granularity. EMT models are effective in evaluating microsecond-level transients such as over-voltages and converter dynamics, while transient models are sufficient in studying millisecond-level large-scale system stability problems. We focus on transient simulations in this context.

Power system transients are described by the physics of the essential components as well as Kirchoff's Laws. Voltage and current are the crucial variables in the dynamics. Differential equations (DE) are employed to describe the relationships of voltages, currents, and the internal states of devices. Electromagnetic transients that are fast enough are viewed as instantaneous in electro-mechanical transients. Therefore, some differential variables are converted into algebraic variables.

The power system is intrinsically a non-linear dynamic system described by a collection of DAE. Computer simulations have been the leading approach to understanding the system since the advent of digital computers. It is arguable that the general-purpose DAE solvers are not fully adaptable for power system simulations. The established computer simulation methods, however, include a "power flow" routine to find the initial states based on simplified models and a "time-domain" transient routine to solve the DAEs over time. This architecture and procedure have been widely adopted in power system simulation tools since the 1970s.

In contrast, advancements in microchips and computer processors continue to follow Moore's Law. Multi-core processors are available in most desktops and servers. The size of memory has grownto tens of gigabytes at affordable prices. On the software side, numerous high-efficiency and open-source DAE solvers as well as the underlying sparse linear solvers, such as SUNDIALs [31] and SuiteSparse [21], have been released

by researchers. Those solvers are seen in some of the commercial simulators, such as DSATools TSAT, and in some open-source projects such as LLNL GridDyn [33]. Related open-source software for distribution system simulation includes OpenDSS [24] and GridLab-D [11].

Commercial software-based simulators for wide-area stability analysis started in the early 1970s. Even today, some simulators still use legacy FORTRAN code for models and numerical computations. Commercial simulators can handle systems up to tens of thousands of buses, and the theoretical limits set by computing resources are well above any practical size. The most prominent change to commercial software is the proper utilization of multi-core processors. Some are also taking steps to integrate into control rooms for online applications. The drawback of commercial software is always the extendability as a block box for research-oriented models and routines.

Open-source simulators are still sparse for EMT and transient simulations. One of the main reasons is that the power system community is a small one that is unable to accumulate enough contributions towards successful projects. On the other hand, crafting a simulator requires extensive understanding of power systems, software engineering, and computer programming, which is time-consuming or even beyond the capability of researchers focusing on power systems.

Engineers have been making efforts to accelerate the numerical integration by parallelization when solving nonlinear DAEs. Modern direct sparse matrix solvers such as KLU and CXSparse utilize the lower-level parallel linear algebra libraries such as ATLAS and OpenBLAS [26]. Iterative solvers for linear equations are also efficient since they are parallelizable by nature on GPUs [39]. As of today, the headroom for efficiency improvements in sparse matrix solvers is limited as they are already very efficient. Parallel and concurrent simulations are also achievable for simulations having similar setups such as N-1 contingency analysis on multiple cores. It is especially helpful for small- and middle-sized systems that benefit little from internal parallelization. At a higher level, researchers are challenging the conventional numerical integration dominated transient simulation approach. Hybrid methods are

being investigated to introduce analytical information into the DAEs root-finding process.

Another observed trend in the computer simulation field is the increasing attention to model exchange and co-simulation. The intent of this trend is to develop reusable models in a general-purpose modeling language instead of hard-coding them. The Modelica language is one specifically designed for this purpose that is gaining popularity in power systems [65]. Implementing models in a Modelica-compatible environment such as OpenModelica or Dymola is rapid, and the compiled function mockup units (FMUs) are usable in all Modelica-compliant simulators. A challenge for the Modelica toolchain in power system simulation is the lack of a research-oriented open-source simulator. By utilizing the existing Modelica-based tools and libraries, such open-source simulator can be made lightweight.

Meanwhile, real-time, hardware-in-the-loop (HIL), and even power-hardware in-the-loop (PHIL) simulators are growing their market share due to their capabilities for running simulations at wall clock speed and using input and output signals during simulations. The real-time simulators are categorized into two main types represented by RTDS and OPAL-RT. RTDS uses dedicated RISC-based embedded hardware, specifically PowerPC processors, for power system emulations. It is designed to run electromagnetic transients for systems, whose sizes are limited by the number of racks. The disadvantages of using dedicated hardware include the lack of scalability and losing the quick and easy benefits of regular hardware upgrades.

OPAL-RT uses generic CISC-based servers running real-time Linux systems to perform simulations and rely on dedicated FPGA PCI-E cards for signal acquisition and output. This approach is mostly scalable as the simulation core is purely software based. It also enjoys hardware updates when Intel rolls out a new generation of processor. The OPAL-RT approach might encounter some overruns or increased simulation time step in extreme cases. PHIL uses reconfigurable devices in a closed-loop simulation, where the sensed power data are eventually converted into low voltage

signals. The power device behavior is captured in this case compared to purely software model-based simulations.

1.5 Cyber-Physical Power System Simulations

The interest in developing a cyber-physical simulation platform/testbed has been growing since the rapid development of the smart grid. Simulation has been a powerful method to study large engineered systems where it is difficult to perform actual tests; however, the traditional simulation method of the electric power system using standalone DAEs is not sufficient for communication scenarios and cybersecurity assessments. The concept of designing the next-generation real-time control, communication, and computation for large power systems was proposed a decade ago [64] [32]. Related works are categorized into the development of co-simulation platforms for power systems with communication, PMU-related cybersecurity assessments, and wide-area measurement-based control applications.

Preliminary cyber-physical test platforms have been developed for smart buildings and smart grids for cyber security related studies, such as intrusion detection, and network resilience [29, 5]. A toolkit for security research on CPS networks is proposed in [3] to connect CPS software and hardware, simulation scripts for components and physical-layer simulation engines based on network emulation, where case studies on cyberattacks and defenses are performed. A hybrid platform combining a distribution power system simulator and a software network emulator is proposed in [30] for testing impacts of communication network applications on power systems. A cyber-physical power system testbed is proposed in [2] for intrusion detection systems based on the real-time digital simulator (RTDS) platform and MATLAB. Architecture and studies of a cyber-physical security testbed known as PowerCyber are described in [4]. A global event-driven co-simulation framework is described in [40] for wide-area measurement and control schemes by showing a case study on a communication-based backup distance relay protection scheme.

To represent the communication network using computer software, some works mentioned above utilize a software-defined network (SDN) to set up and emulate reconfigurable communication infrastructures. The opportunities and challenges are assessed in [22], which discusses the benefits and risks SDNs may bring to the resilience of smart grids against accidental failures and malicious attacks. SDN controller failures are studied in [27] to assess their impacts on the physical system by presenting an example of automatic gain control (AGC). In [41], a self-healing PMU network that exploits the reconfigurable feature of SDN is proposed to achieve resiliency against cyberattacks, which is formulated into an integer linear programming model to minimize the overhead of the self-healing process. Cyberattacks on energy-related CPS have also been studied in [35] for smart buildings, and in [59] [8] [36] [55] [48] [52] for grid monitoring, protection, and control. Experience shows that open-source software-based network emulators are quick to set up and suitable for CPS testbeds aiming at fast prototyping and verifying power system research.

The above testbed designs can be taken advantage of for wide-area measurement-based control verification if the following challenges are addressed. First, telemetry and measurement devices, which describe the real-world counterparts need to be modeled. Second, the telemetry and measurement data should be streamed over industry-standard protocols, such as Distributed Network Protocol — 3 (DNP3) and IEEE C37.118, to mimic communication scenarios accurately. Finally, the measurement data may need to go through high-speed state estimation, which resides in the EMS system, for measurement-based control to reduce the impacts of measurement noise and errors.

Efforts on co-simulation with the communication network started more than a decade ago but are not yet standardized despite successful and ongoing projects [10] [62]. Primary reasons include a) there is no agreement on how the communication network should be modeled; b) there is also no well-established tool to perform the co-simulation. Customized open-source tools are mostly used in co-simulation, but they are difficult to use, and there is no industry standard, and c) as a result, the

set up of a co-simulation environment is non-standard. It is difficult for researchers to replicate existing results. The same phenomenon is observed for transmission-distribution system co-simulation. In fact, the term "co-simulation" implies that there is no appropriate tool for those purposes, and people have to glue programs together.

1.6 Challenges of Modeling and Simulation of Large-Scale Power Electronics Interfaced Systems

In the past few years, various new devices, including renewable generation sources and energy storage, are being integrated into the power grid at an increasing speed in both transmission and distribution networks [17]. Power electronics (PE) devices are used as interfaces for power transfer between dc devices and AC networks, or between AC devices on different voltage levels.

PE converters have been widely used as interfaces between the renewable generations and the ac main grid, as well as between a high voltage dc (HVDC) transmission system and the ac grid. The fully controlled converter operating as a voltage source, known as the voltage source converter (VSC), has a few characteristics that make it the most promising type of device for use as an AC/DC interface. First, the recent utilization of modular multi-level converters has boosted the capacity of VSCs to the hundred-MW level. Second, VSCs allow independent control of active and reactive power on the ac side. As a voltage source, it is also straightforward to form multi-terminal connections for an HVDC system.

Due to the enormous potential that VSCs exhibit, extensive research has been carried out on the modeling and control of VSC based renewable generations, energy storage, and multi-terminal HVDC. Regarding VSC modeling for large systems in the

transient time scale ($10^{-2}|10^{1}$ s), there have not been many discrepancies on the dq-frame control framework. For large-scale simulations, some model simplifications have been proposed to improve convergence and accelerate the simulation. A generalized current-source controlled VSC model is proposed in [14] for stability studies using the classic dual control loop formulation. A simple and computationally efficient power synchronization controlled VSC model is proposed in [53] and implemented in GE PSLF. The model is validated against PLECS EMT simulations.

The control methods of the VSC for the specific application, however, show great diversity ranging from local information based power droop control to wide-area centralized controls. For VSCs connected to a dc network, voltage droop control has been widely adopted to maintain voltage level. The basic idea is, for each converter, to adjust the dc voltage proportional to the deviation of dc power or dc current to achieve power-sharing. In [60], a variation of the P-V droop control is proposed by using a PI controller with a negative feedback gain for the power error. This variation allows for maintaining dc voltage while preserving dc power flow following an event. A detailed voltage margin control based on droop-control and voltage dead band is proposed in [38]. When the dc voltage of a non-slack converter is out of the margin, a droop will be applied, and the slack converter will be shifted into the constant power mode. Instead of using a constant droop coefficient, [12] proposes an approach to compute the droop based on the converter headroom. Recently, a consensus approach was proposed in [34] to achieve exact power-sharing using communication between neighborhoods.

Given the abundant references, challenges still exist for modeling and simulating AC/DC hybrid systems with considerable power electronics. The first problem comes with modeling the power electronic interfaces. The models need to achieve a careful balance between modeling details and computational burden. Typically, large-scale system models are used to analyze AC system stability, and therefore, the devices with PE interfaces must reflect the dynamics at the step size of milliseconds. Meanwhile,

the dc networks, described by stiff ODEs, also need to be included to examine the impacts of a dc perturbation on ac stability.

The second challenge lies in the need for simulating detailed models for protection and control purposes. For example, under fault conditions, over-current protection is needed for individual PE converters. The protective schemes need to be modeled and calibrated to avoid series/cascading converter failures. Also, to study the switching and control methods of the converters, the detailed converter model needs to be modeled in or linked to the transient simulation tool using a decoupling technique.

Further, in the software implementation, the PE interfaces for different devices need to be shared and reused to avoid code redundancy. Currently, in the widely used device models such as wind turbines and energy storage [20], the PE converter models are built-in and specific to the control algorithms. In some commercial software, the PE interfaces are hard-coded with a specified number of nodes. There is currently no open-source tool to simulate large-scale PE-interfaced systems gracefully.

Finally, local control and wide-area coordination of PE interfaces need more integrated studies. For example, the wide-area coordination of PE devices to provide inertia sharing and frequency response through closed-loop simulation of power grids, communication networks, and measurement devices is still a demanding task. The software architecture to represent multiple levels of PE controls and their coordination needs to be addressed.

1.7 Scope of this Dissertation

This dissertation focuses on large-scale simulations of modern electric power systems with an emphasis on voltage source converter based multi-terminal HVDC network modeling and control.

Chapter 1 provides a background introduction and literature review for state-of-the-art power system simulation techniques and tools. Modeling of PE interfaces and MT-HVDC systems in positive-sequence transient simulations are also reviewed.

Chapter 2 describes the implemented Large-Scale Testbed (LTB) in CURENT. LTB is a computer-based platform for verifying and demonstrating measurement-based control methods in large-scale power systems. Chapter 2 also proposes a design and implementation for the next-generation LTB as a cyber-physical system (CPS) testbed.

Chapter 3 proposes a general framework for dc network components and voltage source converters implemented in the LTB for stability studies. A general power flow model for voltage source converters is proposed, and a simultaneous solution approach using an extended formulation with the Newton method is proposed to reduce the time for Jacobian forming and factorization.

Chapter 4 describes two types of VSC models, namely, current-source controlled and voltage-source controlled VSCs, for building multi-terminal HVDC (MT-HVDC) systems. Local control loops for inertia emulation are proposed, and the control effects are compared.

Chapter 5 explores using a multi-terminal dc network for integrating offshore wind farms in a multi-area power grid. The wind generators are controlled to provide inertial response for the ac grids using local dc voltage measurement or remote ROCOF measurements. Estimations for the maximum extractable inertial power and reduced dc voltage due to inadequate inertial power supply are proposed and verified.

Chapter 2

Large-Scale Testbed Design and Implementation

2.1 Motivations and Goals

Large-scale power system simulation is crucial for operators and researchers to study the post-disturbance dynamic characteristics of a system for assessment and operation suggestions. The goal of the Large-Scale Test Bed (LTB) project is to develop a computer software-based platform for wide-area measurement-based control verifications with the structural representation of the modern electric power system. The LTB consists of a grid simulator, which continuously computes the power system states using dynamic simulation and several other relevant modules, a measurement system representing the telemetric and data acquisition devices, an energy management system (EMS), and a measurement-based control system. All these components are implemented as modules and glued together with data streaming over the communication network.

The primary challenge of the LTB is that it involves a wide range of routines such as simulation, monitoring, control, and visualization, requiring an elaborate orchestration to integrate modules seamlessly. Another challenge is to allow the

researchers to quickly spin up the platform and test their models or control methods without having to know all the details. The last major challenge is the real-time verification of control methods in the cyber-physical space, considering both the physical power system and the communication system.

The LTB is designed to run large-scale power grid models up to thousands of buses with modern power system components such as voltage source converters, multi-terminal high-voltage dc networks, and wind turbines. Interfaces to different simulation engines are available to gain capabilities including real-time simulation, high-performance computing, and fast model prototyping. Scenarios including high penetration of wind power, generation mix, and seasonal load balances are created in the North American large-scale systems. The testbed allows for flexibility as a software platform to evaluate novel power system infrastructure and validates wide-area measurement-based control methods under high penetration of renewable energy.

The LTB creates an environment that mimics the real operation of a power grid by running the nationwide or continent-wide system models on high precision simulators, providing energy management system supports, and controlling the grid based on measurements. The LTB provides a testing platform for new technologies developed by CURENT. It also serves as a driver of CURENT research since it allows fast prototyping of new models and grid infrastructures, direct access to simulation and measurement data, and instant feedback of the wide-area control signals.

2.2 Overview of the Implemented LTB Platform

The LTB is designed on a decoupled architecture based on the concept of modules. With the data interfaces properly defined, each module runs independently and communicates with others through data streaming. Modules are categorized into four types: grid simulators, measurement devices, an energy management system, and control methods. An overview of the LTB is shown in Figure 2.1.

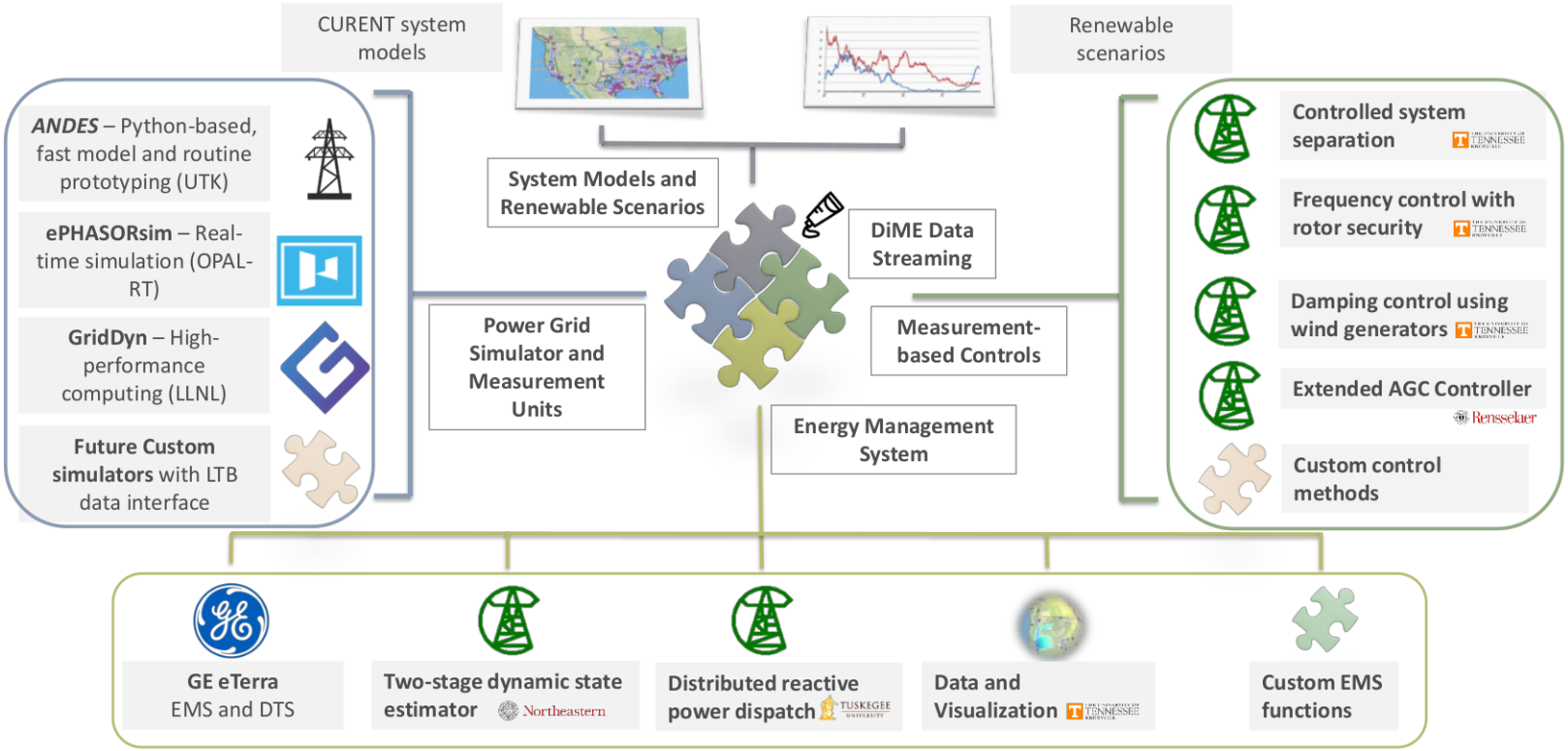


Figure 2.1: LTB architecture overview

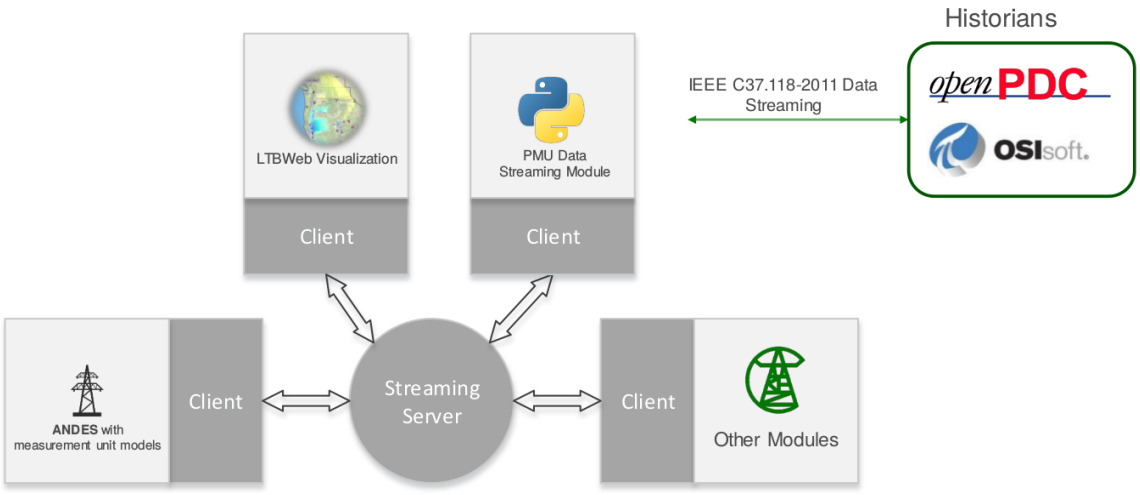


Figure 2.2: Data streaming amongst decoupled modules

These modules, the underlying communication network, and the large-scale system models make up the LTB for cyber-physical systems. The advantages of the decoupled architecture include:

1. Independence: allowing for independent module development using a common data interface; modules can run simultaneously as separate processes;

2. Interoperability: modules written in different environments, including MATLAB, Python, and C/C++, can communicate with each other;

3. Interchangeability: modules of the same function are swappable; for example, the real-time simulator can be swapped in to replace a Python-based simulator.

The core algorithms of modules are developed by the research thrusts in CURENT. A data streaming client is attached as a bridge between the core algorithm and the external modules. By connecting the streaming clients to the data server, the modules can send data to the destination modules, or receive data from others. Data packets go through the underlying communication network, which can be further studied with a communication network emulator. The decoupled architecture of the LTB is illustrated in Figure 2.2.

The LTB strives to mimic the structure and operation of a real power system. There are four categories of modules, namely, an extended-term dynamic simulator, a measurement system, energy management modules, and measurement-based control modules. Figure 2.2 shows the structural organization and data flow between the categories. The closed-loop data flow is described as follows:

1. The grid simulator produces algebraic and state variable data from time-domain integration on a large-scale grid model;
2. The measurement system receives the raw states, on which the measurement errors and delays are imposed, and sends the measurement data to the state estimator;
3. The state estimator sends the estimated states to other modules for further processing;
4. Control signals are sent back to the grid simulator for actuation.

The extended-term dynamic power grid simulator is a differential algebraic equation (DAE) solver plus the component models defining those equations. The LTB has interfaced three dynamic simulators for different purposes:

1. Andes, a Python-based simulator developed by the author for fast model prototyping and research concept verification;
2. The commercial OPAL-RT ePHASORsim for real-time simulation capability;
3. GridDyn, a high-performance grid simulator developed in Lawrence Livermore National Laboratory.

Using these simulators, the LTB maintains flexibility in research modeling and large-scale real-time applications.

The measurement system in the LTB platform is modeled as a component linked to the simulator, taking accurate values and adding errors and delays. Probabilistic

models are used to describe the measurement noises and errors where the probability distribution is fitted by the actual measurement device. Measurement data is taken at the measurement frequency, typically 30 Hz, and then timestamped before sending to the receivers such as the state estimation module.

Energy management functions in the LTB perform routines for security screenings and optimize the economic aspects of system operations. For example, the game theory based reactive power control program calculates the optimal voltage set point to maximize the system robustness. Another example is the N-1 contingency screening that performs mass parallel power flow analysis for N-1 contingencies. All the states and calculated data are sent to the EMS visualization module, which is the user interface for researchers.

2.3 Design of Cyber-Physical Testbed for Power System Wide-Area Measurement-Based Control Using Open-Source Software

The LTB is designed to mimic an electric power system with communication and control functions. The requirements for the design architecture are interchangeability and flexibility. Interchangeability means that the routines and functions are interchangeable with other methods and functions that have the same functionality. Flexibility ensures that the testbed is not limited to specific software packages initially supported but also connectible to other software platforms. The design philosophy is to build a decoupled testbed and 'glue' modules together through data streaming. Each function or routine can be encapsulated as a module and exchange data, but also remain ignorant of other module structures. Interchangeability is realized when a module, for example, a power grid simulator, is replaced with another simulator producing the same type of output. Flexibility is also realized when the testbed

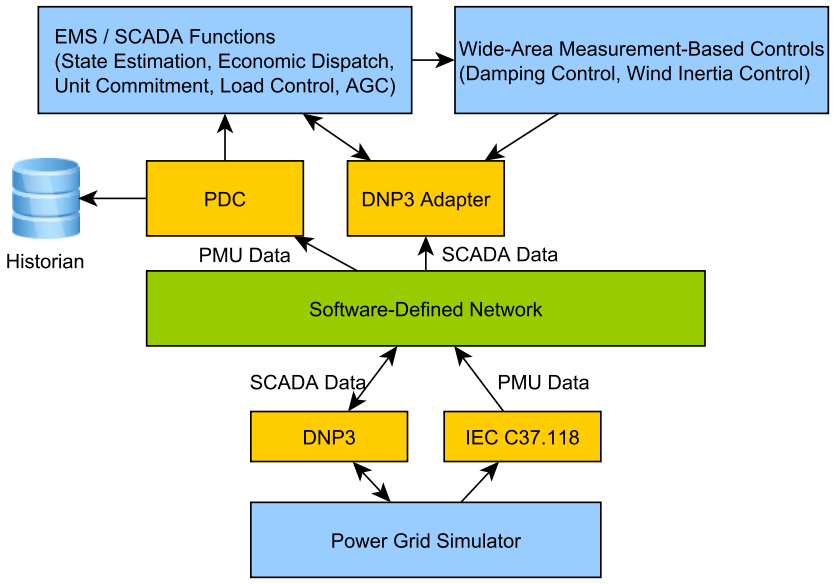


Figure 2.3: Architecture design of the LTB incorporating power network, communication network, EMS, and control

supports standard data streaming protocols, which most software platforms can easily support.

The architecture of the LTB as a cyber-physical testbed is depicted in Figure 2.3. The LTB is composed of four types of components: a power grid simulator to calculate the physical power network, an SDN to emulate the communication network, conventional EMS/SCADA with functions to control generation and load and an operator interface, and wide-area measurement-based controls to perform fast automatic controls

2.3.1 Decoupled Framework

The decoupled architecture is a framework that integrates the cyber and physical components into one testbed while allowing independent development of components. In the LTB, each element is a software module that performs a specified task given the defined input and output, such as running a power grid simulation, handling network connection and data transfer, or running wide-area measurement-based control. One

module does not need to know the details of other modules if their communication interfaces are unified, for example, using the same communication protocol.

The decoupled modules in the framework are integrated using industry-standard communication protocols over a TCP/IP network. The communication protocols from the power industry applied are DNP3 for SCADA controls and IEC C37.118 for PMU data streaming. From the power grid viewpoint, measurement data is collected from the power grid simulator for processing in the EMS and control systems. From the communication perspective, DNP3 protocol is utilized in the application layer for transferring telemetry data and sending control signals over TCP/IP in the software-defined communication network, and IEEE C37.118 protocol is used to stream PMU data from the power grid simulator to Phasor Data Concentrators (PDCs).

2.3.2 Power Grid Simulator

The power grid simulator runs computational routines to simulate the characteristics of the physical electric power grid. The main components in the physical network include generators, transformers, and transmission lines, shunt reactors and capacitors, various distribution system components, and loads, which altogether can be hundreds of different device types. The time scale of interest for dynamic power system simulations can vary from microseconds, for say lightning or switching problems, to several hours for scheduling or restoration problems.

There has always been a trade-off between modeling detail and simulation time, which arises in a transmission network simulator with potentially tens of thousands of buses. For transient stability analysis ($10^{-3} - 10^{1}$ s) of large-scale systems, positive-sequence phasor-domain models are the de facto standard in both commercial and open-source software. This assumes a balanced network, ignores transmission line transients, and considers only the positive symmetric component. This dramatically reduces the computation burden and is sufficient for electromechanical transient studies. The power grid simulator produces output at each integration step from

integrating the DAE. In a real power grid, data is acquired by telemetry and measurement devices, which only have a certain level of accuracy. To describe measurement errors and noise, a software module is added to modify the precise data from the simulation and impose errors and noise based on studies of the measurement model by [72]. Such data are then sampled for transmission using DNP3 and IEC C37.118 protocols at their specified sampling rate, respectively, before being sent over the communication network.

2.3.3 Software-Defined Network Emulator

The SDN emulates the communication network on which the data packages are transferred. The SDN is composed of physical links, switches, and routers, and is configurable in software to emulate different network scenarios. In the decoupled framework, each module with communication capability is a host on the network and has virtual ports. Each host can run processes in its namespace, and send data over the emulation network. Hosts in the SDN include the telemetry sensors, PMU, EMS and SCADA modules, and the measurement-based control modules.

The advantage of integrating an SDN into the cyber-physical testbed is simplicity. No source code modification is needed to migrate from a real network port to a virtual one. Each host can link to a real port or a virtual port simply by changing the port name and writing to sockets as usual. Network latency and package loss scenarios can also be represented by modifying the software definition of the network. Some SDNs allow binding physical ports in the virtual network so that cybersecurity scenarios can be studied. Drawbacks of using an SDN in a testbed exist and have been discussed in the literature [22]. A major concern is the performance in a massive-scale simulation such as that of continent-wide communications for a power system where thousands of virtual hosts may require a large number of computing resources. As a consequence, the data flow may suffer longer latencies in large virtual networks due to resource limitations.

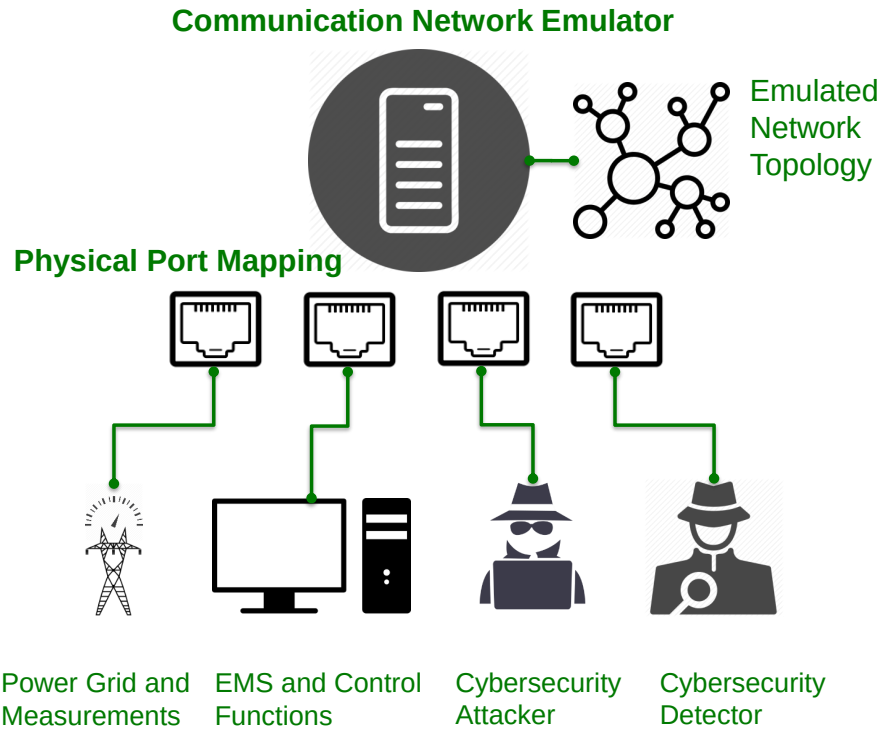


Figure 2.4: Concept of the LTB for cyber-physical testing and cybersecurity studies

The concept of using network emulators for cyber-physical power system studies is depicted in Figure 2.4. A computer equipped with a multi-port network interface card functions as a communication network emulator by establishing the SDN. Some emulated ports in the network are mapped to physical network ports so that external devices can be connected. Modules in the LTB such as measurement devices and control functions can stream data over the emulated network. Meanwhile, cybersecurity scenarios can be studied by allowing roles such as attackers and detectors in the CPS LTB.

2.3.4 EMS Functions

The EMS system plays a vital role in power system energy balance scheduling and minute-level control. An EMS system gathers telemetry data, forecasts load, runs unit

commitment and economic dispatch, screens contingencies, estimate system states, and sends automatic generation control (AGC) signals. It is the operator interface for running the power system. The timescale of scheduling and control in an EMS system varies from day-level (unit commitment) to hour-level (economic dispatch) and second-level (AGC). Most existing EMS systems communicate using the DNP3 protocol. A modification is to integrate high sampling speed PMU data so that near real-time data can be utilized for situational awareness. A high-speed state estimation module in the EMS is also needed to process PMU data, which serves as the foundation for wide-area measurement-based control functions. Other conventional controls in the EMS, such as economic dispatch and AGC, can also be updated to adopt PMU data. In the LTB, the EMS system may have multiple implementations running simultaneously in the decoupled architecture by adding a data splitter after the DNP3 converter and the PDC. This is helpful to evaluate and compare the results of different methods applied to the same system.

2.3.5 Control Functions

The control functions block is an aggregation of wide-area measurement-based control methods developed by researchers. They accept measurement data and state estimation output from the EMS system, monitor critical variables and generate control signals. Control signals are sent back to the power grid simulator using the DNP3 protocol over the communication network. These measurement-based control function can be either centralized or distributed, depending on the information they request from the EMS system [69].

The timescale of the measurement-based control functions is from sub-second to the second level as they are designed to handle faster dynamics in the system than the EMS functions. For example, power electronic devices in a FACTS device may require fast control with inter-area information, and thus, can be included in the wide-area measurement-based control block.

2.4 Open-Source Implementation of CPS LTB

The implementation of the proposed cyber-physical LTB, using open-source software is described in this section. The implementation is comprised of the power grid simulators, an SDN emulator (Mininet), telemetry and measurement units (OpenDNP3, pyPMU), EMS functions (GNU Octave), and measurement-based control functions (GNU Octave).

2.4.1 Decoupled Design

To realize the decoupled design, a dispatcher program is created for managing the module processes and handling their synchronizations. The dispatcher is written in Python as it is an extremely flexible open-source scripting language, which has gained huge popularity in recent years. Python can interface to code and programs written in other languages and provide application program interfaces (APIs) through their Python bindings. Moreover, Python has a simple and elegant syntax and a flat learning curve. Therefore, Python is ideal for a dispatcher program that handles process creations and synchronization.

The Python-based LTB dispatcher creates processes for a) each telemetry device with DNP3 client support, b) each PMU device with IEC C37.118 support, c) an EMS system with DNP3 master support, and d) a wide-area control system with ZeroMQ support. More specifically, each telemetry device loads data from the simulator, imposes measurement noise and error, and sends data to the DNP3 server, at a sampling rate of 1 frame every 2 seconds through the socket bind to a virtual port. Each PMU device loads data from the simulator imposes noises and errors, and sends data to the PDC, at a sampling rate of 30 frames per second, through the socket bind to a virtual port. The EMS process runs a DNP3 server and a PDC, maintains a list of functions that are called routinely in GNU Octave to process the incoming data. The measurement-based control process listens on a ZeroMQ socket to receive

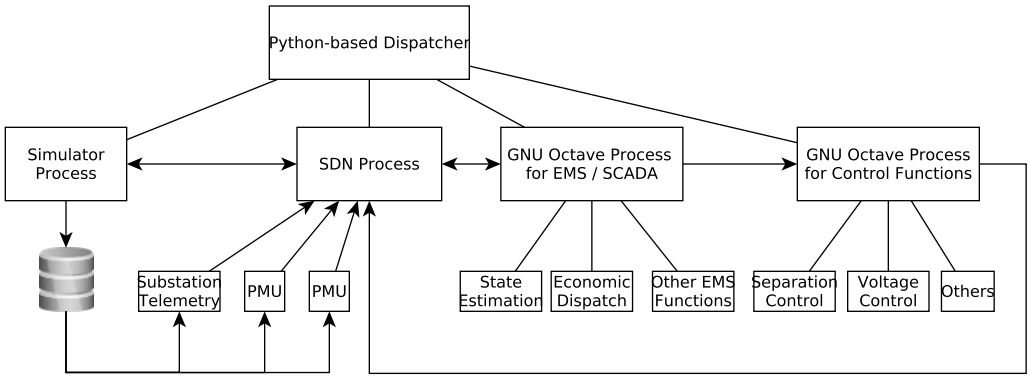


Figure 2.5: Process dispatch architecture in the proposed implementation

the measurement data and state estimation results and calls control routines in GNU Octave to generate control signals.

Software packages used in the dispatcher program include a) OpenDNP3 for telemetry devices, b) PyPMU for PMU devices and the PDC program, c) GNU Octave, which is a free and open-source MATLAB alternative for EMS and control functions, and d) ZeroMQ for data streaming between the EMS process and the control process. Figure 2.5 shows the implemented process dispatch diagram, where the arrows stand for the direction of information flow, while the solid lines without arrows represent the process hierarchy.

2.4.2 Power Grid Simulator

Although positive-sequence phasor-domain simulation for transient stability simulation in power systems has been standard for many years, the choice of an open-source power system transient simulator is relatively limited. The webpage [50] records a list of existing open-source power system simulators, of which only a few support DAE-based transient simulation. These include Power System Toolbox (PST), Power System Analysis Toolbox (PSAT), MatDyn, GridDyn, and our in-house tool, Andes.

The choice of power grid simulator depends on the model library and flexibility of the software. The model library determines the initial capability of modeling

power system devices, and flexibility determines the convenience of adding new device models. In the LTB, PSAT, GridDyn, ANDES and ePHASORsim are interfaced and made available as the simulators, all of which are open-source. Each of them has distinctive features: PSAT has native GNU Octave support, and has a considerable number of built-in models; GridDyn is written in system programming language and utilizes the *SUNDIALS* package by [31] as the underlying solver, and is thus computationally efficient. ANDES is an in-house package written in Python with an aim to provide rapid model prototyping, advanced model interfacing, and data analysis capabilities.

Owing to the decoupled design, the user can choose a power grid simulator based on their actual needs, such as model support, simulation speed, or data analytic interfaces.

2.4.3 Software-Defined Network Emulator

The SDN process in the LTB is based on Mininet [37] to create a software-based network for emulating a real communication network with switches. Mininet is installed on a Linux system, and Python APIs are used to create virtual network configurations and virtual ports/interfaces. Each interface is connected to a component, such as a PMU or an EMS system, described in Section 4.1 to mimic a real power system where the measurements and control system are distributed and connected to the network. The SDN process is responsible for creating virtual network topology scenarios, and virtual Ethernet ports in Linux, veth, which are linked to the virtual network. After initialization, the SDN emulator is ready to serve network connections and operate identically to a real network.

2.4.4 EMS Functions

The EMS process is composed of a data gateway and a set of data processing functions. The data gateway process runs a DNP3 server to gather data from

telemetry devices, and a PDC server to gather data from PMUs. The process also keeps a list of EMS functions to be called each time new data arrives or at a given time interval. To utilize the existing EMS functions written in MATLAB, the EMS process in the LTB leverages the Oct2Py package which calls GNU Octave from inside Python. Understandably, this approach could be improved by rewriting the MATLAB code in Python or using a Python port of the desired packages. For example, for optimal power flow based economic dispatch function, a Python port of MATPOWER, PyPower, is interfaced instead of calling MATPOWER in GNU Octave. The port to Python is, however, not mandatory since MATLAB functions executed in Oct2Py are fairly efficient. Implemented EMS functions to date include a) economic dispatch based on PyPower, b) unit commitment written in GNU Octave, c) contingency screening based on PyPower, and d) state estimation written in GNU Octave. In the decoupled architecture, each component function in the EMS can be replaced with another program that has the same functionality. For example, [1] replaced the traditional weighted least-square state estimator with a two-stage dynamic state estimator, which estimates not only the voltage phasors but also the relative generator rotor angles. Scheduling and control outputs are sent to the DNP3 adapter and transmitted to the power grid simulator. Meanwhile, the state estimation output and the measurement data are stored in Python objects and transmitted to the control function data gateway, using ZeroMQ through TCP/IP, as inputs to the wide-area measurement-based control modules.

2.4.5 Control Functions

Similar to the EMS process, the control process in the testbed is a collection of experimental control functions that take in wide-area measurement data and compute the control actions. Given the fact that most experimental control prototyping is done in MATLAB, the control process interfaces to GNU Octave through Oct2Py to use the research code. The control process is also composed of a ZeroMQ data gateway, which

receives measurement data and state estimation data from the EMS system, and a list of control functions to call upon data refreshment. Note that the measurement data comes in at a higher rate than the DNP3 telemetry data. Therefore, the control functions are also called more frequently, which will be more efficient if the control functions can be rewritten in Python.

Local controls and wide-area controls are implemented based on the same approach, where the only difference lies in the data visibility. In the DAE-based power grid simulator, there is no strict boundary between a utility company owned local network and an ISO-operated large power grid. Therefore, the control functions are categorized into local controls and wide-area controls depending on the input data it requests from the EMS system. This approach shows simplicity by sharing the same data channel but using different subsets to implement both local and wide-area controls and allows testing of various control system architectures.

The implemented wide-area measurement-based controls in the LTB to date include: a) under-frequency load shedding control, which monitors the system frequency and reduces load in severe low-frequency conditions, b) system separation control, which monitors severe line faults and estimated generator rotor angles and separates the system into islands as a remedial approach by [63], c) hierarchical voltage control, which controls the bus voltage from three time scales: wide-area generation dispatch, regional var regulation, and local excitation, and d) online voltage stability assessment using a tangential index from Thevenin equivalent by [67]. The control signals are sent to the power grid simulator using DNP3 protocol through the SDN.

2.5 Case Studies

The developed cyber-physical testbed is used to verify and demonstrate two wide-area measurement-based controls: system separation control for emergencies and hierarchical voltage control. Test cases are based on a reduced WECC system with wind scenarios developed in CURENT. The WECC system contains 181 buses, 313

lines (including 48 transformers), and 31 generators in a summer peak load scenario. The phasor measurement data on all the buses are aggregated into one PMU using multi-stream and sent across the emulated point-to-point network.

The results are visualized in a web-based visualization tool, which has been developed mainly for research and demonstration. The visualization tool is composed of a Python-based data ingestion module which reads data from the simulator through ZeroMQ sockets, and a database in the back-end. In the front-end, it consists of a JavaScript-based cross-platform web application using the Leaflet library and OpenStreetMap to draw buses, lines, and other physical system components, and render the contour triangulations for the selected variables.

One capability envisioned for the visualization tool is to compare cyber-physical simulation scenarios simultaneously. To enable the simultaneous comparison, the visualization tool employs HDF5-based data storage to store simulation data and a PostgreSQL-based database to store metadata. Side-by-side simultaneous comparisons of scenarios are implemented by loading the desired scenarios from disk, caching them in the memory with Memcached, and fetching them from a web socket server.

2.5.1 System Separation Control

The system separation control splits the system into multiple islands during an emergency. When multiple lines are disconnected, the connection between two or more areas of a system becomes weak. Under such conditions, angular instability issue may arise. The objective of the controlled separation scheme is to separate the system into several islands, and therefore, maintain the stability of each island. It is a wide-area, interconnection-level control method that utilizes generator rotor angles estimated from the two-stage dynamic state estimator in the EMS system.

The location of separation is based on offline studies on the test system, in our case the WECC system. Several elementary potential islands (EPI) and

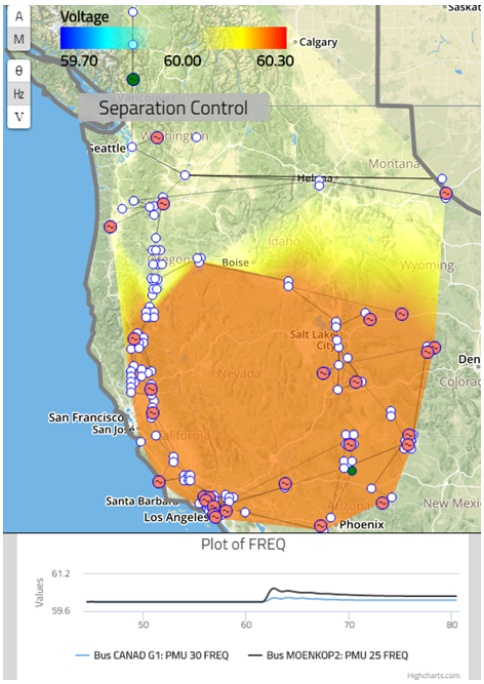


Figure 2.6: Visualization of the WECC 181-bus system frequency contour map after system separation

separation locations are studied and defined for the WECC system. The first step for implementing this control scheme is to decide the best locations to divide the system. Based on the study of WECC's elementary coherent groups, four subsystems are defined as the EPIs.

The timing of separation is also an important factor to consider. At each time step, the difference between the mean values of the largest ten rotor angles and the smallest ten rotor angles is calculated. When the absolute value of this difference reaches a certain threshold, the system will separate into islands. The control module communicates with the grid simulator through a ZeroMQ socket.

Lines 83-172 and 83-170 are disconnected at 5s and 40s, respectively, to create a weak connection between EPI 0 and EPI 1. At 61.5s, the system is separated into two subsystems by cutting the interface EPI 0 / EPI 1 and the interface EPI 0 / EPI 3. The load is reduced 10% in EPI 1 to maintain the stability of the island comprised

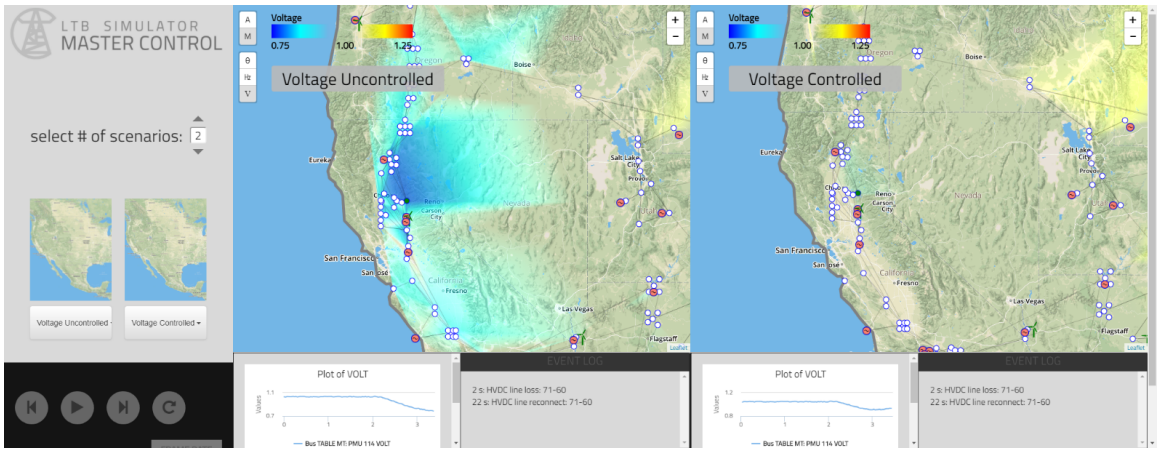


Figure 2.7: Simultaneous comparative visualization of hierarchical voltage control on the WECC 197-bus system

of EPI 1, EPI 2 and EPI 3. The frequency contour map from the simulation result is visualized in Figure 2.6, which demonstrates the successful system separation.

2.5.2 Hierarchical Voltage Control

Hierarchical voltage control allows wind farms to support interconnection-level system-wide voltage control and reactive power dispatch. The control aims at maintaining reactive power sufficiency in systems with a high level of wind power by hierarchical measures: a) re-dispatching power flow in the interconnection level, b) regulating regional wind farm reactive power, and c) tuning local excitation system parameters for generators. The interconnection-level re-dispatch is implemented as an economic dispatch routine maximizing reactive power support, while the other two controls are realized in the control system. This control combines local control and wide-area control and utilizes voltage phasor estimation from the EMS system.

The hierarchical voltage control is tested on a modified WECC 197-bus system with 22% wind penetration. The contingency to demonstrate the proposed control is a monopole dc loss, which heavily stresses the California-Oregon Intertie. NERC standard recommends that any voltage dip lower than 0.8 pu for more than 40 cycles is considered a voltage instability, which may trigger the actions of Under-Voltage Load

Shedding (UVLS). The simultaneous comparison of the controlled and uncontrolled scenarios is shown in Figure 2.7. The voltage contour map shows the low-voltage region in the system due to the HVDC line loss. The implemented voltage control method, which is based on measurement data, is effective in reducing voltage dips in the studied system.

2.6 Remarks on this Chapter

This chapter proposes a cyber-physical testbed design and implementation for wide-area measurement-based control using open-source software. A positive-sequence phasor-domain power grid simulator is adopted for the physical system, and an SDN emulator is used to establish the cyber system. A decoupled architecture is proposed by connecting telemetry and measurement devices over the communication network to an EMS system and a control system over standard data streaming protocols. Regarding implementation, the functional modules are dispatched by a Python-based program on a Linux system.

The LTB platform based on open-source tools is designed for testing wide-area measurement-based control techniques. It allows for quickly integrating modern EMS functions and measurement-based control methods in large-scale cyber-physical systems. It serves as a tool to assess the EMS and control functions from the cyber-physical perspective. Future work includes assessing the impacts of measurement errors, topology errors, and communication delays on wide-area controls. Cybersecurity is also an important application that can be evaluated with the testbed.

Chapter 3

High Voltage Direct Current Transmission Systems

3.1 DC Network Model

The "War of Currents" – in which Thomas Edison and Nikola Tesla were embroiled – between the alternating current (AC) and direct current (DC) technologies in the late 1880s was concluded by Thomas Edison being forced out of controlling General Electric and the Tesla jumping on the ac train. Since then, ac technology has dominated the electric power system for power generation, transmission, and distribution.

The main shortcoming that caused dc to lose the war was its struggle to transform voltage level as a means of reducing line losses. After more than a century, this challenge has been conquered with advancements in semiconductor-based power electronic technologies. Nowadays, high-voltage dc (HVDC) systems are more economical than traditional high-voltage ac systems when the distance goes beyond the break-even point. This is mostly due to DC's reduced number of lines (bi-polar dc versus three-phases AC) and the elimination of induced electromagnetic losses. Increasing attention has been given to utilizing HVDC systems and creating overlays

on the ac system to increase bulk power transfer capacity and enhance transmission efficiency.

A traditional HVDC model such as two-terminal dc lines in a stability analysis program does not explicitly model the dc line since it is bound to the inverter and rectifier. The recent voltage-source converter technologies allow the formation of multi-point dc network connections, thus there arises the need to model a general-purpose dc network for various devices.

3.1.1 DC Nodes

DC nodes are the points of connection for dc devices. Each dc node introduces a nodal voltage variable $v_{dc,h}$ and an equation on this node. Using the current injection model, the current balance equation for the nodes are:

$$\sum_{i \in \Omega_h} i_{dc,h,i}(\boldsymbol{x}, \hat{\boldsymbol{y}}, \boldsymbol{v}) = 0, \quad h \in \aleph \tag{3.1}$$

where $i_{dc,h,i}$ is the current injection of device i into node h, and $\aleph$ is the set of nodes in the dc system. This equation assumes current injection into the node as reference.

3.1.2 DC Device Abstraction

A commonly accepted assumption for modeling the ac network in the stability program is the implicit treatment of the ground. The advantage of this assumption is that only one voltage variable is needed for shunt-connected devices, which are the majority in the ac network. On the other hand, series-connected devices are of equal importance in the dc network. Therefore, a series device model is adopted for all the components in the dc network.

In this abstraction, each dc device has two terminals. Each terminal can be connected to a dc node, where the device can obtain the dc voltages using

$$v_{dc,i} = v_{dc,h} - v_{dc,k} \tag{3.2}$$

Therefore, two interface equations are needed to impose the power injections on the nodes. The current injection is computed by the dc device model based on its characteristics.

The series-connected model provides flexibility to connect dc devices in arbitrary ways. For instance, the bi-polar symmetric converter topology can be implemented by connecting two converters in series and the ground at the mid-point. When used as a shunt-connected device, a ground device is connected to one of the two terminals.

3.2 Generalized VSC MT-HVDC Model

3.2.1 VSC MT-HVDC Equivalent Circuit

In power flow analysis, only the steady-state equations of VSC are considered. Fig. 3.1 shows a VSC MT-HVDC equivalent circuit in shunt connection. The converters *i, j, k* are connected to an ac network bus *i, j, k* with a coupling transformer having an equivalent impedance of Zsh. They also connect to dc nodes *i, j, k* linked by dc lines.

In this scheme, the converters at Buses *i, j* are considered as primary converters which are capable of controlling the active power and reactive power flow from the ac buses independently. The converter at Bus k is a secondary converter capable of controlling the ac bus voltage V_k and the dc voltage Vdc_k. Therefore, converter k is slack to balance power exchange among the converters. This scheme can be extended to N-terminal HVDC networks where the first $N-1$ converters are primary, and the Nth converter is secondary.

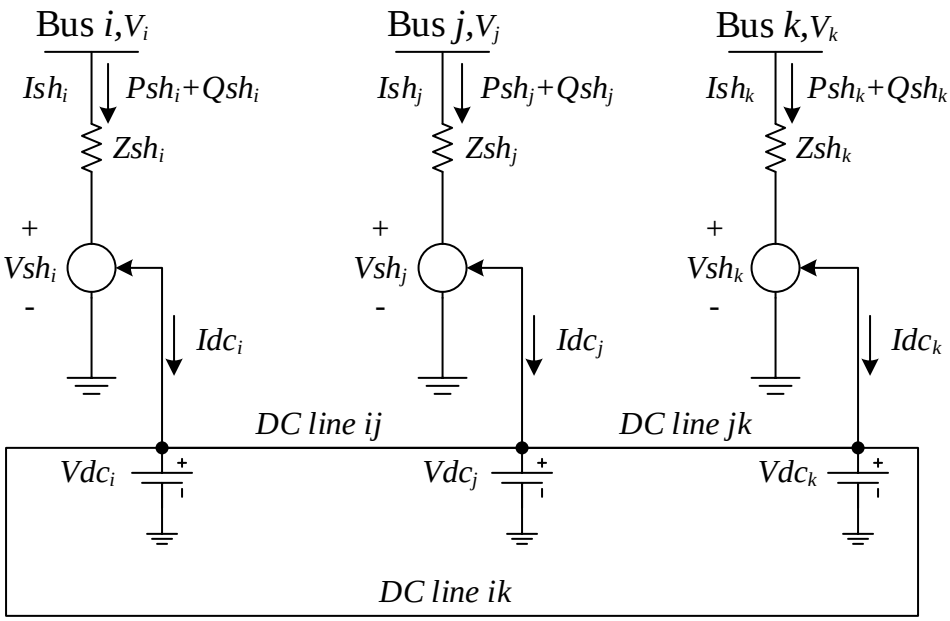


Figure 3.1: Generalized system with VSC MT-HVDC

3.2.2 VSC MT-HVDC Power Flow Equations

The VSC MT-HVDC equivalent circuit is modeled in the phasor domain, i.e., the converters are represented at the fundamental frequency by the voltage phasors $\mathbf{V}sh_m = Vsh_m \angle \theta sh_m (m = i, j, k)$. The power injection from the ac bus m to the coupling transformer is given by:

$$Ssh_m = V_m \times Ish_m^* = V_m \times \left(\frac{V_m - Vsh_m}{Zsh_m} \right)^* \tag{3.3}$$

where V_m is the voltage magnitude of bus m, Ish_m is the current in the coupling transformer, and Zsh_m is the equivalent impedance of the transformer. $Zsh_m = Rsh_m + jXsh_m$, where Rsh_m and Xsh_m are the resistance and reactance of the transformer. The real and imaginary parts of (3.3) correspond to the active and reactive power injections:

$$\begin{aligned} Psh_m =& gsh_m V_m^2 - gsh_m V_m Vsh_m \cos(\theta_m - \theta sh_m) \\ & - bsh_m V_m Vsh_m \sin(\theta_m - \theta sh_m) \end{aligned} \tag{3.4}$$

$$\begin{aligned} Qsh_m = &- bsh_m V_m^2 - gsh_m V_m Vsh_m \sin(\theta_m - \theta sh_m) \\ &+ bsh_m V_m Vsh_m \cos(\theta_m - \theta sh_m) \end{aligned} \tag{3.5}$$

where $Zsh_m = 1/(gsh_m + jbsh_m)$, $m = i, j, k$.

The power balancing equation of each converter involves the throughput power, converter losses, and the actual output. The active power through the converter, Pdc'_m, is given by:

$$\begin{aligned} Pdc'_m =& Re(-\mathbf{V}sh_m \mathbf{I}sh^*_m) \\ =& gsh_m Vsh^2_m - gsh_m V_m Vsh_m cos(\theta_m - \theta sh_m) \\ &+ bsh_m V_m Vsh_m sin(\theta_m - \theta sh_m) \end{aligned} \tag{3.6}$$

which consists of two parts: the neat power injection to the dc network Pdc_m and converter losses Pl_m. The converter loss term can be further split into three components: a constant power term, a constant voltage term, and a constant impedance term. In other words, the loss terms are independent, linearly and quadratically dependent on the converter current:

$$\begin{aligned} Pl_m &= Pdc'_m - Pdc_m \\ &= a + b \cdot Ish_m + c \cdot Ish^2_m \end{aligned} \tag{3.7}$$

The next set of equations is the dc network equations. The dc network model is composed of dc nodes and dc lines. The dc power flow pattern is dictated by the network line resistances and the dc node voltages following Kirchoff's laws. Therefore, a voltage variable and a current injection equation are added for each node.

The current injection from the dc network to the nodes is given in the following matrix form:

$$\mathbf{I} = -\mathbf{Y}\mathbf{V}dc \tag{3.8}$$

where $\mathbf{I} = [I_i, I_j, I_k]^T$ is the dc nodal current injections from lines, $\mathbf{V}dc = [Vdc_i, Vdc_j, Vdc_k]^T$ is the dc node voltage magnitudes, and $\mathbf{Y}$ is the dc conductance

matrix following the ac admittance matrix definition. Equation (3.8) can be written in tensorial form as:

$$Idc_m = -\sum_n Y_{mn} \cdot V_n \tag{3.9}$$

where $\forall m = i, j, k$, $n = \{i, j, k\}$, and Y_{mn} is the element at (m, n) in the conductance matrix $\mathbf{Y}$.

The current injection from the converter into node m is given as:

$$\mathbf{I}dc_m = Pdc_m / V_m \tag{3.10}$$

where Pdc_m is the power injection from VSC into the dc network given by (3.7). The current injections from all devices into node m follow Kirchoff's law and sum up to zero.

Finally, all converters are subject to physical voltage and current limits. The limits are rated values of the converters which need to be handled carefully in the power flow formulation. Voltage limits are given by:

$$Vsh_m^{min} \leq Vsh_m \leq Vsh_m^{max} \tag{3.11}$$

The current flow through the VSC equals the current through the coupling transformer, given by:

$$Ish_m = \frac{\sqrt{V_m^2 + Vsh_m^2 - 2V_m Vsh_m \cos(\theta_m - \theta sh_m)}}{|Zsh_m|} \tag{3.12}$$

Note the throughput current is not an independent variable in the equations but a function of several variables. In the final solution, it is limited within the rating:

$$Ish_m \leq Ish_m^{max}, m = i, j, k \tag{3.13}$$

3.2.3 Voltage and Power Flow Control of Converters

In an N-terminal VSC HVDC network, the $N-1$ primary converters are capable of controlling either PQ or PV independently, while the Nth secondary converter can control the voltage magnitude on the ac bus and dc node. Power or voltage control of the VSC in power flow analysis forces the controlled variable at the desired value. These controls are valid if neither voltage nor current constraint is binding. That is, the controlled variables equal the desired values, depending on the control mode.

Primary VSC - PQ Control

The primary converter controls the active and reactive power injections at the connected ac bus independently. This is given by:

$$0 = Psh_m - Psh_m^c \tag{3.14}$$

$$0 = Qsh_m - Qsh_m^c \tag{3.15}$$

where Psh_m^c and Qsh_m^c are the desired active power and reactive power on bus m, $m = i, j$.

If either voltage or current limit of a PQ-controlled primary converter is reached, the voltage will be set to the limit to release the reactive power control. If the other limit is also reached, the active power control will be released.

Primary VSC - PV Control

The converter controls the active power injection and bus voltage magnitude on the ac bus. The control is given by (3.14) and (3.16):

$$0 = V_m - V_m^c \tag{3.16}$$

where V_m^c is the desired voltage magnitude of bus m, $m = i, j$.

If voltage or current limit is reached, the converter voltage will be set at the limit, and the ac voltage control will be dropped first, and then the active power control.

Secondary VSC - Voltage Control

The secondary VSC acts as a reference/slack bus for active power balancing in the dc network. dc nodal voltage on the dc slack node is controlled to the reference value given by:

$$0 = Vdc_k - Vdc_k^c \tag{3.17}$$

Power injections on the connected ac bus are hence slack and uncontrollable. The voltage magnitude on the connected ac bus is controlled, given by:

$$0 = V_k - V_k^c \tag{3.18}$$

where V_k^c is the desired voltage magnitude on the secondary VSC connected bus k. ac network voltage control will be released if either voltage limit or current limit is reached.

3.2.4 Summary of VSC Power Flow Model

The generalized VSC MT-HVDC model with controls and limits contains the following equations:

AC Bus Power Outputs

(3.4) and (3.5)

VSC Power Injections and Losses

(3.6) and (3.7)

VSC Limits

(3.11) and (3.13),

Primary Converter Controls

(3.14), (3.15) or (3.14), (3.16)

Secondary Converter Controls

(3.17), (3.18)

DC Network Current Injections

(3.10)

3.3 Formulating into Newton Power Flow

The power flow problem is to find the zero of a set of non-linear equations starting from an adequate initial guess. The general form of the power flow equation is given as follows:

$$\mathbf{g}(\mathbf{y}) = 0 \tag{3.19}$$

where $\mathbf{y}$ represents the steady-state algebraic variables. The state variables of the differential equations will be initialized afterwards.

3.3.1 Newton Method with Automatic Reactive Power Limit

Before considering VSC MT-HVDC, the power flow equations are revisited. The commonly adopted equations are nodal power mismatches which include the active power mismatch for PQ- and PV-connected buses, and reactive power mismatch for PQ-connected buses. Reactive power limits of PV generators are checked after each iteration. If a limit is reached, the PV generator will be converted to a PQ load to

fix the reactive power output at the limit, and a reactive mismatch equation has to be added. Checking the reactive power limit can be easily done by an if-then logic. The addition of equations, however, will change the size of matrices and requires re-factorization of the Jacobian, which is time-consuming. [19]

The inclusion of PV reactive power output in the power flow equation set is proposed in [44], which retains the size of the Jacobian matrix. For each PV-connected bus, a variable Q for the reactive power output is added, as is an equation for the reactive power mismatch on that bus. Also added is a variable V for the voltage magnitude and an equation for the voltage mismatch given by (3.20), where V_0 is the desired value.

$$0 = V - V_0 \tag{3.20}$$

Organizing the equations by grouping together active power mismatches, reactive power mismatches, voltage deviation (for the PV and slack buses), and angle deviation (for the slack bus only), the equations can be written in the following form:

$$\mathbf{g} = [g_p^T, g_q^T, g_v^T, g_\theta^T]^T = 0 \tag{3.21}$$

The linearized equation for each Newton iteration can be written as:

$$\begin{bmatrix} \Delta P \\ \Delta Q \\ \Delta V_e \\ \Delta \theta_e \end{bmatrix} = - \left[\begin{array}{cc|cc} g_{p,\theta} & g_{p,v} & 0 & g_{p,pg} \\ g_{q,\theta} & g_{q,v} & g_{q,qg} & 0 \\ \hline 0 & g_{v,v} & \varepsilon & 0 \\ g_{\theta,\theta} & 0 & 0 & \varepsilon \end{array}\right] \begin{bmatrix} \Delta\theta \\ \Delta V \\ Q_g \\ P_g \end{bmatrix} \tag{3.22}$$

where $g_{p,\theta} = \nabla_\theta^T g_p$, $g_{p,v} = \nabla_v^T g_p$, $g_{q,\theta} = \nabla_\theta^T g_q$, $g_{q,v} = \nabla_v^T g_q$, $g_{v,v} = \nabla_v^T g_v$, $g_{\theta,\theta} = \nabla_\theta^T g_\theta$. Note that $g_{p,pg} = \nabla_{pg}^T g_p$ and $g_{q,qg} = \nabla_{qg}^T g_q$ are the derivatives of g_p and g_q with respect to the specific generator output, and ϵ is a diagonal matrix of small values (10^{-6}) to avoid singularity in matrix factorization.

Each time before evaluating all the equations, the reactive power limits are checked for violations. If a violation happens, the corresponding reactive power output will be set to the limit, and, more importantly, the voltage mismatch equations will be forced at 0, which invalidate the voltage control on PV buses. This process does not affect the size or shape of the Jacobian matrix. Hence the symbolic factorization can be re-used.

One observation from the Jacobian matrix (3.22) is that, except for the upper-left block corresponding to the bus power injection mismatch equations, the values in the matrix are constant. In other words, only the upper-left block needs to be updated at every iteration using the Newton method. Since the matrix size does not change, variations of the Newton method which do not update the Jacobian at every step, e.g. the Dishonest Newton method, can be applied.

3.3.2 Incorporation of VSC MT-HVDC Model

The equations and the Jacobian matrix need to be extended to incorporate the VSC MT-HVDC model described in Section 3.2.4. The introduced variable set of the VSC is given by (3.23), whose increments are appended to the right-hand side of (3.22).

$$\mathbf{X_2} = [\theta sh, Vsh, Psh, Qsh, Pdc', Pdc, Vdc, Ish] \tag{3.23}$$

The introduced equation set of VSC is given by (3.24), which are appended to the left-hand side of (3.22). The components in (3.24) correspond to equations (3.4), (3.5), (3.14), (3.15), (3.6), (3.7), (3.10), (3.12), respectively. All terms in each equation are moved to one side to evaluate the mismatch for each iteration.

$$\mathbf{g_2} = [g_{Psh}^T, g_{Qsh}^T, g_{Psh^c}^T, g_{Qsh^c}^T, g_{Pdc'}^T, g_{Pl}^T, g_{Pdc}^T, g_{Ish}^T]^T \tag{3.24}$$

In addition to (3.23) and (3.24), for each VSC in voltage control mode, (3.16) or (3.18) is not explicitly used. Rather, the connected ac bus is converted to a PV-type

bus, where a voltage variable and voltage mismatch equation g_{V^c} is added, such as in (3.20).

The corresponding Jacobian matrix is obtained by taking the derivative of each equation for each variable. Note that if the power outflows from the VSC connected ac buses are added to the ac network equations, namely ΔP and ΔQ, then the derivatives of ΔP and ΔQ for Psh and Qsh need to be evaluated. Similarly, the derivatives of (3.24) for ac voltage magnitude and angle need to be included.

3.3.3 Automatic VSC Control and Limit Enforcing

In the framework of the Newton method with an automatic reactive power limit described in Section 3.3.1, the voltage and current limits of the VSC MT-HVDC model can be automatically handled without changing the size of the Jacobian matrix. The approach is described as follows:

No Limit Violation

If there is no limit violation at this iteration, all controls are maintained, which means enforcing the corresponding control equation. For example, if the PQ control of a primary converter is effective, g_{Psh^c} and g_{Qsh^c} need to be evaluated for mismatches.

Limit Violations

If either voltage or current limit is reached, the reactive power control or voltage control is first released. The violated term is set to the limit value, and the corresponding equation g_{Qsh^c} or g_{V^c} is set to 0 using (3.25). If the other limit is reached after releasing the first controlled variable, the active power control will be released. For the secondary converter, ac voltage control is released first, and then the dc node voltage control.

$$g_{Qsh^c} \triangleq 0 \; or \; g_{V^c} \triangleq 0 \tag{3.25}$$

The voltage and current limits of the VSC can be checked at every iteration, but it is more effective to start enforcing the limits when the mismatch is relatively small.

3.4 Case Studies and Results

3.4.1 IEEE 14-Bus System

The proposed method for VSC MT-HVDC control and limit enforcement is simulated on the IEEE 14-bus and the Polish 9241-bus systems. Simulations are performed on a Python-based software package, *ANDES* [18], using CVXOPT 1.1.8 for sparse matrix operations and KLU for fast sparse matrix factorizations. A standard Newton-Raphson method with a convergence tolerance of 10^{-8} is implemented. Limit enforcement is turned on starting at the fourth iteration, and a maximum of one PV can be converted in each iteration. All the case studies are carried out on a PC with an i7-6700 processor and 16GB of RAM.

On the IEEE 14-bus system, we consider the following four scenarios:

1. Base case with $qG_2 \leq 0.4$.
2. Base case with $qG_2 \leq 0.4$, dc networks and VSC
3. Base case with $qG_2 \leq 0.4$, dc networks and VSC with V_{shmin} limit on VSC 4.
4. Base case with $qG_2 \leq 0.4$, dc networks, VSC with V_{shmin} limit on VSC 4 and reduced I_{sh} limit on VSC 3.

In the modified test cases, generator reactive power is limited to 0.4 pu, 0.4 pu, 0.24 pu and 0.24 pu, respectively. The four VSCs are connected to the 14-bus system on Buses 1, 2, 13, and 14, and their dc output is connected to a circular dc network where each dc line has a resistance of 1 pu. The control methods and the parameters are listed in Table 3.1. All the loss coefficients are neglected.

Table 3.1: MT-HVDC VSC Set Points

VSC Number	Bus Number	First Control Variable	Second Control Variable	V_{shmax}	V_{shmin}	I_{shmax}
1	1	$v_{dc} = 1$	$V = 1.06$	1.1	0.95	0.5
2	2	$P = -0.08$	$Q = 0.01$	1.1	0.95	0.5
3	13	$P = 0.12$	$Q = 0.01$	1.1	0.95	0.5
4	14	$P = 0.12$	$V = 1.02$	1.1	0.95	0.5

Table 3.2: Scenario 1: Base Case with $qG_2 \leq 0.4$

Bus m	v [pu]	θ [rad]	p_G [pu]	q_G [pu]	p_L [pu]	q_L [pu]
1	1.06	0	2.3239	-0.1535	0	0
2	1.0442	-0.0015	0.4	0.4	0.217	0.127
3	1.01	-0.0039	0	0.2400	0.942	0.19
4	1.0183	-0.0032	0	0	0.478	-0.039
5	1.0199	-0.0027	0	0	0.076	0.016
6	1.07	-0.0043	0	0.1243	0.112	0.075
7	1.0618	-0.0041	0	0	0	0
8	1.09	-0.0041	0	0.1744	0	0
9	1.0562	-0.0046	0	0	0.295	-0.046
10	1.0512	-0.0046	0	0	0.09	0.058
11	1.057	-0.0045	0	0	0.035	0.018
12	1.0552	-0.0046	0	0	0.061	0.016
13	1.0504	-0.0046	0	0	0.135	0.058
14	1.0357	-0.0049	0	0	0.149	0.05

The base case solution to the original 14-bus system can be found in [44]. The solution to the first scenario is listed in Table 3.2, where reactive violation on Bus 2 is enforced at the fourth iteration to fix the reactive power generation at its maximum. It takes eight iterations in 0.0071 seconds to reach the tolerance.

Scenario 2 considers the four VSCs and a dc network. The bus-wise solution to this scenario is listed in Table 3.3, while the results of the VSC converters are given in Table 3.4, where the grey cells are the effective limits. Note that the power flow into the VSCs, namely P_{sh} and Q_{sh}, are counted as a load on the connected buses. This scenario is solved in five iterations in 0.0006 seconds with no limit violations.

Table 3.3: Scenario 2: Base Case with $q_{G2} \leq 0.4$, VSC MT-HVDC Network

Bus m	v [pu]	θ [rad]	pG [pu]	qG [pu]	pL [pu]	qL [pu]
1	1.06	0	2.308	-0.0758	0.1633	0.0758
2	1.045	-0.08124	0.4	0.3824	0.297	0.117
3	1.01	-0.2095	0	0.2227	0.942	0.19
4	1.021	-0.1623	0	0	0.478	-0.039
5	1.023	-0.1364	0	0	0.076	0.016
6	1.07	-0.2047	0	0.1603	0.112	0.075
7	1.059	-0.2013	0	0	0	0
8	1.09	-0.2013	0	0.1911	0	0
9	1.049	-0.2218	0	0	0.295	-0.04289
10	1.045	-0.2237	0	0	0.09	0.058
11	1.054	-0.2165	0	0	0.035	0.018
12	1.055	-0.2121	0	0	0.061	0.016
13	1.053	-0.206	0	0	0.015	0.048
14	1.02	-0.2061	0	0	0.029	0.1889

Table 3.4: Scenario 2: VSC MT-HVDC Solutions

Bus m	Node n	Psh [pu]	Qsh [pu]	Pdc [pu]	Vm [pu]	Vsh [pu]	Ish [pu]
1	1	-0.163	-0.076	-0.163	1.06	1.055	0.170
2	2	-0.080	0.010	-0.080	1.045	1.045	0.077
13	3	0.120	0.010	0.120	1.054	1.055	0.114
14	4	0.120	-0.139	0.120	1.020	1.012	0.180

Table 3.5: Scenario 3: VSC MT-HVDC Solutions ($V_{sh3} \leq 1.05$)

Bus m	Node n	Psh [pu]	Qsh [pu]	Pdc [pu]	Vm [pu]	Vsh [pu]	Ish [pu]
1	1	-0.163	-0.076	-0.163	1.06	1.055	0.170
2	2	-0.080	0.010	-0.080	1.045	1.045	0.077
13	3	0.120	-0.018	0.120	1.051	1.050	0.116
14	4	0.120	-0.133	0.120	1.020	1.013	0.176

Table 3.6: Scenario 4: VSC MT-HVDC Solutions ($V_{sh3} \leq 1.05$ and $I_{sh4} \leq 0.15$)

Bus m	Node n	Psh [pu]	Qsh [pu]	Pdc [pu]	Vm [pu]	Vsh [pu]	Ish [pu]
1	1	-0.163	-0.076	-0.163	1.06	1.055	0.170
2	2	-0.080	0.010	-0.080	1.045	1.045	0.077
13	3	0.120	-0.030	0.120	1.051	1.050	0.118
14	4	0.120	-0.097	0.120	1.027	1.022	0.150

Scenario 3 reduces the range of the converter ac terminal voltage V_{shmax} from $[0.95, 1.1]$ to $[0.95, 1.05]$. Results from Scenario 2 violate the limit, and the iteration process must enforce the voltage limit by relaxing the reactive power set point. At iteration 4, V_{shmax} is reached on VSC 4 and is capped at 1.05 pu. The problem is solved in eight iterations in 0.0134 seconds, and no further violations are observed. The solution to the VSC variables is listed in Table 3.5.

Scenario 4 imposes a converter current limit, which is common for power electronic interfaces. The current limit on VSC 4 is reduced to 0.15 pu. The solutions in Scenarios 2 and 3 violate the limits, which have to be enforced during the iterations. The solution process took 39 iterations in 0.0436 seconds. The V_{shmax} limit for VSC 3 and I_{shmax} limit for VSC 4 are hit and capped at the maximum at iteration 4. Solutions of the VSC variables are given in Table 3.6.

3.4.2 Large Test Systems

The proposed method is also applied to solve the CURENT North American test system. The test system is composed of three interconnections: Western Electricity Coordinating Council (WECC), Eastern Interconnection (EI), and Electricity Reliability Council of Texas (ERCOT). The base power flow data has been published to the BetterGrids repository, available at [9] in PSS/E format.

In our study, a bipolar, nine-terminal, 10-link MT-HVDC overlay is added to the test system to replace the existing back-to-back line-commutated converter (LCC) HVDC stations. The MT-HVDC network is built to link the remote buses with high generation capacity and the load center buses. The power flow of the test system is solved in 0.133 seconds with ANDES 0.6.0 in eight iterations.

Given the page limits, instead of listing numerical values, this section shows some visualizations of power flow results. First, the ac bus voltages are shown in Figure 3.2. The voltage level is illustrated by the color and the radius of the circle. Note that although the EI and ERCOT system models are built from model reductions based on their full models, the ac transmission network lines are in a star topology that is unrealistic. It is observable that the WECC interconnection has a generally higher voltage level.

The visualization in Figure 3.3 shows the generation bus active power injections and the VSC station power injections. The left- and right-hand sides of the color bar correspond to the bus injections and the converter injections, respectively. It can be observed that the VSC converters absorb power from the midwest and north-Texas, where renewable power generation is abundant for load centers in populated cities.

Finally, the Polish 9248-bus test system from MATPOWER 5.1 is also studied. PV reactive power checking for the system is turned off, while the limit enforcement of the VSC remains on. The base 9248-bus system is first solved using ANDES in seven iterations in 0.4461 seconds, which is faster than MATPOWER which takes 0.5996 seconds yielding the same results. A modified system with a 10-terminal VSC

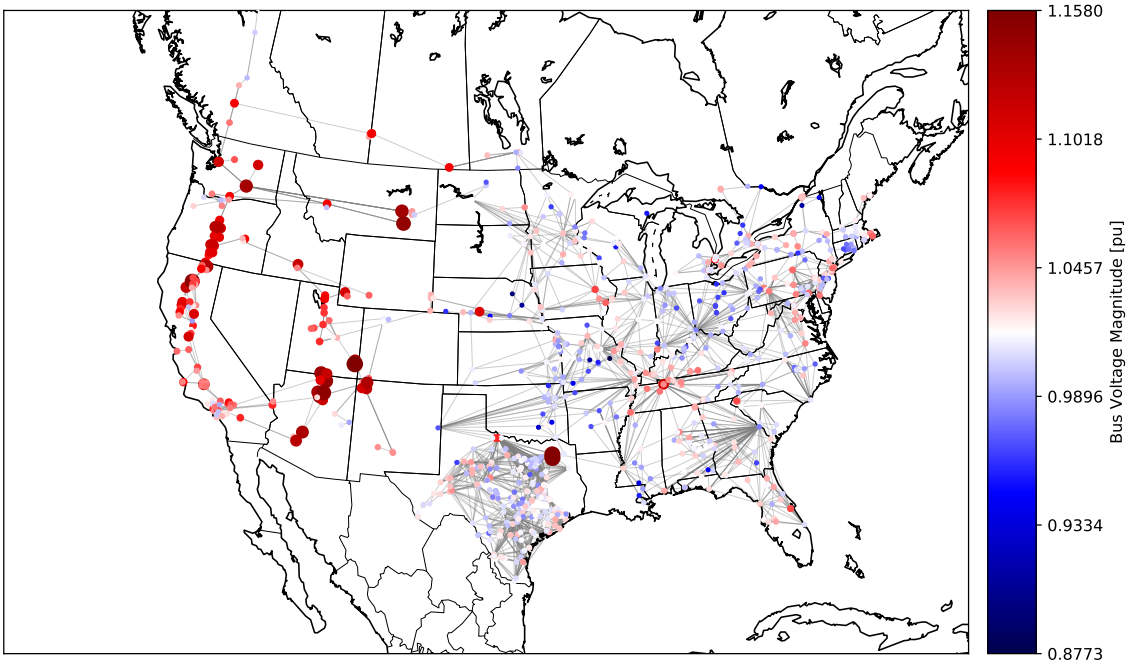


Figure 3.2: AC voltage magnitude visualization for the CURENT North American System

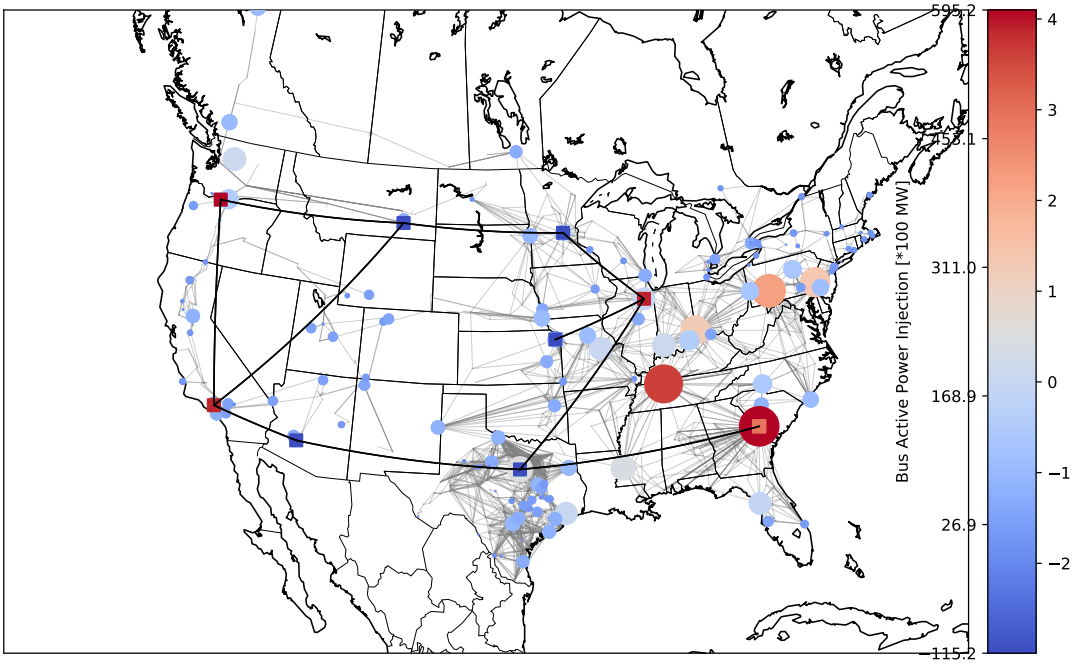


Figure 3.3: Power injections on buses and VSC converter stations

HVDC network is solved. With VSC MT-HVDC added, the test system takes eight iterations in 0.6211 seconds.

3.4.3 Conclusion

In this chapter, an automatic control and limit enforcement method for VSC MT-HVDC is elaborated. By using additional equations in the Newton power flow routine, voltage and current limits can be enforced during the iterations by switching out the control equations and substituting in the limits. Case studies verify the proposed method for handling multiple violations during iterations.

Chapter 4

Transient Models for VSC and MT-HVDC Networks

4.1 Classification of VSC-Based Interface

The roles of VSC-based interfaces connected to an ac grid are mixed. They are neither solely grid-forming converters which form the ac voltage nor a grid feeder which purely injects power. The mixed role is termed as grid-supporting converters which transfer designated power while simultaneously contribute to the frequency and voltage regulations [54]. Distinguished by the synchronization method, VSC interfaces can be controlled as a current source with a shunt impedance in parallel, or as a voltage source with a series impedance. Their output current and voltage, respectively, are controllable to maintain the output power, bus voltage and measured frequency around the reference values.

The current-source controlled VSC is the more commonly studied between the two types. This type of VSC adjusts its output current based on the bus voltage to deliver power at the reference values, which may be adjusted by supplementary information on voltage and frequency deviations. Current-source controlled VSCs are typically assumed to be connected to strong ac grids. The most distinct characteristic of the

current-source controlled VSC is that it relies on measured ac frequency by using a phase lock loop (PLL) for output synchronization. Therefore, the synchronization has to be accurate enough to deliver the desired amount of power.

The voltage-source controlled VSC is gaining popularity recently because it can set the terminal voltages, making it flexible for an ac grid. This control type regulates voltage and frequency on the ac side to the set point and, additionally, output power around the reference values. In steady-state mode, it can be modeled as an ac voltage source behind an impedance in the same vein as a synchronous generator. Power control errors can be used to modify the voltage and frequency references using, for example, droop control. While the current-source controlled VSC computes the current reference based on the power set point and the ac voltage, this type directly controls the ac voltage phase angle based on the synchronization speed reference. To adjust the output power, additional control methods have been proposed to modify the speed reference and emulate rotating generators.

4.1.1 Current-Source Controlled VSC

The fundamental control structure of a current-source controlled VSC for large-scale transient simulations is shown in Figure 4.1. This model is widely used by renewable generation systems to feed power to a strong external ac grid. Additional controllers such as maximum power point tracking (MPPT) or reactive power control are used to calculate the power references. Outer control loops are also available to adjust the power reference based on voltage and frequency deviations. Using the measured synchronizing phase angle, the VSC output current is synchronized to the ac system by an inverse Park transformation to the *abc* reference frame in a time-domain simulation, or by a phase shifter in a phasor-domain simulation.

The current-source controlled VSC exhibits high parallel output impedance and thus must work in parallel with other power sources in a strong ac grid. If the external system is weak, the capabilities of external voltage and frequency control loops are

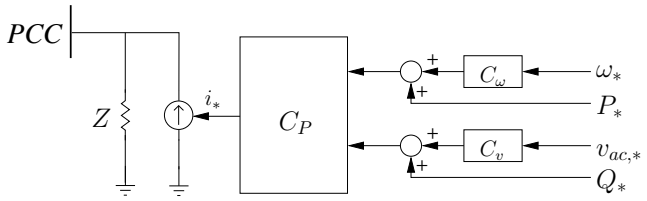


Figure 4.1: Schematic diagram of a current-source controlled VSC connection.

not guaranteed. On the other hand, if the converter is working in rectifier mode, the inner current reference can be computed to control the dc voltage. In a multi-terminal HVDC network, one converter must be configured to control dc voltage instead of ac power. The other converters can apply the droop of dc voltage on the power generation, the $v_{dc} - P$ droop, to provide feedback similar to the commonly used ac $f - P$ droop.

4.1.2 Voltage-Source Controlled VSC

Instead of relying on the external ac grid to set the voltage, as shown in Figure 4.2, the voltage-source controlled VSC is controlled as a voltage source. The output voltage and frequency are controlled directly, and additional loops are used to emulate the behaviors of a conventional ac power source. It exhibits low parallel output impedance and is connected to an ac grid, either strong or weak, through a coupling impedance. Similar to a synchronous generator, the output power is determined by the ac terminal voltage phasor, bus voltage phasor, and the coupling impedance.

The voltage-source controlled VSC does not require PLL for ac synchronization. Rather, it is capable of regulating its output voltage frequency based on the input frequency reference. Active power control is realized by increasing the output frequency, namely, leaping the voltage phasor on the VSC terminal. External control loops have been proposed to modify the frequency control loop for inertia emulation and primary frequency regulation. One issue of the voltage-source controlled VSC is that, under severe ac grid contingencies, the output current may exceed the maximum

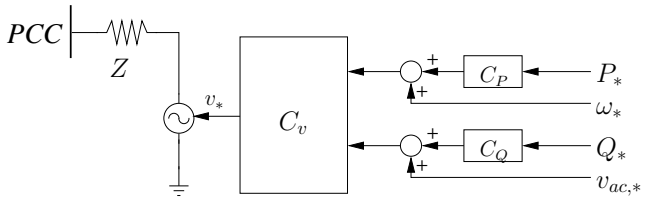


Figure 4.2: Schematic diagram of a voltage-source controlled VSC connection.

tolerable current for the device. Thus a protection such as a current limiter or a control switching method must be employed to avoid overcurrent.

4.2 Positive-Sequence Phasor-Domain Model

This section discusses the mathematical model for VSCs in large-scale phasor-domain transient simulation programs. First, the common network interface equations are derived from Park's Transformation. Then, both the current-source controlled and voltage-source controlled models are derived for different control loops. Finally, an additional loop to emulate the inertia response is proposed.

4.2.1 Network Interfaces

The single-line diagram of a bi-direction VSC interfacing the ac and dc network is shown in Figure 4.3. The ac output from the VSC is first filtered with a series reactance which blocks the high-frequency harmonics from the converter, and a shunt-connected high-pass filter which provides a low-impedance path for the remaining high-frequency harmonics. The filtered current is then interfaced to the grid through a converter transformer. The dc output from the VSC is also filtered with a shunt capacitor and a series reactance before feeding into the dc network. The current reference directions shown in the figure are used for the equations hereafter.

To deal with time-variant control settings, the ac network phasor-domain quantities are transformed into a *d-q* reference frame which rotates at the same speed as the ac voltage phasor. The Park transformation in a three-phase time-domain

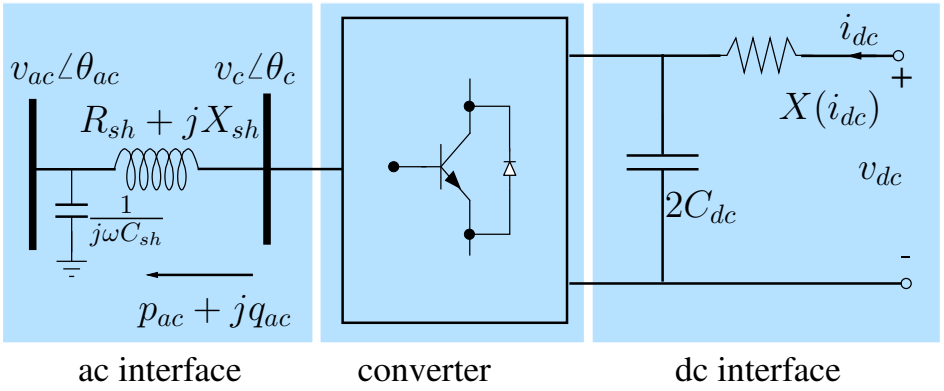


Figure 4.3: VSC interface block diagram.

becomes a phase shift in the phasor-domain given that, at the fundamental frequency, the phasors are rotating at the same speed as the d-q axis. Assuming the d axis is aligned with the ac voltage phasor, the ac quantities, including the voltage and the current, can be transformed as follows:

$$v_{ac}e^{j(\omega t+\theta_{ac})} = (v_{ac,d} + jv_{ac,q})e^{j(\omega t+\theta_{dq})} \tag{4.1}$$

where the phase shift angle θ_{dq}, depending on the control type on the ac side, is obtained from PLL or calculated from the speed reference. Note that if the phase shift in a rotating reference frame is T, in the time-domain, T is given as

$$T = e^{j(-\omega t-\theta_{dq})} \tag{4.2}$$

where θ_{dq} is the angle of the d-axis of the selected dq reference frame.

The dynamic ac side of the VSC can be transformed from the time domain into the phasor domain in the d-q reference frame. Considering the derivative of the ac current injection i_{sh}, the transformation is given as

$$\begin{aligned} T\frac{di_{sh}}{dt} &= \frac{d(Ti_{sh})}{dt} - i_{sh}\frac{dT}{dt} \\ &= \frac{d(i_{sh,d} + ji_{sh,q})}{dt} - j(\omega i_{sh,q} - \omega i_{sh,d}) \end{aligned} \tag{4.3}$$

Thus the full dynamic equations on the ac side in the d-q reference frame are

$$L_{sh}\frac{di_{sh,d}}{dt} - \omega L_{sh} i_{sh,q} = -R_{sh} i_{sh,d} + (v_{c,d} - v_{ac,d}) \tag{4.4}$$

$$L_{sh}\frac{di_{sh,q}}{dt} + \omega L_{sh} i_{sh,d} = -R_{sh} i_{sh,q} + (v_{c,q} - v_{ac,q}) \tag{4.5}$$

$$C_{sh}\frac{dv_{ac,d}}{dt} - \omega C v_{ac,q} = (i_{sh,d} - i_{ac,d}) \tag{4.6}$$

$$C_{sh}\frac{dv_{ac,q}}{dt} + \omega C v_{ac,d} = (i_{sh,q} - i_{ac,q}) \tag{4.7}$$

where $Z_{sh} = R_{sh} + jL_{sh}$ is the aggregated impedance of the high-frequency harmonics blocker at the converter ac terminal; ω is the frequency of the PCC voltage v_{ac}.

The dc network interface is relatively straightforward. Applying the Kirchoff's Current Law on the VSC dc terminal yields

$$C_{dc}\frac{dv_{dc,\pm}}{dt} = -(i_{dc} - i_c) \tag{4.8}$$

4.2.2 Current-Source Controlled VSC Modeling

The full model of a current-source type of VSC is shown in Figure 4.4. Mathematical equations are explained as follows.

Phase Lock Loop

The current-source type VSC depends on the external grid for synchronization. A phase lock loop is employed to track the ac voltage angle as the reference position of the q axis. Figure 4.5 shows the scheme of the PLL [7], which consists of a phase detector, a loop filter, and a voltage-controlled oscillator.

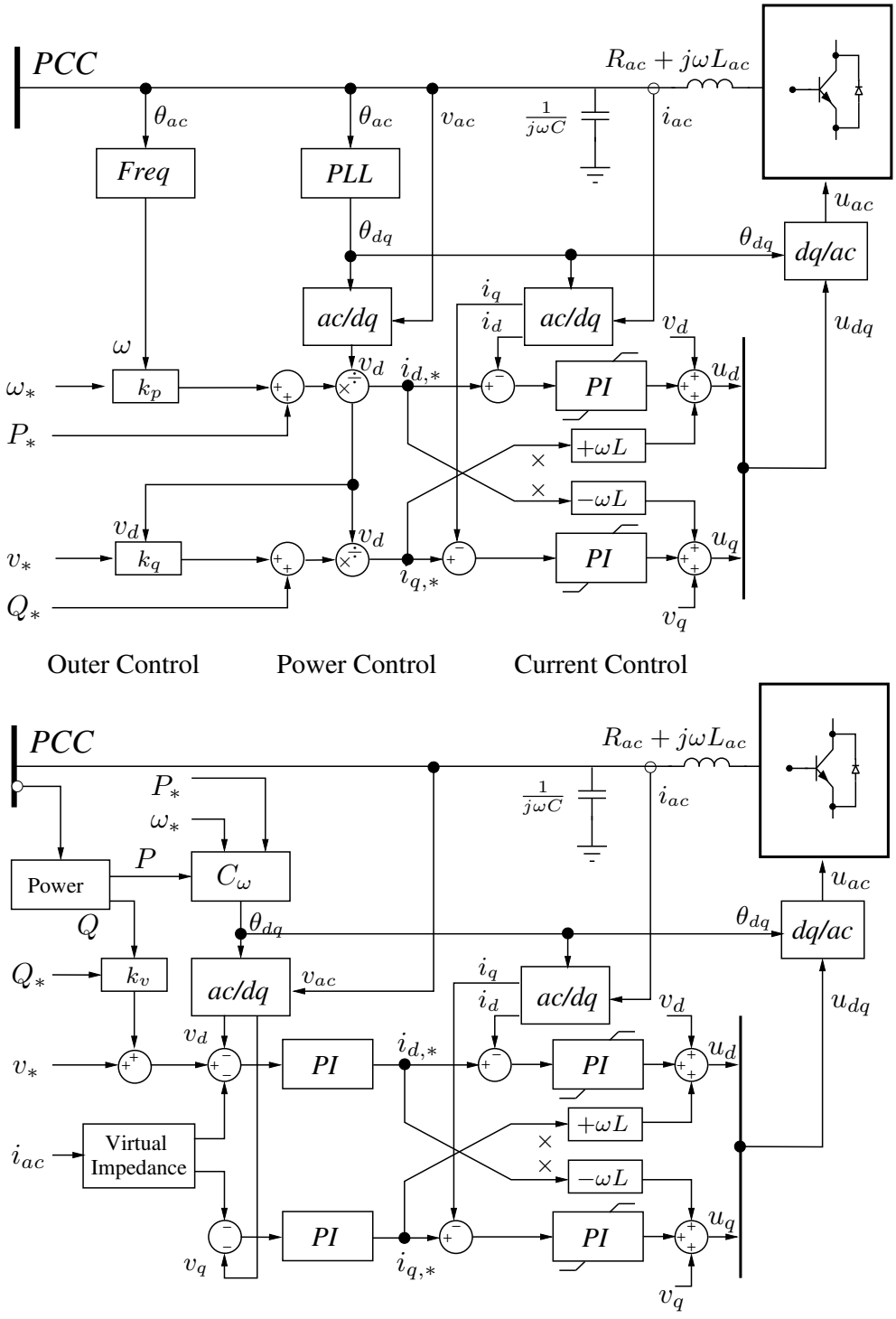


Figure 4.4: Full model of VSC interfaced to large-scale ac systems. Upper: current-source type VSC; Lower: voltage-source type VSC.

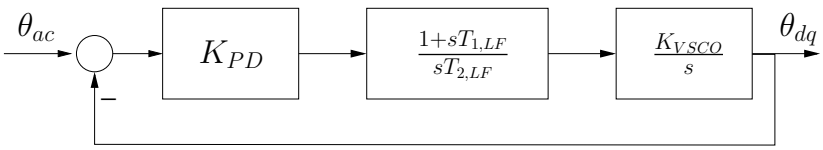


Figure 4.5: PLL block diagram.

Active Power Balance

The active power balance equation coupling the ac and the dc circuits is given as

$$v_{ac,d}i_{ac,d} + v_{ac,q}i_{ac,q} = -v_{dc}i_{dc} + p_{loss} \tag{4.9}$$

where p_{loss} is the aggregated converter switching losses.

Outer Control Loops

The outer control loops are responsible for maintaining the grid-side control quantities to the input reference values. The outputs of the outer loop is the computed current references in the *d*-*q* reference frame.

The reactive power Q_{ac} in the *d*-*q* reference frame at the PCC is given as

$$Q_{ac} = v_{ac,d}i_{sh,q} - v_{ac,q}i_{sh,d} \tag{4.10}$$

where the second term becomes zero since, under the ideal circumstance, the PLL eliminates the *q*-axis voltage component. Therefore, the *q*-axis current reference can be computed from the reactive power reference. Considering the voltage droop, the reactive power control loop is expressed as

$$Q_{ac,**} = Q_{ac,*} + k_q(v_{ac,*} - v_{ac,d}) \tag{4.11}$$

$$i_{sh,q,*} = \frac{Q_{ac,**}}{v_{ac,d}} \tag{4.12}$$

Regarding the active power, a converter can be configured to control either the *ac active power* or the *dc terminal voltage*. In the active power control mode, the inner current reference $i_{sh,d,*}$ is derived as follows. The active power P_{ac} is given by

$$P_{ac} = v_{ac,d} i_{ac,d} + v_{ac,q} i_{ac,q} \tag{4.13}$$

where the second term becomes zero if assuming perfect PLL alignment. The internal active power reference is computed considering the reference active power and the frequency droop. The full equations to compute the d-axis voltage reference frame are:

$$P_{ac,**} = P_{ac,*} + k_p(\omega_* - \omega) \tag{4.14}$$

$$i_{sh,d,*} = \frac{P_{ac,**}}{v_{ac,d}} \tag{4.15}$$

The dc voltage control mode allows the converter to control dc voltage instead of maintaining an ac active power injection. In a multi-terminal HVDC network, one converter with a large capacity is responsible for maintaining the dc voltage magnitude. It compensates for the dc power mismatches in the same way as an ac slack bus. A possible model is to adjust the dc current through a PI controlled based on dc voltage deviation:

$$i_{sh,d,*} = i_{sh,d} + (K_{p3} + \frac{K_{i3}}{s})(v_{dc,*} - v_{dc}) \tag{4.16}$$

Inner Control Loops

The inner control loops adopt vector control schemes to achieve the d-q reference frame current set point. The d-q voltage references are computed to track the current reference values using PI controllers as follows:

$$u_{c,q,*} = u_{ac,q} - \omega L i_{sh,d} + (K_{p1} + \frac{K_{i1}}{s})(i_{sh,q,*} - i_{sh,q}) \tag{4.17}$$

$$u_{c,d,*} = u_{ac,d} + \omega L i_{sh,q} + (K_{p2} + \frac{K_{i2}}{s})(i_{sh,d,*} - i_{sh,d}) \tag{4.18}$$

A delay between the voltage references and the actual values due to power electronics switching is modeled by a time delay of the time constant T_c. The relationship between the reference values and the terminal voltages is thus:

$$\begin{aligned} \dot{u}_{c,d} &= (u_{c,d,*} - u_{c,d})/T_c \\ \dot{u}_{c,q} &= (u_{c,q,*} - u_{c,q})/T_c \end{aligned} \tag{4.19}$$

4.2.3 Voltage-Source Controlled VSC Modeling

The full model of the voltage-source controlled VSC is shown in Figure 4.4. This control method was proposed by [68] as the power-synchronization control. It computes the current references, at the outer control loop, based on the voltage and frequency set points. Active and reactive power droops can be applied to modify the voltage and frequency references. The following subsections provide the outer-control loop with droop control equations of the voltage-source type VSC.

Frequency Control Loop

The frequency control loop generates the angle of the d-q reference frame based on the frequency set point. The rate of change of the hypothetical reference frame angle θ_{dq} is the frequency deviation, given as

$$\dot{\theta}_{dq} = \omega_* - \omega_s \tag{4.20}$$

A droop of active power deviation can be added as a feedback to frequency:

$$\dot{\theta}_{dq} = \omega_* + k_p(P_{ac,*} - P_{ac}) - \omega_s \tag{4.21}$$

Voltage Control Loop

The other outer control loop serves to enforce the terminal voltages on the ac bus. The converter currents are computed to align the ac voltage phasor to the d-axis and eliminate the q-axis component.

$$i_{sh,d,*} = i_{sh,d} + (K_{p4} + \frac{K_{i4}}{s})(v_{ac,**} - v_{ac,d} - i_{ac,d}R) \tag{4.22}$$

$$i_{sh,q,*} = i_{sh,q} + (K_{p5} + \frac{K_{i5}}{s})(-v_{ac,d} - i_{ac,d}R) \tag{4.23}$$

Similarly, a droop of reactive power deviation can be added:

$$v_{ac,**} = v_{ac,*} + k_q(Q_{ac,*} - Q_{ac}) \tag{4.24}$$

4.2.4 Possible Simplifications

Simplifications to reduce the model complexity are practical for simulation in large-scale systems. The aforementioned transient model of VSC is indeed simplified from the detailed switching model used in electromagnetic transient simulators. The transient model can be further simplified by neglecting the existing fast dynamics, namely, the states associated with small time constants, on both the ac and dc sides.

AC Interface

On the ac side, the shunt capacitance is used to filter out the high-frequency components in inverter output. This capacitor filter is commonly neglected in transient simulations, which are on the fundamental frequency. This simplification eliminates (4.6) and (4.7). Also, for the current-source controlled VSC, assuming that the angle tracking is fast enough so that $\theta_{ac} = \theta_{dq}$, the PLL can also be neglected.

DC Interface

If the study is focused on ac system responses, the fast dynamics of the dc shunt capacitor can be neglected, which leads to the drop of (4.8). Nevertheless, in real systems, the dc capacitance is one of the most important factors for its transients. The simplification of dc capacitance is practical only when necessary and justified.

Inner Current Control Loops

The converter terminal voltage dynamics can be simplified by neglecting the power electronic converter response time, namely, $T_c = 0$. This will render the ac terminal voltage $v_{c,d}$, $v_{c,q}$ be the reference value $v_{c,d,*}$, $v_{c,d,*}$ without delay. Equation (4.19) can be dropped and $v_{c,d}$, $v_{c,q}$ will become algebraic variables.

The PI-controller based inner current control loops can be simplified with a low-pass filter that imposes a delay. The output of the transfer function which tracks the input current references and yields the terminal voltages are given as follows to replace equations (4.18), (4.17) and (4.19).

$$i_{ac,d} = \frac{1}{1 + sT_{id}} \times i_{ac,d,*} \tag{4.25}$$

$$i_{ac,q} = \frac{1}{1 + sT_{iq}} \times i_{ac,q,*} \tag{4.26}$$

$$v_{c,d,*} = v_{ac,d} + i_{ac,d}R_{sh} - i_{ac,q}X_{sh} \tag{4.27}$$

$$v_{c,q,*} = v_{ac,q} + i_{ac,q}R_{sh} + i_{ac,d}X_{sh} \tag{4.28}$$

$$v_{c,d} = \frac{1}{1 + sT_{vd}} \times v_{ac,d,*} \tag{4.29}$$

$$v_{c,q} = \frac{1}{1 + sT_{vq}} \times v_{ac,q,*} \tag{4.30}$$

$$v_c = v_{c,d} + jv_{c,q} \tag{4.31}$$

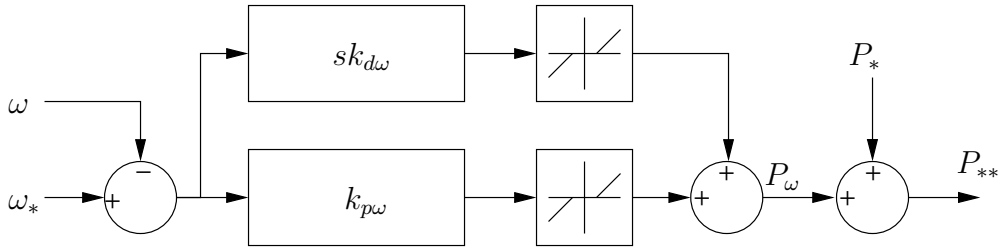


Figure 4.6: Inertia emulation control loop for current-source VSC.

4.2.5 Modeling Local Frequency Control for VSC

As an electronically controlled high-power device, VSC has zero rotating mass. Under severe ac grid contingencies, the VSC is not able to release the kinetic energy, which is equivalent to the inertia, stored in the rotating mass to compensate for the immediate power mismatch like a conventional generator. From the ac perspective, a network with high VSC integration will thus have little inertia and, in the event of a fault, the change of frequency will be rapid. Extensive research has been carried out to emulate the inertia of conventional generators by associating the power reference with grid frequency [55].

Current-Source Controlled VSC

For current-source type interfaces, an additional differential term of the frequency variation is added to the primary frequency droop in the active power controller, as shown in Fig. 4.6, where $k_{d\omega}$ is the coefficient of the frequency differential for inertia emulation, and k_{pw} is the primary frequency control droop [47]. The dead-bands after the droop and the differential blocks are optional to avoid frequent active power adjustments around the nominal frequency. The active power reference value is then adjusted and will be reflected in the calculated $i_{d,*}$ for the inner current control loop.

Since the active power reference goes through the power control loops, which also depend on the ac voltage, the inertia emulation response is not guaranteed. The actual incremental power output depends on the active power margin from the dc side through de-loading or rotor-side inertia response. An analytical model to estimate the

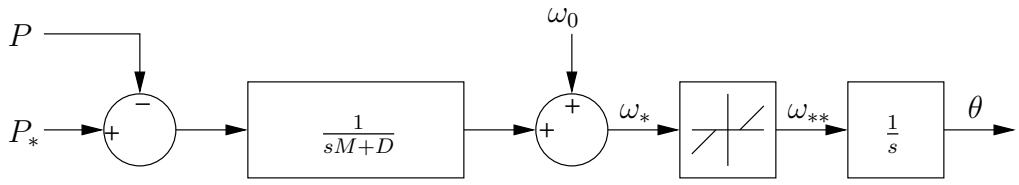


Figure 4.7: Inertia emulation control loop for voltage-source VSC.

frequency regulation performance of inertia emulation and droop control is discussed in [28] based on an average low-order system frequency response (SFR) model [57]. A performance guaranteed method is proposed in [70] using model reference control for current-source type VSCs to deliver the desired amount of inertia in microgrids along with a controllable diesel generator, based on the wind generator model in [49].

Voltage-Source Controlled VSC

For voltage-source type converters, an analytical approach can be applied to derive the speed reference for the desired inertia value. The method manipulates the synchronous generator swing equation to derive the equation for speed reference, which is briefly shown as follows.

The Laplace transformation of (4.32) yields (4.33):

$$M\frac{d\omega^*}{dt} = P_* - P - D(\omega^* - \omega_0) \tag{4.32}$$

$$P_* - P = Ms\omega^* + D(\omega^* - \omega_0)f \tag{4.33}$$

The speed reference to emulate a generator with time constant M is given as

$$\omega^* = \omega_0 + \frac{1}{1+sT}\frac{P_* - P}{D} \tag{4.34}$$

where $T = \frac{M}{D}$ is the time constant of the first-order inertia transfer function. When $T = 0$, the synchronous generator inertia emulation control becomes the conventional power droop control. The diagram of the controller is shown in Fig. 4.7.

Table 4.1: MT-HVDC VSC Set Points

VSC Number	Bus Number	First Control Variable	Second Control Variable	V_{shmax}	V_{shmin}	I_{shmax}
1	1	$v_{dc} = 1.0$	$V = 1.06$	1.1	0.95	0.5
2	2	$P = -0.2$	$Q = -0.01$	1.1	0.95	0.5
3	13	$P = 0.2$	$Q = 0.01$	1.1	0.95	0.5
4	14	$P = 0.2$	$V = 1.02$	1.1	0.95	0.5

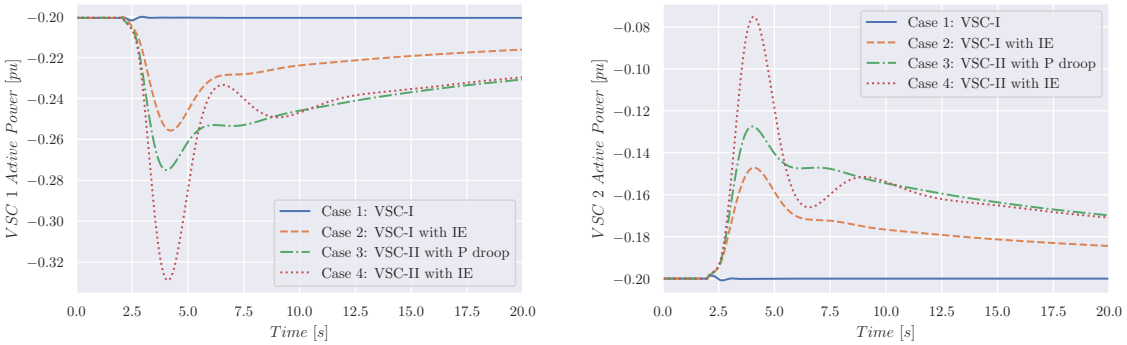
4.3 Dynamic Response of the Proposed Models

Simulation studies are carried out to evaluate the performance of the proposed VSC models implemented on the LTB Andes simulation platform. The IEEE 14-bus system is used in the illustrative studies. Generators of the 6th-order model, turbine governors, voltage regulators, and power system stabilizers are included in the 14-bus dynamic model. Four VSC stations are constructed to transfer power from Buses 1 and 2 to Buses 13 and 14 through the dc network, the same topology as in the last chapter. The control parameters are given in Table 4.1.

An instant load ramping event is imposed on Bus 2 at $t = 2.0s$. This section compares the system dynamic response for the following cases:

1. Four current-source controlled converters (VSC-I)
2. Four current-source controlled converters (VSC-I), VSC 2 on Bus 2 equipped with inertia emulation (IE)
3. Three current-source controlled (VSC-I) on Buses 1, 13, 14, and one voltage-source controlled converter (VSC-II) with active power droop on Bus 2;
4. Three current-source controlled (VSC-I) on Buses 1, 13, 14, and one voltage-source controlled converter (VSC-II) with IE on Bus 2;

First, the active power on VSC 1 and VSC 2 are shown in Figure 4.8a and Figure 4.8b. In the MT-HVDC set up, since VSC 1 controls the dc voltages as a



(a) Active power output at VSC 1 and VSC 2 **(b)** Active power output at VSC 2

Figure 4.8: Active power output at VSC 1

slack converter, the inertial power withdrawn by VSC 2 have to be supplied by VSC 1. Observations are as follows:

1. In Case 1, VSC 2 is a current source drawing constant power from Bus 2 and not responding to the load ramping event. Nevertheless, the tiny active power fluctuation is due to the ac voltage ripple.

2. In Case 2, the droop of frequency deviation and ROCOF modifies the power reference and therefore reduces the active power drawn from Bus 2.

3. Comparing Case 3 with Case 4, the initial active power reduction in the first two seconds is higher in Case 4 because of the inclusion of the integral term in (4.34).

4. When the time window of inertial response has passed, namely, after the eighth second, Case 3 and Case 4 have a similar active power curve due to the frequency droop.

The second variable to compare is the dc voltage. In all cases, only VSC 1 at Bus 1 is controlling the dc voltage. Given the low resistance and small capacitor sizes in the dc network, all the dc nodes exhibit similar voltage patterns. The dc voltage of Node 1 where VSC 1 is connected is shown in Figure 4.9. It is observable that Case 2

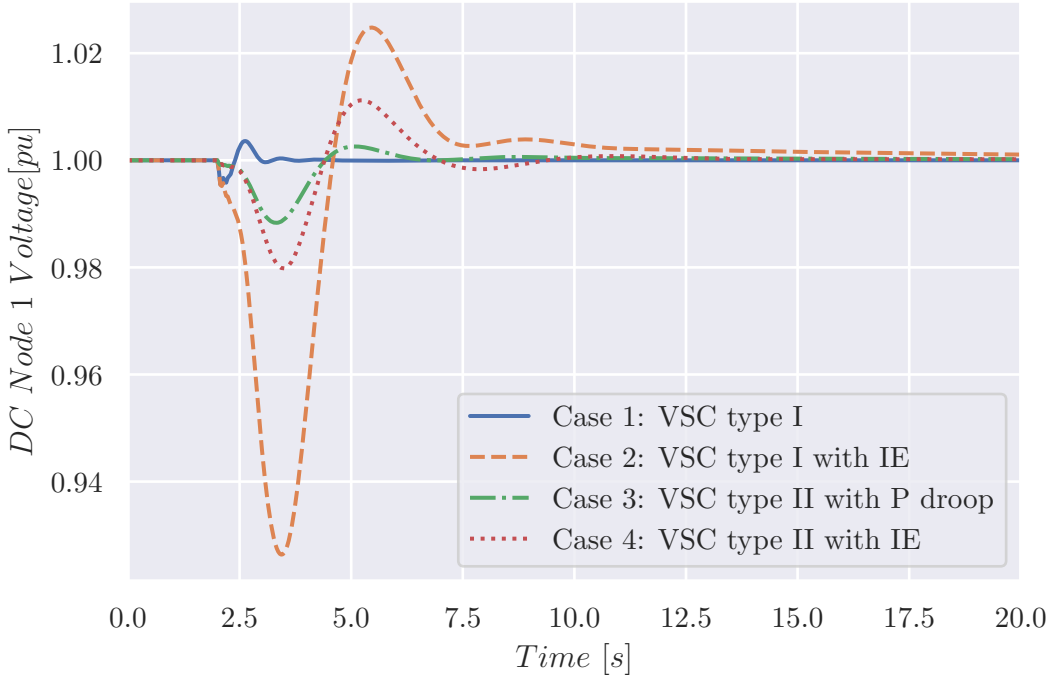
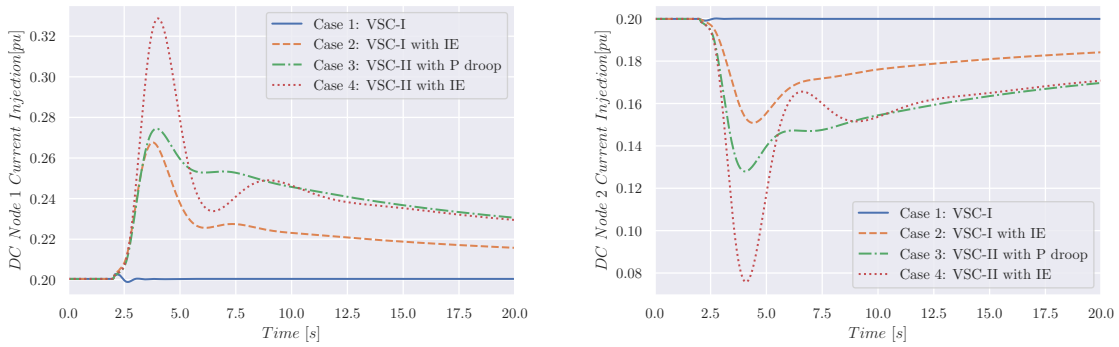


Figure 4.9: DC voltage at Node 1

has the most severe dc voltage drop. The explanation can be seen from the dc current injection changes at Node 1 and Node 2.

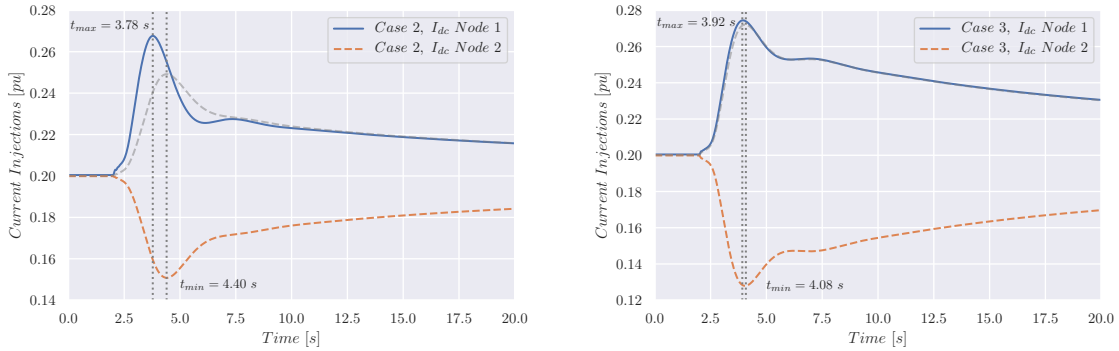
In the event of load ramping, as seen in Figure 4.10b, the current injections at Node 2 reduce in all the cases. Since VSC 3 and VSC 4 are absorbing constant power from the dc grid, the power deficits must be compensated by VSC 1, which have to reduce the dc voltage in order to raise the dc current. The dc current injections on Nodes 1 and 2 in Case 2 are shown in Figure 4.11a, where the unlabeled light grey curve is the mirror of the dashed curve.

In Case 2, there is a noticeable delay between the changes in active power reference and the dc current injection. The delay causes VSC 1 to further reduce the dc voltage so as to achieve a power balance. Nevertheless, in Case 3 as shown in Figure 4.11b, the change in current at Node 1 and Node 2 are synchronized, and the dc voltage drop is low.



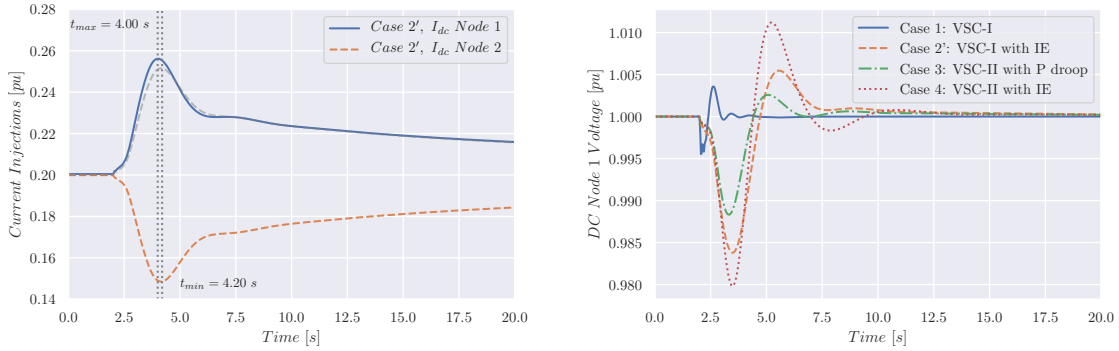
(a) Current injection at Node 1 **(b)** Current injection at Node 2

Figure 4.10: Current injections at Nodes 1 and 2



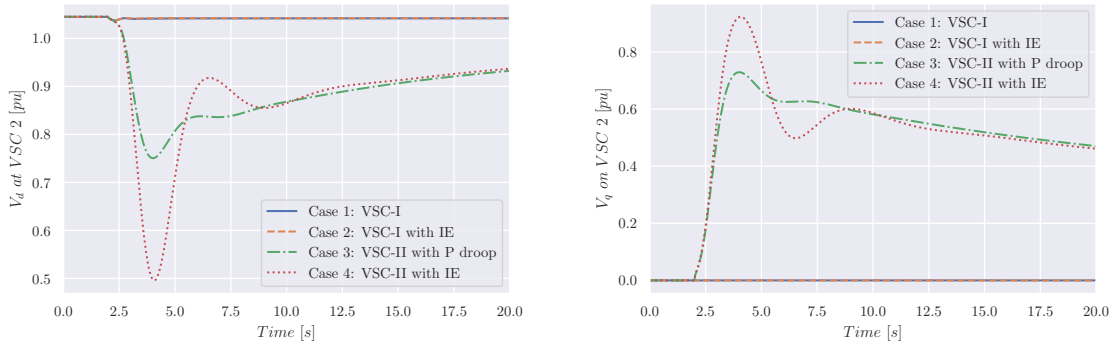
(a) Case 2 nodal current injection **(b)** Case 3 nodal current injection

Figure 4.11: Nodal current injections at Nodes 1 and 2 in Case 2 original parameters



(a) Case 2′ nodal current injection **(b)** Nodal voltage comparisons

Figure 4.12: Nodal current injections at Node 2 and the voltage profiles. Case 2´ uses modified parameters.



(a) d-axis ac voltages **(b)** q-axis ac voltages

Figure 4.13: ac voltages in the dq-axis

The voltage drop in *Case 2* can be corrected by adjusting the PI controller gain for the dc voltage. By changing K_{p2} from 0.5 to 1.5 and K_{i2} from 0.5 to 2, the peak of I_{dc} at Node 1 can be shifted to the same phase as I_{dc} at Node 2. The results with the new parameters are denoted as $Case2'$ and shown in Figure 4.12b.

Finally, the ac voltages in the dq-axis are shown in Figure 4.13. In Cases 1 and 2, the voltage components follow the ac grid voltage phasor. Compared to Case 3, Case 4 adds the inertial term on the speed reference and thus modifies the ac voltage components.

4.3.1 Conclusions

In this chapter, two types of transient models for VSC in MT-HVDC networks are modeled and studied. The current-source controlled VSC, namely, VSC-I is synchronized to the ac grid and can be seen as a current source from the ac grid. The voltage-source controlled VSC, VSC-II, is controlled as a synchronous machine that generates its own speed references.

Although both types of converter models can emulate the inertial response of the synchronous generator, the mechanism and response characteristics differ. VSC-I depends on frequency and ROCOF droop to modify the active power reference, while

VSC-II computes the speed reference based on the ac active power change. It is worth noting that VSC-I may cause a more severe voltage drop, while VSC-II may result in higher converter current changes.

Chapter 5

Provision of Emulated Inertia Through HVDC Networks

In recent years, large-scale wind farms have been built offshore due to wind resource availability and onshore land saving. These offshore wind farms are typically configured as a current source to inject active power into the ac grid and control the terminal voltage.

This chapter models the Type IV wind generator for offshore wind farms. Wind farms are connected to the ac main grid through multi-terminal dc systems. Local and remote sensing based controls are proposed for the wind farms to provide inertial and frequency support for the main grid.

5.1 Modeling of Type IV Wind Generators

A type IV wind generator consists of a wind turbine, and a Permanent Magnetic Synchronous Generator (PMSG) connected to a pair of back-to-back full-capacity VSCs.

5.1.1 Aerodynamics and Turbine Model

Based on aerodynamics, mechanical power extracted from wind power by the wind turbine is represented by

$$P_t = \frac{1}{2}\rho\pi R_t^2 v_w^3 C_p(\lambda, \theta_t) \tag{5.1}$$

where v_w, R_t, ρ, θ_t, and ω_t are the wind speed input, blade radius, air density, rotor blade pitch angle, and the wind turbine angular speed. The C_p output characteristic is approximated by

$$C_p = 0.22(\frac{116}{\lambda_i} - 0.4\theta_p - 5)e^{-\frac{12.5}{\lambda_i}} \tag{5.2}$$

with λ_i given by

$$\frac{1}{\lambda_i} = \frac{1}{\lambda + 0.08\theta_p} - \frac{0.035}{\theta_p^3 + 1} \tag{5.3}$$

and the speed tip ratio λ given as

$$\lambda = \frac{v_{tip}}{v_w} = \eta_{GB}\frac{2R\omega_t}{n_{pole}v_w} \tag{5.4}$$

For modern wind turbines, assuming a rigid shaft model, namely, $\omega_m = \omega_t$, the turbine motion equation is given as

$$2H\dot{\omega}_m = \tau_t - \tau_e \tag{5.5}$$

where τ_t, τ_e, and H are the mechanical torque, the electric torque, and the total inertia. The mechanical torque is calculated from the wind power input and rotor speed, given as

$$\tau_t = \frac{p_w}{\omega_t} \tag{5.6}$$

5.1.2 Pitch Angle Control and Maximum Power Tracking

Pitch angle control is designed to avoid super-synchronous speed in high wind speed scenarios. The pitch angle, θ_p is modeled as a state variable to track the pitch angle

setpoint, given as:

$$\dot{\theta_p} = (K_P * \phi(\omega_m - \omega^{ref}) - \theta_p)/T_p \tag{5.7}$$

where ϕ is a step function which is only sensitive to variations larger than a predefined step. Then, the output pitch angle goes through an anti-windup limiter which sets the minimum pitch angle to zero.

Speed control maximizes the power extraction from the wind turbine by changing the active power setpoint based on maximum power condition. This is also known as maximum power point tracking (MPPT). For each wind speed and pitch angle, there exists an optimal turbine speed ω_t^* which satisfies

$$\frac{dp_w(\omega_t^*, v_w, \theta_p)}{d\omega_t} = 0 \tag{5.8}$$

The power generation $p_w(\omega_t^*, v_w, \theta_p)$ is the maximum power point under the wind speed v_w and pitch angle θ_p. Assuming $\theta_p = 0$, the maximum power point can be approximated by a piece-wise linear function given by

$$p_w^*(\omega_t) = \begin{cases} 0 & (\omega_t < 0.5) \\ 2\omega_m - 1 & (0.5 \leq \omega_t \leq 1) \\ 1 & (\omega_t > 1) \end{cases} \tag{5.9}$$

This MPPT function imposes a lower limit of zero when the turbine speed drops below 0.5 pu. It also caps the upper limit to 1 pu in super-synchronous cases to avoid generator overloading.

5.1.3 Generator Model

The transient model assume that the converter dynamics are rapid and therefore can be neglected. The VSCs decouple the generator from the main grid. Power production

from the generator depends on the generator-side voltage and current, given as

$$p_s = v_{s,d} i_{s,d} + v_{s,q} i_{s,q} \tag{5.10}$$

$$q_s = v_{s,q} i_{s,d} - v_{s,d} i_{s,q} \tag{5.11}$$

The machine equations in steady state are

$$v_{s,d} = -r_s i_{s,d} + \omega_m x_q i_{s,q} \tag{5.12}$$

$$v_{s,q} = -r_s i_{s,q} - \omega_m (x_d i_{s,d} - \psi_p) \tag{5.13}$$

where ψ_p is the rotor-side permanent field flux.

The power injections into the grid depend on the grid-side voltage and the converter current, given as

$$p_c = v_{c,d} i_{c,d} + v_{c,q} i_{c,q} \tag{5.14}$$

$$q_c = v_{c,q} i_{c,d} - v_{c,d} i_{c,q} \tag{5.15}$$

Assuming perfect PLL tracking, the voltage phasors of the main grid, $v_{c,d}$ and $v_{c,q}$ can be calculated from

$$v_{c,d} = -v_h sin\theta_h \tag{5.16}$$

$$v_{c,q} = v_h cos\theta_h \tag{5.17}$$

5.1.4 VSC Controller

The back-to-back VSCs decouple the generator from the main grid for independent controls. The converters can regulate the dc link voltage and reactive power generation on the generator side while controlling the active power and the ac voltage on the grid side. These control effects are achieved by controlling the converter currents $i_{s,d}$, $i_{s,q}$, $i_{c,d}$, $i_{c,q}$. The following control paradigm is adopted [44].

Let the generator-side converter track the optimal active power and control reactive power generation:

$$\dot{i}_{s,d} = \frac{1}{T_{sd}}(K_{sd}(q_{s0} - q_s) - i_{s,d}) \tag{5.18}$$

$$\dot{i}_{s,q} = \frac{1}{T_{sq}}(\frac{p_s^{ref}}{\omega_m(\psi_p - x_d i_{s,d})} - i_{s,q}) \tag{5.19}$$

where q_{s0} is the reactive power computed from the power flow solution, and p_s^{ref} is the computed active power set point on the generator side. In general, $p_s^{ref} = p_w^*(\omega_m) + \Delta p$, which is the MPPT function defined in (5.9).

Let the grid-side converter control the dc link power extraction and the ac voltage:

$$\dot{i}_{c,d} = (K_{cd}(v^{ref} - v_h) - i_{c,d})/T_{cd} \tag{5.20}$$

$$\dot{i}_{c,q} = (K_{cq}(p_s - p_c) - i_{c,q})/T_{cq} \tag{5.21}$$

where v^{ref} is the ac voltage set point.

5.1.5 Inertia Emulation Control

The inertia emulation control loop modifies the active power set point in the event of a detected ac grid frequency excursion. The wind generator can push inertial mechanical power out of the turbine by increasing the generator-side converter current and, consequently, reduce the turbine generator speed. Some literature also explores different modes for wind turbines under various operating conditions [66].

The implementation of an inertial emulation controller does not require the modification of the existing VSC control model. Instead, it is an add-on controller that provides an output signal, $p_i(f_h)$ for adjusting the active power reference, p_s^{ref}, of the generator-side converter. Ideally, the power adjustment is proportional to the

rate-of-change of frequency (ROCOF) of bus h:

$$\Delta p = p_i(f_h) = K_p \frac{d\Delta f_h}{dt} \tag{5.22}$$

where the frequency of bus h can be obtained, depending on the installation site of the wind generator, locally or remotely. If the wind generator is installed onshore, the wind generator should monitor the frequency on the collector bus. If the wind generator is installed offshore, the frequency value passing could utilize the dc network or a communication network [58, 71].

In real systems, the ROCOF measured by PMUs is hardly accurate. During transitions, power system noise and harmonics could invalidate the ROCOF measurements, especially during a short time window.

5.1.6 Simplified Off-Shore Wind Generators

There are cases where wind generator output is connected to dc networks through an extra level of power converter, such as large-scale distributed offshore wind farms. Assuming the time constants for the VSC controllers are negligible, the Type IV wind generator model can be simplified to a turbine generator model and a generator-side converter model. Equations (5.14), (5.10), (5.16), (5.17), (5.20) and (5.21) can be excluded. In addition, the current injection to the dc grid is calculated as

$$i_{dc} = p_s/(v_1 - v_2) \tag{5.23}$$

where v_1 and v_2 are the dc voltages on both terminals of the connection.

5.2 Inertia Emulation Controllers

Converters can be controlled individually to emulate inertia response, as discussed in the previous chapter. The MTDC network, therefore, becomes the medium for

transferring power and sharing inertia among the connected areas. This section will discuss the local and wide-area inertia emulation controllers for differently controlled dc components.

5.2.1 Local Signal Based Inertia Emulation

In the MTDC topology, one of the converters, known as the secondary, is in charge of controlling the dc voltage, while the other converters, the primary ones, are to control the ac power injections. The inertia emulation controllers, therefore, have to be designed differently. For the active power controlling converters, inertia emulation is performed by modifying the active power reference in the same vein as (5.22). Nevertheless, the extra power comes at the cost of reduced capacity to control the dc voltage by the primary converter. In other words, if the secondary converter injects less power into the dc network, the dc voltage reference must be reduced to maintain stability:

$$\Delta V_{dc} = K_p(P - P_0) \tag{5.24}$$

For the converter controlling the dc voltage, inertia emulation can only be done by modifying the dc voltage reference so that the power flow injection into the dc node increases. The application of a ROCOF droop on V_{dc} with the coefficient K_i is given by

$$\Delta V_{dc} = K_i \frac{d\Delta f_h}{dt} \tag{5.25}$$

The additional power for the inertia response has to be supplied by other components through the dc network. If a frequency excursion happens in the area where the active power is controlled, the extra power demand for emulated inertia will cause a dc voltage drop and therefore be compensated by the secondary converter. Interestingly, if frequency dives in the area with a secondary converter, additional power will not be supplied by other primary converters unless an additional signal is comprehended.

The additional signal can be local, such as dc voltage, or wide-area, such as remote frequency. Given the simplicity and effectiveness of droop control, for the primary converters a dc voltage droop on the active power reference (4.14) is necessary as a negative feedback:

$$\Delta P_{ref} = K_{dc}(V_{dc} - V_{dc0}) \tag{5.26}$$

where K_{dc} is the droop coefficient, and V_{dc0} is the dc voltage initial value. Note that the sign of K_{dc} depends on the direction of power flow, namely, the sign of P_{ref}. K_{dc} should be positive if the converter is feeding power into the ac grid, otherwise negative if the converter is absorbing power from the grid.

Accordingly, the secondary converter can modulate the amplitude of the reference dc voltage by imposing the ROCOF. With a droop coefficient of K_r, the voltage reference is modified by

$$\Delta V_{dc} = K_r \frac{d\Delta f_h}{dt} \tag{5.27}$$

The advantage of local signal based methods are [58, 42]:

1. Simplicity in implementation, as the local dc voltage can be readily measured,
2. Robustness in performance, as only local measurements are involved.

The disadvantages are, however,

1. *Normal* and *disturbed* operation modes must be distinguished to select the proper droop. Converters should operate in $P - V_{dc}$ droop in normal mode and must switch to $f - V_{dc}$ droop in disturbed mode. This can be implemented by a dead band of frequency deviation, for instance, $\pm 20\ mHz$.
2. A change in power reference P_{ref} to modify the converter setting will affect the dc voltage and may trigger *disturbed* mode for the interconnected areas. Converters in the disturbed areas will switch to $f - V_{dc}$ droop and drift from the power reference point.

3. The total amount of extra power demand is set by the converter in the area where a frequency event happens (denoted as the "destination converter"). Nevertheless, the distribution of the extra power demand by other source converters is highly dependent on the dc network topology, parameters, and converter droops.

5.2.2 Wide-Area Signal Based Inertia Emulation

In a monitored wide-area network, the frequency and ROCOF signals can be transmitted to other areas through communication networks. Wide-area signals can be complementary to local dc voltage signals in adjusting the references for inertia response. For an active power controlled VSC, the ROCOF signals of other areas can be utilized to modify P_{ref} as

$$\Delta P_{ref} = \sum_{j=1,..,n}^{j \neq i} K_{i,j} \dot{f}_j \tag{5.28}$$

where $K_{i,j}$ is the droop coefficient of the ROCOF in area j on $P_{i,ref}$. The sign of $K_{i,j}$ is positive when $P_{i,ref}$ is negative, or vice versa.

For a secondary converter controlling the dc reference voltage, the ROCOF droop can be applied to V_{dc} similarly as

$$\Delta V_{dc} = \sum_{j=1,..,n}^{j \neq i} K_{dc,j} \dot{f}_j \tag{5.29}$$

where the sign of $K_{dc,j}$ is positive when $P_{i,0}$ is positive, or vice versa.

Although the source converters are able to increase the power output in response to frequency events, it is important to note that the total amount of power to be extracted is determined by the destination converter, which updates its reference value based on the local measurement.

5.3 Provision and Allocation of Inertia Response

In the dc voltage droop based method, an important and interesting topic is to estimate the amount of inertia converters can emulate, the amount of power needed for the inertial response, and the allocation of the needed power. This subsection proposes an approximation of the power absorption by the converter in need, along with an approach to allocate the power among the offshore wind farms.

Consider a dc network with two Node. VSC 1 in Area 1 connects to Node 1, controlling the dc node voltage and its ac bus voltage. VSC 2 in Area 2 controls the ac voltage magnitude and the power generated by the connected PMSG. If an event happens in Area 1, the ROCOF in Area 1, specifically on the bus where VSC 1 is connected, will reflect as a command to reduce the dc voltage based on (5.27). It will affect the dc current reference and be actuated with a change in the inner current control loop.

Consider the power absorption on VSC 1 and neglect the converter losses as the multiplication of dc voltage and current:

$$P_{VSC1} = -V_{dc1} I_{dc1} \tag{5.30}$$

where the negative sign indicates current injection into the converter. Linearize the equation around the steady state yields:

$$\Delta P_{VSC1} = -V_{dc1} \Delta I_{dc1} - I_{dc1} \Delta V_{dc1} \tag{5.31}$$

In (5.31), $-V_{dc1}\Delta I_{dc1}$ is the extra power the converter can absorb by increasing its current injection, while the $I_{dc1}\Delta V_{dc1}$ is the amount of power the converter fails to absorb due to dc voltage drop.

5.3.1 Maximum Extractable Inertial Power

Assuming that the dc current tracking dictated by the dc voltage deviation is fast enough and ignoring the integral term due to the relatively short time period, the dc current can be approximated by

$$\begin{aligned} \Delta I_{dc1} &\approx (V^*_{dc1} - V_{dc1})K_{p3} \\ &= (K_i \frac{df_1}{dt})K_{p3} \end{aligned} \tag{5.32}$$

If the power supply from VSC 2 is adequate and rapid, the dc current control will stabilize before a significant dc voltage drop, which yields $\Delta V_{dc1} = 0$. Letting the converter operate with nominal power initially, the maximum inertial power VSC 1 can absorb is calculated by substituting (5.32) in (5.31):

$$\Delta P_{VSC1} = K_i K_{p3} \frac{df_1}{dt} \tag{5.33}$$

Comparing (5.33) with the generator swing equation (5.34)

$$2H \frac{d\omega}{dt} = \Delta P \tag{5.34}$$

it is observable that the the emulated inertia H_{VSC1} at VSC 1 is

$$H_{VSC1} = \frac{1}{2} K_i K_{p3} \tag{5.35}$$

5.3.2 Power Reduction Due to DC Voltage Drop

If the output of VSC 2 does not ramp either fast enough or adequately enough, VSC 1 will continue reducing the dc voltage in order to increase the current injection. On the other hand, the voltage reduction will have a droop effect on the inertial power.

Considering the output of VSC 2 as in (5.26), which is a power droop based on dc voltage deviation, the power balance between VSC 1 and VSC 2 can be given as

$$K_{p3}K_i\frac{df_1}{dt} + \Delta V_{dc1}I_{dc1} = \Delta V_{dc2}K_{dc} \tag{5.36}$$

which can be extended to a multi-terminal dc network where terminals $j = 2, ..., n$ respond to the dc voltage deviation collectively:

$$K_{p3}K_i\frac{df_1}{dt} + \Delta V_{dc1}I_{dc1} = \sum_{j=2}^{n} \Delta V_{dcj}K_{dcj} \tag{5.37}$$

Assuming that the dc voltage drops $\Delta V_{dci} \approx \Delta V_{dc1}, j = 2, ..., n$, the dc voltage drop can be calculated as

$$\Delta V_{dc} = \frac{K_{p3}K_i}{\sum_{j=2}^{n} K_{dcj} + I_{dc1}} \times \frac{df_1}{dt} \tag{5.38}$$

where I_{dc1} is the dc current in per unit value at the linearization point. It can be observed that the dc voltage deviation is determined by the sensitivity coefficient (K_{dcj})

5.3.3 Allocation of Inertial Power

The inertial power response from areas outside the contingent area depends on their sensitivity on the dc voltage change. To allocate the inertial response from multiple areas, an extra signal is needed to adjust the power references on the supporting converters. The extra signal can be transported via communication channels, and the generation of the signal can be centralized or decentralized.

The goal of inertial power allocation is to have the converters contribute the desired percentage of power, which results in coordination between the converters. The centralized approach to generating the signal can be done by communicating the active power demand, (5.33), at the secondary (receiving) converter, and letting each sending converter compute its share. Although the centralized method offers more accuracy in computing the power, it is prone to $N - 1$ failures and could be jeopardized by communication delays.

The alternative approach is to use decentralized control which does not rely on a single source for control signals. Each converter in the system can communicate necessary information with other converters to achieve a consensus. Assume that converter i is set to share ρ_i percent of actual inertial power, the power-sharing percentages can be achieved by sending to converter *i+1*: a) the desired share of converter i, and b) the current inertial power deviation, ΔP_i, defined as

$$\Delta P_i = P_i - P_{i,0} \tag{5.39}$$

The receiving *i+1*-th converter modifies the local inertial response in (5.26) with a correction term based on the received information. Ideally, the inertial response from converters i and j should satisfy

$$\frac{\rho_{i+1}}{\rho_i} = \frac{\Delta P_{i+1}}{\Delta P_i} \tag{5.40}$$

Therefore, the correction term to be added at converter *i+1* is calculated with

$$\Delta P'_{ref,i+1} = \Delta P_i - \frac{\rho_{i+1}}{\rho_i} \Delta P_{i+1} \tag{5.41}$$

The diagram of the proposed decentralized control is shown in Figure 5.1.

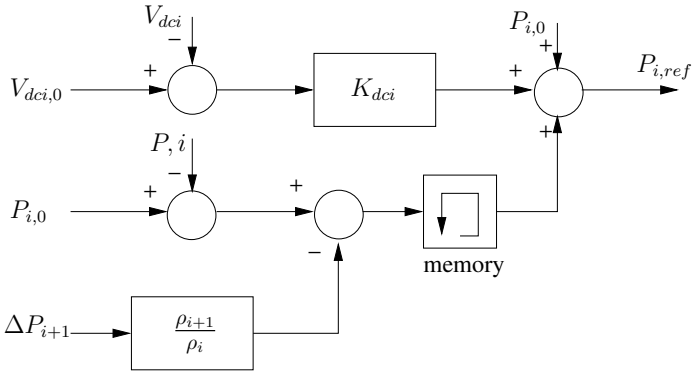


Figure 5.1: Decentralized inertial power allocation controller on converter i

5.4 Case Studies

5.4.1 Test System Setup

To better understand the inertia response across the dc network, a multi-area test system is created by linking two IEEE 14-bus islands with two offshore wind farms using a four-terminal MTDC. Two current-source controlled VSC inverters are installed at Bus 1 in Area 1 (denoted as Bus 1-1) and Bus 2 in Area 2 (denoted as Bus 2-2). Each of the two Type IV wind generators has a generator-side converter with a direct connection to the MTDC network. Note that in each independent ac system, Bus 1 has a high-capacity slack generator, and Bus 2 has a small generator initially with $P_g = 0.4\ pu$. An illustration of the test system can be found in Figure 5.2.

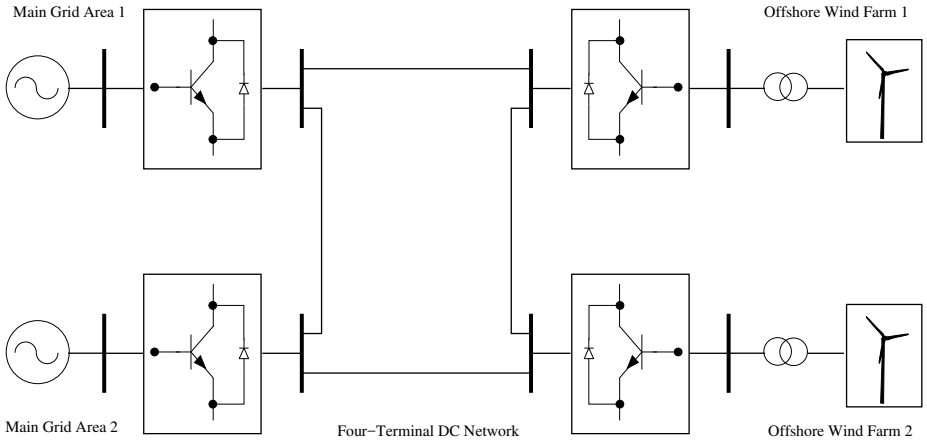


Figure 5.2: Illustration of the four-area, four-terminal test system

The control settings of the dc terminals are: *a*) VSC 1: $V_{ac} = 1.06$, $V_{dc} = 1.0$, *b*) VSC 2: $P = 0.4$, $Q = 0$, *c*) WTG 1 and WTG 2: $P_s = 0.4$. At the initial wind speed, the active power generation by each of the wind turbines is 0.4 *pu*. VSC 2 absorbs exactly 0.4 *pu* of active power and VSC 1 slightly less, at 0.399 *pu*, due to dc losses.

The event to trigger the frequency drop is a load ramping of $0.4pu$ at Bus 12 in each island, respectively. Given the different active power control methods, the inertia responses provided by the connected converters are expected to differ. The

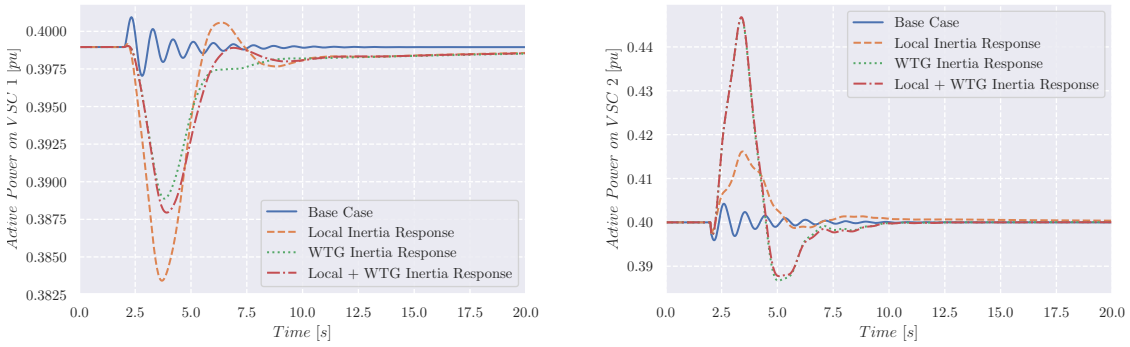
following four case studies are performed under local IE and wide-area ROCOF-based IE:

1. Base Case: No inertia emulation enabled on VSC or WTG;
2. VSC Inertia Response: VSCs are IE-enabled; WTGs are not;
3. WTG Inertia Response: WTGs are IE-enabled; the other VSC is not;
4. VSC + WTG Inertia Response: Both WTGs and VSCs are IE-enabled.

5.4.2 Load Ramping in Area 2

Local Inertia Emulation

Simulation results of active power output, bus frequency, dc voltage, and WTG rotor speed are shown in Figures 5.3 to 5.6.

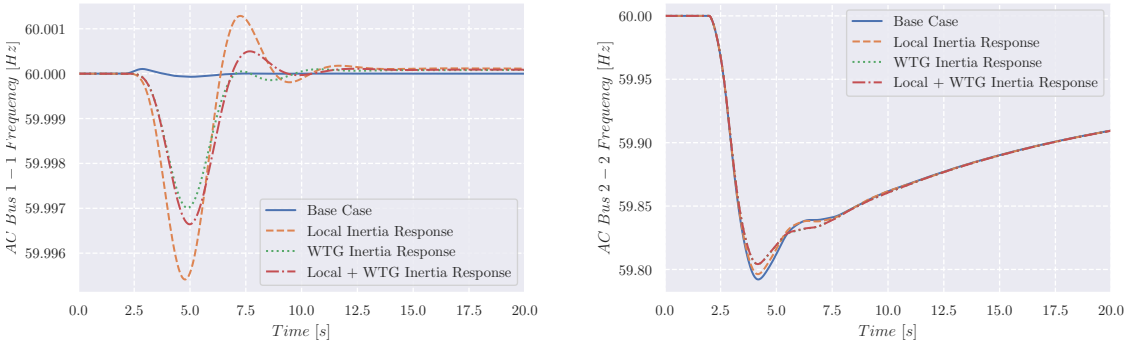


(a) Active power injection of VSC 1 into Bus 1-1 **(b)** Active power injection of VSC 1 into Bus 2-2

Figure 5.3: VSC active power injections under local inertia emulation

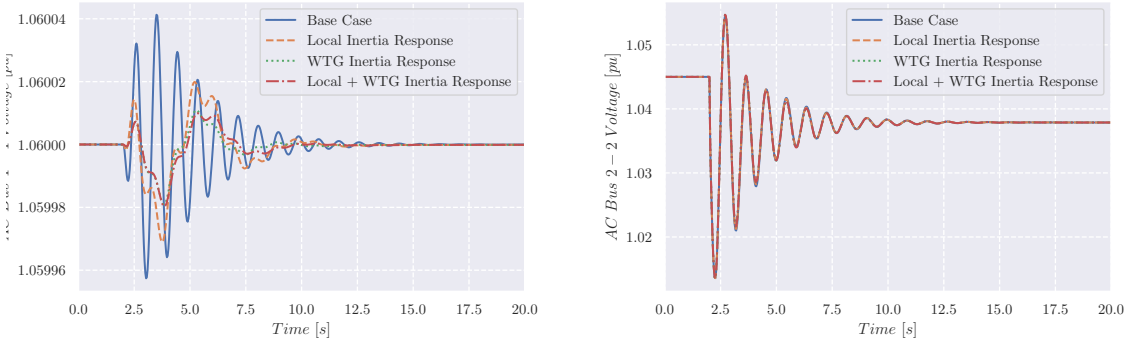
There are six observations from the results:

1. In *Case 1*, the frequency in Area 2 has the lowest nadir because VSC 2 cannot provide inertial support to the load ramping event; the fluctuation of active power on VSC 2 is caused by the fluctuation of the Bus 2-2 voltage.



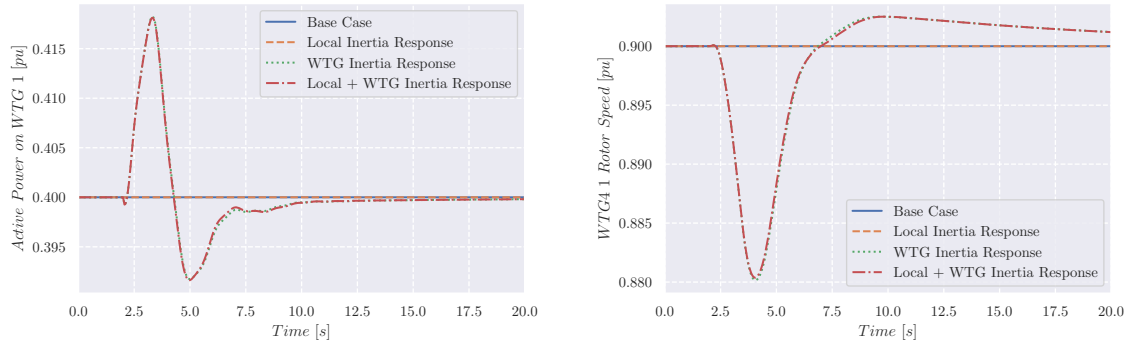
(a) Frequency at Bus 1-1 **(b)** Frequency at Bus 2-2

Figure 5.4: Bus frequency under local inertia emulation



(a) Voltage magnitude at Bus 1-1 **(b)** Voltage magnitude at Bus 2-2

Figure 5.5: Bus voltage magnitude under local IE



(a) WTG power output under local IE **(b)** WTG Rotor Speed under local IE

Figure 5.6: WTG response characteristics under local IE

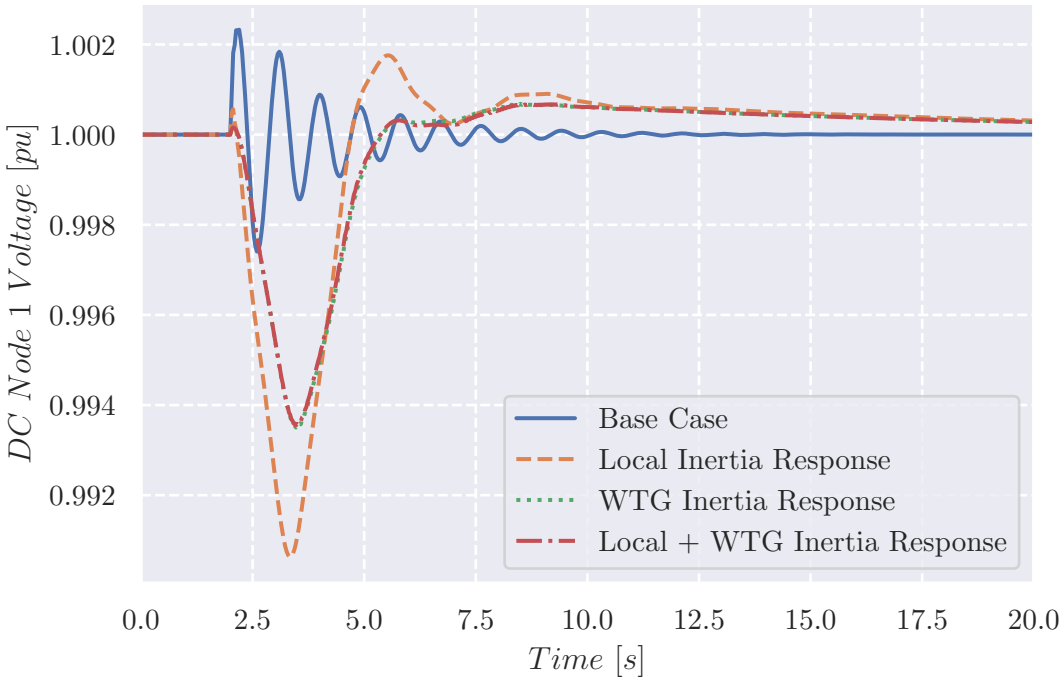


Figure 5.7: DC voltage at Node 1 under local IE

2. In *Case 2*, VSC 2 is able to increase the active power reference based on the local ROCOF. It causes the dc voltage to reduce and incurs extra inertial power supply from VSC 1.

3. In *Case 3*, WTGs are able to reduce the rotor speed to extra inertial power, in response to the dc voltage deviation.

4. In *Cases 3-4*, VSC 2 are able to ramp up active power of the same amount. In both cases, WTGs supplied most of the inertial power to VSC 2.

5. Comparing *Case 2* with *Case 3*, the inertial power supplies from the WTGs are more sufficient and timely.

6. In *Case 4*, since there is adequate inertial support from the WTGs, dc voltage drops less than in *Case 2*. Due to the response from VSC 1, dc voltage drops more than in *Case 3*.

In this scenario, WTGs voluntarily provide inertial support for the load ramping event in Area 2. VSC 1 does not voluntarily provide inertial support, but its dc voltage controller can provide extra power when the dc voltage drops due to VSC 2.

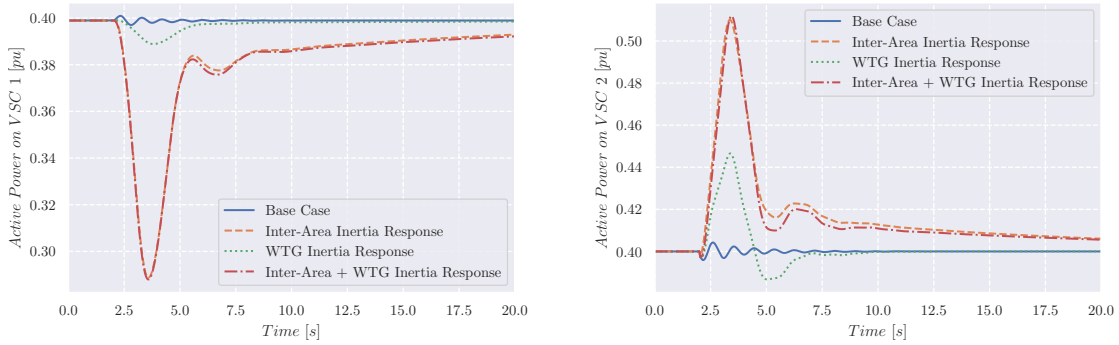
Remote ROCOF based Inertia Emulation

In this case, the ROCOF of Bus 2-2 is transmitted to VSC 1 as a remote signal to improve the inertia response. In Figures 5.8 to 5.11, the following can be observed:

1. *Cases 1 and 3* are identical to the cases in the last subsection. The WTG model and parameters remain the same.

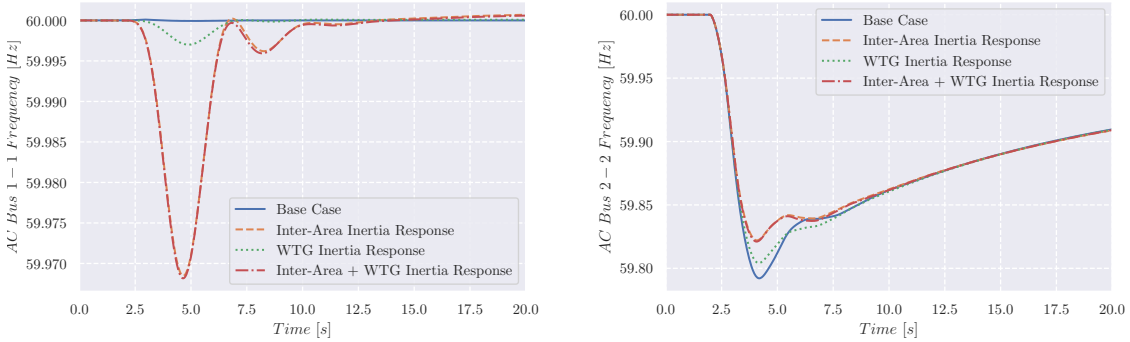
2. In *Cases 2 and 4*, VSC 2 extracts the same peak power for inertial response. VSC 1 is able to able to support inertial power without relying on the dc voltage drop signal.

3. In *Cases 2 and 4*, due to the increased support from VSC 1, the frequency response in Area 2 is increased compared with the local IE methods.



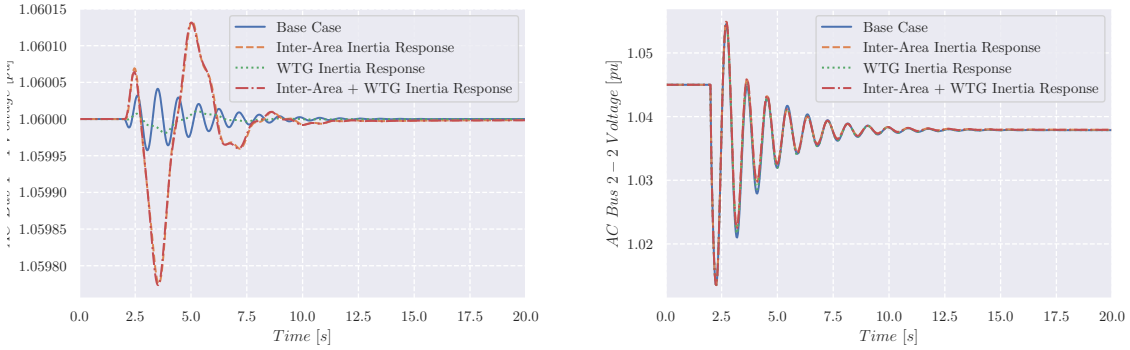
(a) Active power injection of VSC 1 into Bus 1-1 **(b)** Active power injection of VSC 1 into Bus 2-2

Figure 5.8: VSC active power injections under remote inertia emulation



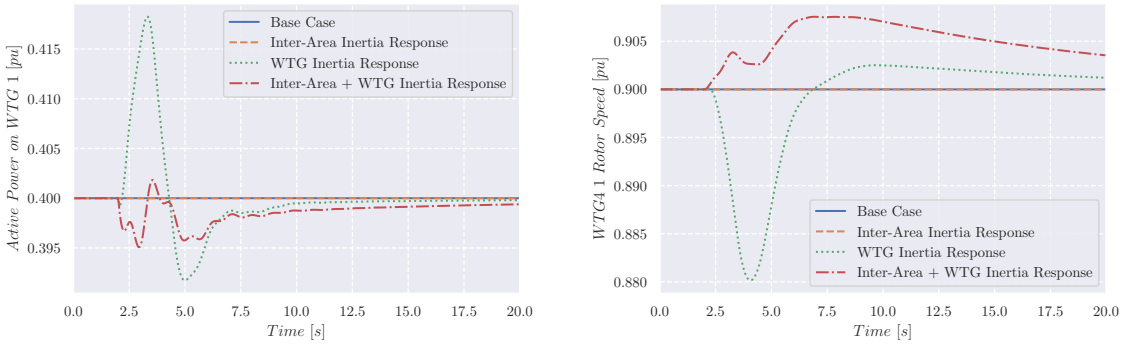
(a) Frequency at Bus 1-1 **(b)** Frequency at Bus 2-2

Figure 5.9: Bus frequency under remote inertia emulation



(a) Voltage magnitude at Bus 1-1 **(b)** Voltage magnitude at Bus 2-2

Figure 5.10: Bus voltage magnitude under remote inertia emulation



(a) WTG power output under remote IE

(b) WTG Rotor Speed under remote IE

Figure 5.11: WTG response characteristics under remote IE

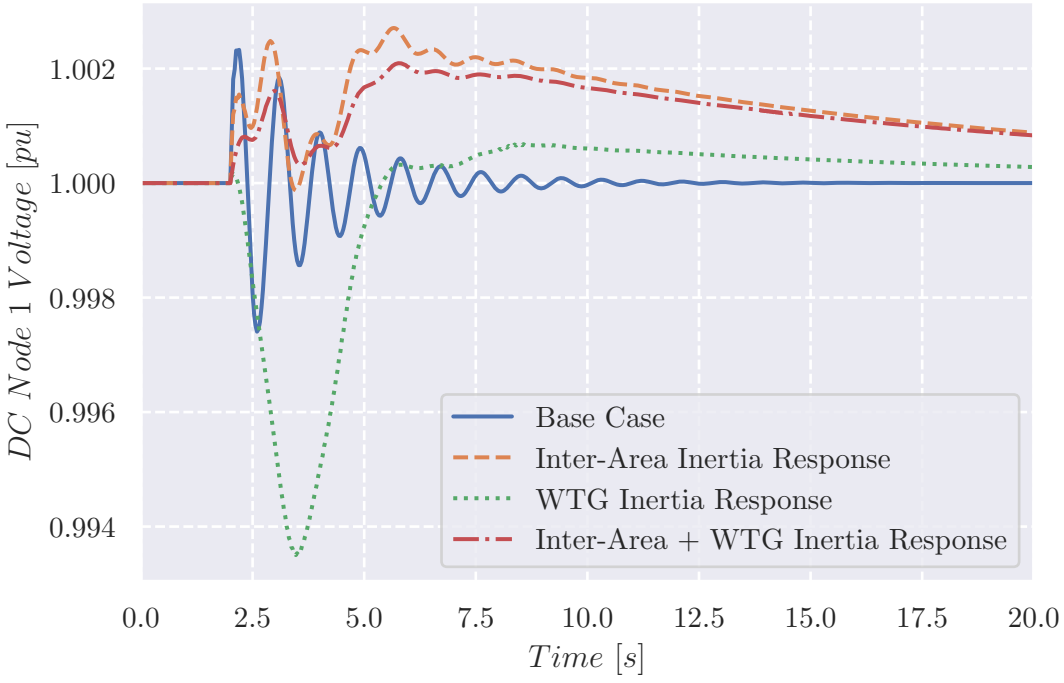


Figure 5.12: DC voltage at Node 1 under remote IE

4. In *Case 4*, since the dc voltage drop is low, inertial support from WTGs are inhibited. Figure 5.11b shows that the WTGs start to accelerate due to the increasing dc voltage and extra power from VSC 1.

The droop of Bus 2-2 ROCOF on dc voltage introduced by VSC 1 can be viewed as a leverage to split the inertia demand between VSC 1 and other sources (the WTGs in these cases). Based on the values of $K_{i,2}$, the following scenarios exist:

1. If $K_{i,2} = 0$ (case 4 under local IE), WTGs will respond to V_{dc} drops due to the inertia power demand on VSC 2. VSC 1 will then compensate for the deficits.

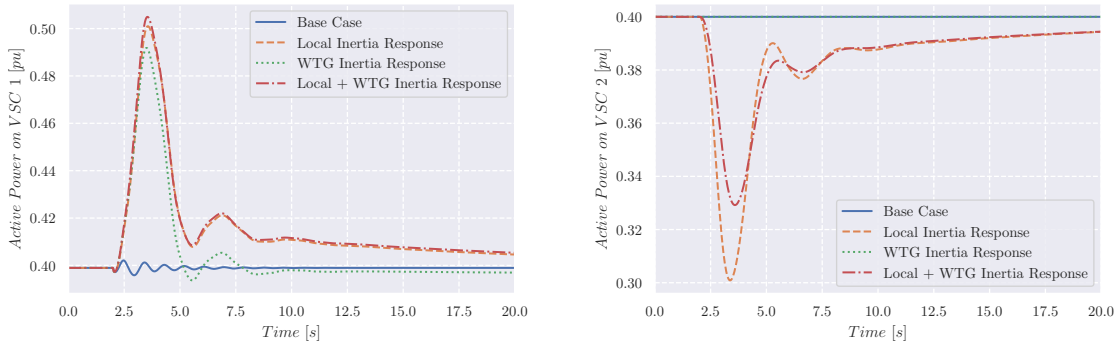
2. If $K_{i,2} \geq 0$, dc voltage will experience a further decline. WTGs will provide more inertia support, but VSC 1 will compete with VSC 2 to withdraw inertial power from the WTGs.

3. If $K_{i,2} \leq 0$, dc voltage will rise. As a result, WTGs will reduce their outputs and VSC 1 will pick up. A limiter should be imposed on the upper dc voltage so that VSC 1 will not be overdrawn. Also needed is a limiter to cap the dc voltage the WTGs should respond to.

To summarize, the inertial response from WTGs requires a decline in the dc voltage, while the inertial response from VSC 1 may, on the other hand, increase the dc voltage. A balance needs to be achieved when leveraging the $ROCOF - V_{dc}$ droop.

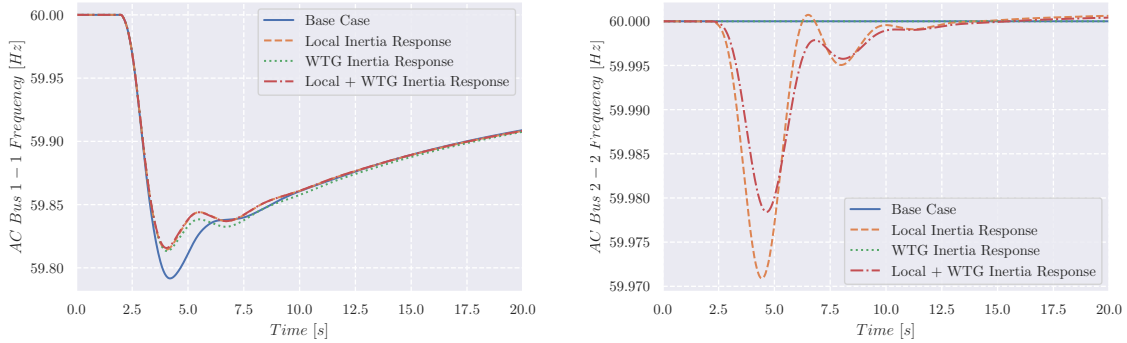
5.4.3 Load Ramping in Area 1

In this subsection, load ramping events on Bus 1-2 in Area 1 is studied. The WTGs can be configured to provide inertial support based on the dc voltage deviation, and VSC 2 can be set to respond to either the local dc voltage signals or the remote ROCOF signal from Area 1. Note that VSC 1 in Area 1 is responsible for controlling the dc voltage, so the theoretical maximum extractable power is determined by VSC 1.



(a) Active power injection of VSC 1 into Bus 1-1 **(b)** Active power injection of VSC 1 into Bus 2-2

Figure 5.13: VSC active power injections under local inertia emulation



(a) Frequency at Bus 1-1 **(b)** Frequency at Bus 2-2

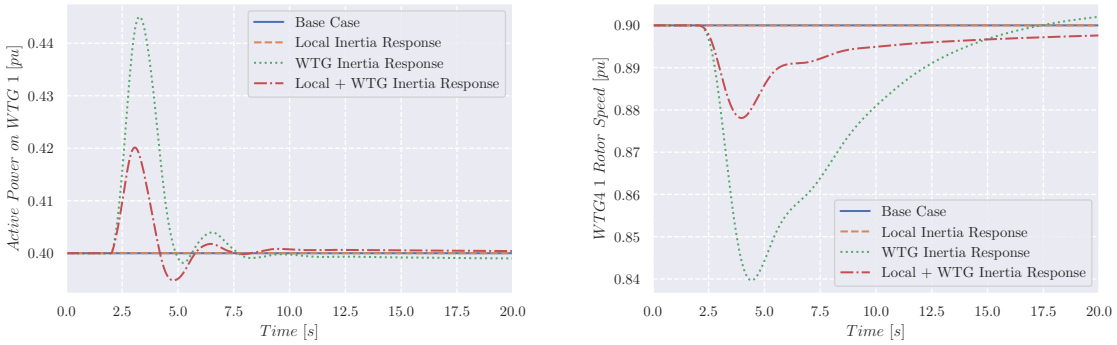
Figure 5.14: Bus frequency under remote local emulation

Local Inertia Emulation

In this simulation case set, VSC 2 can only respond to local dc voltage signals. The results are shown in Figures 5.13 to 5.16. The observations are as follows:

1. In *Cases 2-4*, VSC 2 and WTGs can contribute to the inertial demand by VSC 1, either individually or collectively. The inertial power drawn by VSC 1 in the three cases is close to each other.

2. Comparing *Case 4* with *Case 2*, it is observed that the dc voltage drop can be lowered if VSC 2 and the WTGs collaborate.



(a) WTG power output under local IE

(b) WTG Rotor Speed under local IE

Figure 5.15: WTG response characteristics under local IE

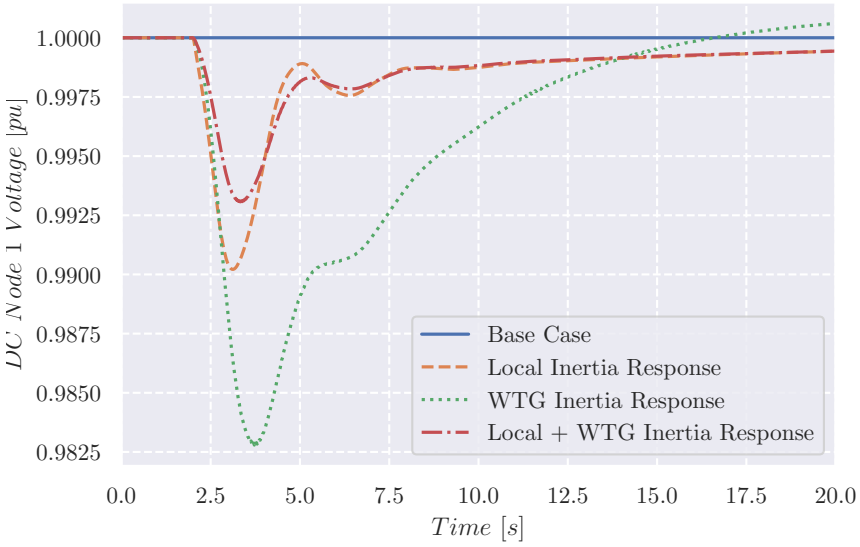
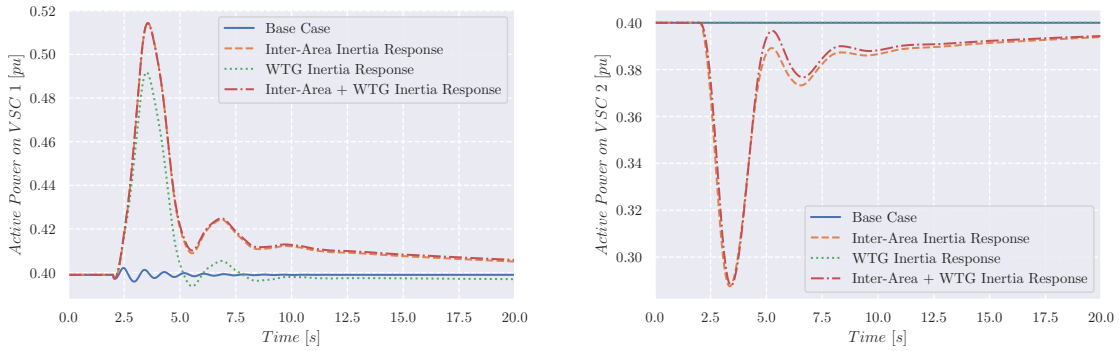


Figure 5.16: DC voltage at Node 1 under local IE

3. The collaboration between the WTGs and VSC 2 reduced the rotor speed reduction at the WTGs and lowered the disturbance to Area 2, when given the same amount of inertial power VSC 1 withdraws.

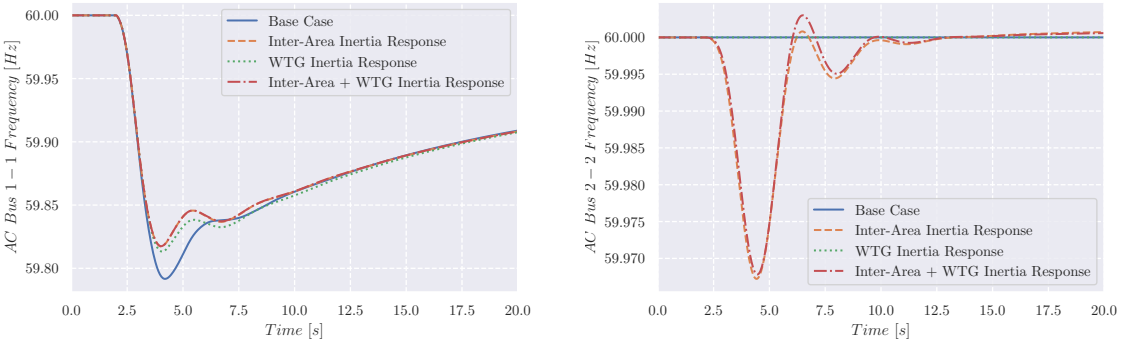
Remote ROCOF-Based Inertia Emulation

In this study, the ROCOF signal of Area 1 is transmitted to VSC 2 as a droop to modify the active power reference. Compared with the studies in the previous subsection, in *Cases 2 and 4*, the dc voltage changes are smaller, and the inertial power ramping at VSC 1 is slightly higher.



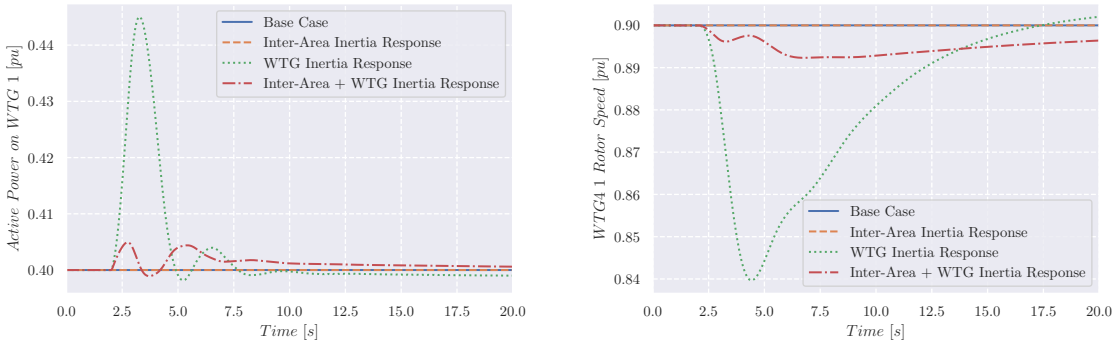
(a) Active power injection of VSC 1 into Bus 1-1 **(b)** Active power injection of VSC 1 into Bus 2-2

Figure 5.17: VSC active power injections under remote inertia emulation



(a) Frequency at Bus 1-1 **(b)** Frequency at Bus 2-2

Figure 5.18: Bus frequency under remote IE



(a) WTG power output under remote IE **(b)** WTG Rotor Speed under remote IE

Figure 5.19: WTG response characteristics under remote IE

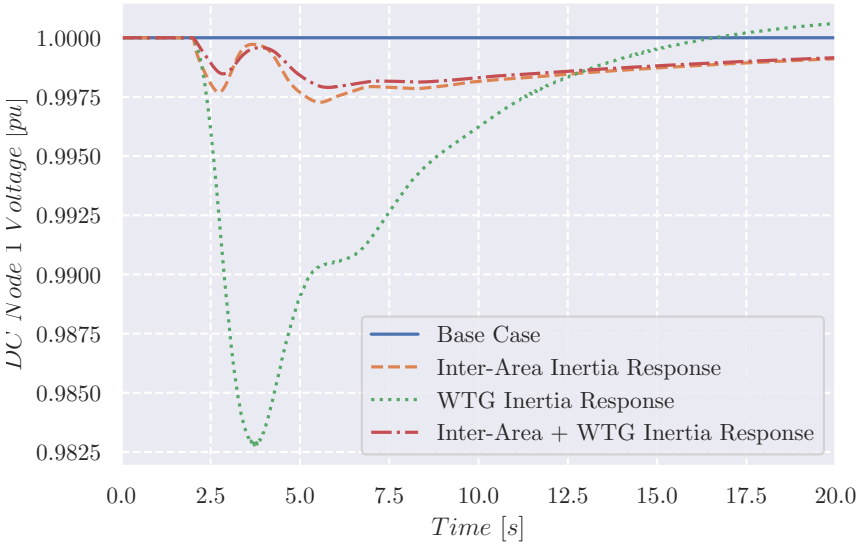


Figure 5.20: DC voltage at Node 1 under remote ROCOF-based IE

The maximum inertial power extracted by VSC 1 can be calculated using (5.33). By substituting in $K_i = 50$, $K_{p3} = 1$ and observing the ROCOF at Bus 1-1 in Figure 5.21, the estimated maximum inertial power is

$$\Delta P_{VSC1} = K_i K_{p3} \frac{df_1}{dt} = 0.1 \; pu \tag{5.42}$$

which can approximate the maximum power extraction, $\Delta P_{VSC1} = 0.11$, shown in Figure 5.17a.

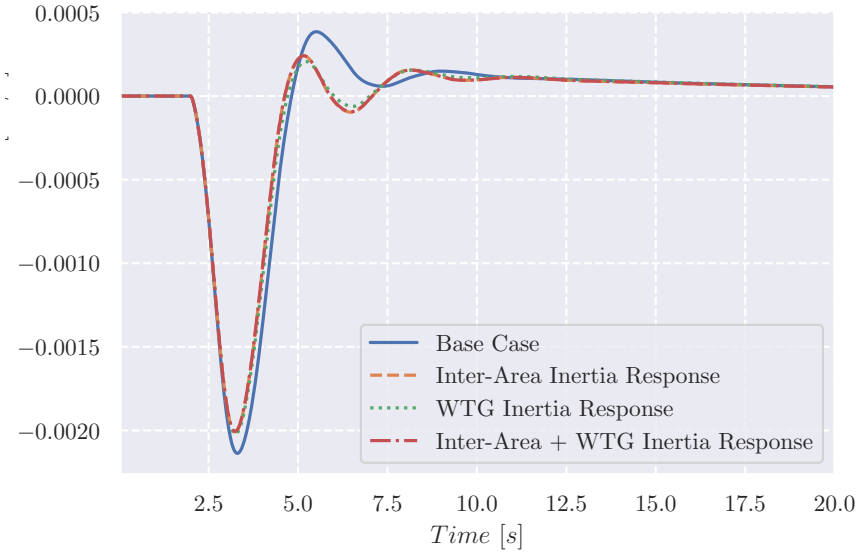


Figure 5.21: ROCOF at Bus 1-1 under Area 1 load ramping with remote ROCOF-based IE

By observing the valley dc voltage difference of Case 3 and Case 4 as shown in Figure 5.16, the reduced dc voltage between *Cases 2 and 3* when ROCOF is at its nadir can be calculated using (5.38) by substituting in $K_i = 50$, $K_{p3} = 1$, $K_{dc3} = K_{dc4} = 10$, and $I_{dc1} = 0.4$, yielding

$$\Delta V_{dc} = \frac{K_{p3} K_i}{\sum_{j=2}^{n} K_{dcj} + I_{dc1}} \times \frac{df_1}{dt} = \frac{-0.1}{20.4} = -0.0049 \tag{5.43}$$

which can approximate the actual voltage drop $\Delta V_{dc} = 0.9902 - 0.9856 = 0.00465$ at $t = 3.13\ s$

5.5 Conclusion

This chapter presented an application of using multi-terminal dc for integrating offshore wind generation. Type IV PMSG wind generator model with inertial emulation is proposed. A four-terminal dc system that connects two onshore ac grids and two offshore wind farms are studied. Estimation for the extracted inertial power by the VSC controlling the dc voltage is provided, along with an estimation of dc voltage drop.

Case studies verify the inertial support capability of the Type IV wind generators. Also verified is the capability of extracting the inertial power of the converters through the dc network.

Chapter 6

Conclusions

6.1 Main Contributions and Conclusions

This dissertation consists of four main parts: 1) the architecture, design, and implementation of a large-scale cyber-physical power system testbed, 2) Newton power flow methods with the inclusion of multi-terminal HVDC and its control handling, 3) dc network and VSC converter models for transient simulations with inertia emulation, and 4) integration of offshore wind farms with inertial and primary frequency support through MTDC

Chapter 2 proposes the design and implementation of a testbed for wide-area measurement-based control using open-source software. The testbed consists of a data streaming interface for linking simulations, measurements, EMS, and control modules. The platform features a unified data interface, which enables exchangeability between modules of the same functionality. Further, an open-source Python-based transient simulation tool, ANDES, is developed and interfaced to the testbed.

Chapter 3 models the dc network and VSC in the Newton power flow iterations. An extended formulation to include the control set points and automatically enforce the control limits is proposed. By including the set point equations in the simultaneous power flow solution process, the values of the controlled variables, such

as terminal voltages or throughput current, can be checked at each iteration and set to the limits when applicable.

Chapter 4 models the dynamic components in the HVDC transmission networks with representations of dc resistance, inductance, and capacitance. Two types of VSCs that are controlled as a current source or voltage source are modeled for positive-sequence transient simulation. In addition, inertia emulation control loops are modeled for each type of VSC. Case studies show that the converters are able to provide inertial support to the ac grid, although their response characteristics differ. Therefore, the dc voltage controller gains must be tuned accordingly to ensure adequate response and maintain dc voltage.

Chapter 5 presents offshore wind farms, with Type IV wind generators, namely, the PMSG with ac voltage control and power control, connected through a multi-terminal dc network. Inertial emulation controllers are modeled to modify the power reference and provide inertial power by decelerating the turbine. Furthermore, dc-voltage droop based local information and remote ROCOF-based information are compared. Estimation of the maximum extractable inertial power and estimated dc voltage droop due to inadequate response are proposed.

6.2 Future Research Directions

Continuation of the research proposed in this dissertation can be carried out in the following directions:

1. The integration of software-defined communication networks with the power simulator can continue. Modeling the existing communication infrastructure for power substations and the supporting communication protocols helps examine the impact of cyber-space events on the physical system. Further, cybersecurity research using the testbed can be carried out within substations, between substations and control centers, and within the control center.

2. The voltage-source type VSC can be modeled with more details, including the overcurrent limiters that are critical for fault scenarios. The stability of the voltage-source type VSC can be further studied by examining angular stability, namely, the synchronization characteristics that are affected by the control parameters.

Bibliography

[1] A. Abur and A. Rouhani. Linear Phasor Estimator Assisted Dynamic State Estimation. *IEEE Transactions on Smart Grid*, 3053(99):1–1, 2016. ISSN 1949-3053. doi: 10.1109/TSG.2016.2548244. URL http://ieeexplore.ieee.org/lpdocs/epic03/wrapper.htm?arnumber=7445210. 29

[2] U. Adhikari, T. H. Morris, and S. Pan. A cyber-physical power system test bed for intrusion detection systems. *2014 IEEE PES General Meeting*, pages 1–5, 2014. ISSN 1932-5517. doi: 10.1109/PESGM.2014.6939262. URL http://ieeexplore.ieee.org/lpdocs/epic03/wrapper.htm?arnumber=6939262. 9

[3] D. Antonioli and N. O. Tippenhauer. MiniCPS: A toolkit for security research on CPS Networks. In *Proceedings of the First ACM Workshop on Cyber-Physical Systems-Security and/or Privacy*, pages 91–100, 2015. ISBN 9781450338271. doi: 10.1145/2808705.2808715. URL http://arxiv.org/abs/1507.04860. 9

[4] A. Ashok, A. Hahn, and M. Govindarasu. A Cyber-Physical Security testbed for Smart Grid : System Architecture and Studies. *Proceedings of the Seventh Annual Workshop on Cyber Security and Information Intelligence Research. ACM, 2011.*, page 20, 2011. doi: 10.1145/2179298.2179320. 9

[5] A. Ashok, S. Krishnaswamy, and M. Govindarasu. PowerCyber: A remotely accessible testbed for Cyber Physical security of the Smart Grid. *2016 IEEE Power and Energy Society Innovative Smart Grid Technologies Conference, ISGT 2016*, 2016. doi: 10.1109/ISGT.2016.7781277. 9

[6] L. Bai, F. Li, H. Cui, T. Jiang, H. Sun, and J. Zhu. Interval optimization based operating strategy for gas-electricity integrated energy systems considering demand response and wind uncertainty. *Applied Energy*, 167:270–279, 2015. ISSN 03062619. doi: 10.1016/j.apenergy.2015.10.119. 2

[7] J. Beerten and R. Belmans. Modeling and control of Multi-terminal VSC HVDC systems. *Energy Procedia*, 24:123–130, 2012. ISSN 18766102. doi: 10.1016/

j.egypro.2012.06.093. URL http://dx.doi.org/10.1016/j.egypro.2012.06.093. 59

[8] D. C. Bergman, D. Jin, D. M. Nicol, and T. Yardley. The virtual power system testbed and inter-testbed integration. *Proceedings of the 2nd conference on Cyber security experimentation and test*, (August):5, 2009. 10

[9] BetterGrids.org. CURENT North American Grid, 2018. URL https://db.bettergrids.org/bettergrids/handle/1001/414. 51

[10] D. Bian, M. Kuzlu, M. Pipattanasomporn, S. Rahman, and Y. Wu. Real-time co-simulation platform using OPAL-RT and OPNET for analyzing smart grid performance. In *IEEE Power and Energy Society General Meeting*, volume 2015-Septe, 2015. ISBN 9781467380409. doi: 10.1109/PESGM.2015.7286238. 10

[11] D. P. Chassin, K. Schneider, and C. Gerkensmeyer. GridLAB-D: An Open-source Power Systems Modelling and Simulation Environment. *Transmission and Distribution Conference and Exposition*, pages 1–5, 2008. ISSN 9781424419043. doi: 10.1109/TDC.2008.4517260. URL http://ieeexplore.ieee.org.ezproxy.lib.purdue.edu/xpl/articleDetails.jsp?arnumber=4517260. 7

[12] N. R. Chaudhuri and B. Chaudhuri. Adaptive droop control for effective power sharing in multi-terminal DC (MTDC) grids. *IEEE Transactions on Power Systems*, 28(1):21–29, 2013. ISSN 08858950. doi: 10.1109/TPWRS.2012.2203390. 12

[13] S. Cole and R. Belmans. Matdyn, a new matlab-based toolbox for power system dynamic simulation. *IEEE Transactions on Power systems*, 26(3):1129–1136, 2011. 5

[14] S. Cole, J. Beerten, and R. Belmans. Generalized dynamic VSC MTDC model for power system stability studies. *IEEE Transactions on Power Systems*, 25(3):1655–1662, 2010. 12

[15] H. Cui. ANDES - A Python-based tool for power system research, 2016. URL https://github.com/cuihantao/andes. 5

[16] H. Cui and F. Li. ANDES : A Python-Based Cyber-Physical Power System Simulation Tool. In *North American Power Symposium*, pages 1–5, 2018. 5

[17] H. Cui, R. Long, F. Li, X. Fang, and R. Long. Distribution Network Reconfiguration with Aggregated Electric Vehicle Charging Strategy. In *IEEE Power and Energy Society General Meeting*, volume 2015-Septe, pages 1–5, 2015. ISBN 9781467380409. doi: 10.1109/PESGM.2015.7285650. 11

[18] H. Cui, F. Li, Q. Hu, L. Bai, and X. Fang. Day-ahead coordinated operation of utility-scale electricity and natural gas networks considering demand response based virtual power plants. *Applied Energy*, 2016. ISSN 03062619. doi: 10.1016/j.apenergy.2016.05.007. 2, 47

[19] H. Cui, F. Li, and H. Yuan. Control and Limit Enforcements for VSC Multi-Terminal HVDC in Newton Power Flow. In *IEEE PES General Meeting 2017*, pages 1–5, 2017. URL http://arxiv.org/abs/1703.07231. 44

[20] H. Cui, F. Li, X. Fang, H. Chen, and H. Wang. Bilevel Arbitrage Potential Evaluation for Grid-Scale Energy Storage Considering Wind Power and LMP Smoothing Effect. *IEEE Transactions on Sustainable Energy*, 2018. ISSN 19493029. doi: 10.1109/TSTE.2017.2758378. 13

[21] T. A. Davis. *Direct Methods for Sparse Linear Systems*. Society for Industrial and Applied Mathematics, 2006. ISBN 9780898716139. 6

[22] X. Dong, H. Lin, R. Tan, R. K. Iyer, and Z. Kalbarczyk. Software-Defined Networking for Smart Grid Resilience: Opportunities and Challenges. *Proceedings of the 1st ACM Workshop on Cyber-Physical System Security*, pages 61–68, 2015. doi: 10.1145/2732198.2732203. URL http://doi.acm.org/10.1145/2732198.2732203. 10, 23

[23] N. Duan and K. Sun. Application of the adomian decomposition method for semi-analytic solutions of power system differential algebraic equations. In *2015 IEEE Eindhoven PowerTech, PowerTech 2015*, 2015. ISBN 9781479976935. doi: 10.1109/PTC.2015.7232370. 5

[24] R. C. Dugan and T. E. McDermott. An open source platform for collaborating on smart grid research. *IEEE Power and Energy Society General Meeting*, (Ivvc): 1–7, 2011. ISSN 19449925. doi: 10.1109/PES.2011.6039829. 7

[25] X. Fang, F. Li, Y. Wei, and H. Cui. Strategic scheduling of energy storage for load serving entities in locational marginal pricing market. *IET Generation, Transmission and Distribution*, 10(5):1258–1267, 2016. ISSN 17518687. doi: 10.1049/iet-gtd.2015.0144. 2

[26] C. Fu, J. D. McCalley, and J. Tong. A numerical solver design for extended-term time-domain simulation. *IEEE Transactions on Power Systems*, 28(4): 4926–4935, 2013. ISSN 08858950. doi: 10.1109/TPWRS.2011.2177674. 7

[27] U. Ghosh, X. Dong, R. Tan, and Z. Kalbarczyk. A Simulation Study on Smart Grid Resilience under Software-Defined Networking Controller Failures. In *CPSS'16*, pages 52–58, 2016. ISBN 9781450342889. doi: 10.1145/2899015.2899020. URL http://dl.acm.org/citation.cfm?id=2899020. 10

[28] M. Guan, W. Pan, J. Zhang, and Q. Hao. Synchronous Generator Emulation Control Strategy for Voltage Source Converter (VSC) Stations. *IEEE Trans. on Power Syst.*, 30(1):1–9, 2015. doi: 10.1109/TPWRS.2014.2384498. 67

[29] A. Hahn, A. Ashok, S. Sridhar, and M. Govindarasu. Cyber-physical security testbeds: Architecture, application, and evaluation for smart grid. *IEEE Transactions on Smart Grid*, 4(2):847–855, 2013. ISSN 19493053. doi: 10.1109/TSG.2012.2226919. 9

[30] C. Hannon, J. Yan, and D. Jin. DSSnet. In *Proceedings of the 2016 annual ACM Conference on SIGSIM Principles of Advanced Discrete Simulation - SIGSIM-PADS '16*, pages 131–142, 2016. ISBN 9781450337427. doi: 10.1145/2901378.2901383. URL http://dl.acm.org/citation.cfm?id=2901378.2901383http://dl.acm.org/citation.cfm?doid=2901378.2901383. 9

[31] A. C. Hindmarsh, P. N. Brown, K. E. Grant, S. L. Lee, R. Serban, D. E. Shumaker, and C. S. Woodward. Sundials. *ACM Transactions on Mathematical Software*, 31(3):363–396, 2005. ISSN 00983500. doi: 10.1145/1089014.1089020. URL http://portal.acm.org/citation.cfm?doid=1089014.1089020. 6, 28

[32] M. D. Ilić, L. Xie, U. A. Khan, and J. M. F. Moura. Modeling future cyber-physical energy systems. *IEEE Power and Energy Society 2008 General Meeting: Conversion and Delivery of Electrical Energy in the 21st Century, PES*, 2008. ISSN 1932-5517. doi: 10.1109/PES.2008.4596708. 9

[33] B. M. Kelley, P. Top, S. G. Smith, C. S. Woodward, and L. Min. A federated simulation toolkit for electric power grid and communication network co-simulation. In *2015 Workshop on Modeling and Simulation of Cyber-Physical Energy Systems (MSCPES)*, pages 1–6. IEEE, 2015. 5, 7

[34] A. Kirakosyan, E. F. El-Saadany, M. S. E. Moursi, S. Acharya, and K. A. Hosani. Control Approach for the Multi-Terminal HVDC System for the Accurate Power Sharing. *IEEE Transactions on Power Systems*, 33(4):4323–4334, 2018. ISSN 08858950. doi: 10.1109/TPWRS.2017.2786702. 12

[35] J. Kleissl and Y. Agarwal. Cyber-physical energy systems: Focus on smart buildings. *Design Automation Conference (DAC), 2010 47th ACM/IEEE*, pages 749–754, 2010. ISSN 0738-100X. doi: 10.1145/1837274.1837464. 10

[36] D. Kundur, X. Feng, S. Liu, T. Zourntos, and K. L. Butler-Purry. Towards a framework for cyber attack impact analysis of the electric smart grid.

SmartGridComm'2010, pages 244–249, 2010. doi: 10.1109/SMARTGRID.2010.5622049. 10

[37] B. Lantz, B. Heller, and N. McKeown. A network in a laptop: rapid prototyping for software-defined networks. In *Proc. of the 9th ACM SIGCOMM Workshop on Hot Topics in Networks*, page 19. ACM, 2010. 28

[38] H. Li, C. Liu, G. Li, and R. Iravani. An Enhanced DC Voltage Droop-Control for the VSC-HVDC Grid. *IEEE Transactions on Power Systems*, 32(2):1520–1527, 2016. ISSN 0885-8950. doi: 10.1109/TPWRS.2016.2576901. URL http://ieeexplore.ieee.org/lpdocs/epic03/wrapper.htm?arnumber=7484690. 12

[39] X. Li, F. Li, H. Yuan, H. Cui, and Q. Hu. GPU-Based Fast Decoupled Power Flow with Preconditioned Iterative Solver and Inexact Newton Method. *IEEE Transactions on Power Systems*, 32(4):2695–2703, 2017. ISSN 08858950. doi: 10.1109/TPWRS.2016.2618889. 7

[40] H. Lin, S. S. Veda, S. S. Shukla, L. Mili, and J. Thorp. GECO: Global event-driven co-simulation framework for interconnected power system and communication network. *IEEE Transactions on Smart Grid*, 3(3):1444–1456, 2012. ISSN 19493053. doi: 10.1109/TSG.2012.2191805. 9

[41] H. Lin, C. Chen, J. Wang, S. Member, J. Qi, and D. Jin. Self-Healing Attack-Resilient PMU Network for Power System Operation. *IEEE Transactions on Smart Grid*, PP(99), 2016. ISSN 1949-3053. doi: 10.1109/TSG.2016.2593021. 10

[42] Y. Ma, L. Yang, J. Wang, F. Wang, and L. M. Tolbert. Emulating full-converter wind turbine by a single converter in a multiple converter based emulation system. *Conference Proceedings - IEEE Applied Power Electronics Conference and Exposition - APEC*, pages 3042–3047, 2014. doi: 10.1109/APEC.2014.6803738. 81

[43] F. Milano. PSAT Power System Analysis Toolbox. page 446, 2008. URL http://faraday1.ucd.ie/psat.html. 5

[44] F. Milano. *Power system modelling and scripting*. Springer Science & Business Media, 2010. 5, 44, 48, 77

[45] F. Milano. A python-based software tool for power system analysis. In *IEEE Power and Energy Society General Meeting*, 2013. ISBN 9781479913039. doi: 10.1109/PESMG.2013.6672387. 5

[46] F. Milano. Semi-Implicit Formulation of Differential-Algebraic Equations for Transient Stability Analysis. *IEEE Transactions on Power Systems*, 31(6):4534–4543, 2016. ISSN 08858950. doi: 10.1109/TPWRS.2016.2516646. 5

[47] J. Morren, S. W. H. de Haan, W. L. Kling, and J. A. Ferreira. Wind turbines emulating inertia and supporting primary frequency control. *IEEE Transactions on Power Systems*, 21(1):433–434, 2006. ISSN 08858950. doi: 10.1109/TPWRS.2005.861956. 66

[48] T. H. Morris, A. K. Srivastava, B. Reaves, K. Pavurapu, S. Abdelwahed, R. Vaughn, W. McGrew, and Y. Dandass. Engineering future cyber-physical energy systems: Challenges, research needs, and roadmap. *41st North American Power Symposium, NAPS*, pages 1–6, 2009. doi: 10.1109/NAPS.2009.5484019. URL http://ieeexplore.ieee.org/xpls/abs{_}all.jsp?arnumber=5484019. 10

[49] S. Muyeen, R. Takahashi, T. Murata, and J. Tamura. A Variable Speed Wind Turbine Control Strategy to Meet Wind Farm Grid Code Requirements. *IEEE Transactions on Power Systems*, 25(1):331–340, 2010. ISSN 0885-8950. doi: 10.1109/TPWRS.2009.2030421. 67

[50] OpenElectrical. Power Systems Analysis Software, 2016. URL http://www.openelectrical.org/wiki/index.php?title=Power{_}Systems{_}Analysis{_}Software. 27

[51] M. A. Pai and P. W. Sauer. Stability Analysis of Power Systems by Lyapunov's Direct Method. *IEEE Control Systems Magazine*, 9(1):23–27, 1989. ISSN 02721708. doi: 10.1109/37.16746. 4

[52] P. Palensky, E. Widl, and A. Elsheikh. Simulating Cyber-Physical Energy Systems: Challenges, Tools and Methods. *IEEE Transactions on Systems, Man, and Cybernetics: Systems*, 44(3):318–326, 2014. ISSN 10834427. doi: 10.1109/TSMCC.2013.2265739. 10

[53] D. Ramasubramanian, Z. Yu, R. Ayyanar, V. Vittal, and J. Undrill. Converter Model for Representing Converter Interfaced Generation in Large Scale Grid Simulations. *IEEE Transactions on Power Systems*, 32(1):1–1, 2016. ISSN 0885-8950. doi: 10.1109/TPWRS.2016.2551223. URL http://ieeexplore.ieee.org/document/7448458/. 12

[54] J. Rocabert, A. Luna, F. Blaabjerg, and P. Rodríguez. Control of power converters in AC microgrids. *IEEE Transactions on Power Electronics*, 27(11): 4734–4749, nov 2012. ISSN 08858993. doi: 10.1109/TPEL.2012.2199334. URL http://ieeexplore.ieee.org/document/6200347/. 54

[55] Q. Shi, H. Cui, and F. Li. A Hybrid Dynamic Demand Control Strategy for Power System Frequency Regulation. *Csee*, 3(2):176–185, 2017. doi: 10.17775/CSEEJPES.2017.0022. 10, 66

[56] Q. Shi, F. Li, Q. Hu, and Z. Wang. Dynamic demand control for system frequency regulation: Concept review, algorithm comparison, and future vision. *Electric Power Systems Research*, 154:75–87, 2018. 3

[57] Q. Shi, F. F. Li, and H. Cui. Analytical Method to Aggregate Multi-Machine SFR Model with Applications in Power System Dynamic Studies. *IEEE Transactions on Power Systems*, 8950(c):1–12, 2018. ISSN 08858950. doi: 10.1109/TPWRS.2018.2824823. 67

[58] B. Silva, C. L. Moreira, L. Seca, Y. Phulpin, and J. A. Lopes. Provision of inertial and primary frequency control services using offshore multiterminal HVDC networks. *IEEE Transactions on Sustainable Energy*, 3(4):800–808, oct 2012. ISSN 19493029. doi: 10.1109/TSTE.2012.2199774. URL http://ieeexplore.ieee.org/document/6213587/. 79, 81

[59] S. Sridhar, A. Hahn, and M. Govindarasu. Cyber-physical system security for the electric power grid. *Proceedings of the IEEE*, 100(1):210–224, 2012. ISSN 00189219. doi: 10.1109/JPROC.2011.2165269. 10

[60] G. Stamatiou and M. Bongiorno. Power-dependent droop-based control strategy for multi-terminal HVDC transmission grids. *IET Generation, Transmission & Distribution*, oct 2016. ISSN 1751-8687. doi: 10.1049/iet-gtd.2016.0764. URL http://digital-library.theiet.org/content/journals/10.1049/iet-gtd.2016.0764. 12

[61] B. Stott. Power system dynamic response calculations. *Proceedings of the IEEE*, 67(2):219–241, 1979. ISSN 0018-9219. doi: 10.1109/PROC.1979.11233. URL http://ieeexplore.ieee.org/xpls/abs{_}all.jsp?arnumber=1455502. 5

[62] C.-C. Sun, C.-C. Liu, and J. Xie. Cyber-Physical System Security of a Power Grid: State-of-the-Art. *Electronics*, 5(3):40, 2016. ISSN 2079-9292. doi: 10.3390/electronics5030040. URL http://www.mdpi.com/2079-9292/5/3/40. 10

[63] K. Sun, K. Hur, and P. Zhang. A new unified scheme for controlled power system separation using synchronized phasor measurements. *IEEE Transactions on Power Systems*, 26(3):1544–1554, 2011. 30

[64] K. Tomsovic, D. E. Bakken, V. Venkatasubramanian, and A. Bose. Designing the next generation of real-time control, communication, and computations for large power systems. *Proceedings of the IEEE*, 93(5):965–979, 2005. ISSN 00189219. doi: 10.1109/JPROC.2005.847249. 9

[65] L. Vanfretti, T. Rabuzin, M. Baudette, and M. Murad. iTesla Power Systems Library (iPSL): A Modelica library for phasor time-domain simulations. *SoftwareX*, 2016. 8

[66] S. Wang and K. Tomsovic. A Novel Active Power Control Framework for Wind Turbine Generators to Improve Frequency Response. *IEEE Transactions on Power Systems*, 8950(c):1–11, 2018. ISSN 08858950. doi: 10.1109/TPWRS.2018.2829748. 78

[67] H. Yuan, X. Li, F. Li, X. Fang, H. Cui, and Q. Hu. Mitigate Overestimation of Voltage Stability Margin by Coupled Single-Port Circuit Models. In *IEEE Power and Energy Society General Meeting*, volume 2016-Novem, pages 1–5, 2016. ISBN 9781509041688. doi: 10.1109/PESGM.2016.7741515. 30

[68] L. Zhang, L. Harnefors, and H. P. Nee. Power-synchronization control of grid-connected voltage-source converters. *IEEE Transactions on Power Systems*, 25 (2):809–820, 2010. ISSN 08858950. doi: 10.1109/TPWRS.2009.2032231. 63

[69] Y. Zhang, M. E. Raoufat, and K. Tomsovic. Remedial Action Schemes and Defense Systems. *Smart Grid Handbook*, pages 1–10, 2016. doi: 10.1002/9781118755471.sgd032. URL http://doi.wiley.com/10.1002/9781118755471.sgd032. 25

[70] Y. Zhang, A. Melin, S. Djouadi, and M. Olama. Performance guaranteed inertia emulation for diesel-wind system feed microgrid via model reference control. In *2017 IEEE Power and Energy Society Innovative Smart Grid Technologies*

Conference, ISGT 2017, 2017. ISBN 9781538628904. doi: 10.1109/ISGT.2017.8085976. 67

[71] Y. Zhang, A. Melin, S. M. Djouadi, M. Olama, and K. Tomsovic. Provision for Guaranteed Inertial Response in Diesel-Wind Systems via Model Reference Control. *IEEE Transactions on Power Systems*, 8950(c):1–11, 2018. ISSN 08858950. doi: 10.1109/TPWRS.2018.2827205. 79

[72] J. Zhao, L. Zhan, Y. Liu, H. Qi, J. R. Garcia, and P. D. Ewing. Measurement accuracy limitation analysis on synchrophasors. In *2015 IEEE Power & Energy Society General Meeting*, pages 1–5. IEEE, 2015. 23

[73] R. D. Zimmerman, C. E. Murillo-Sanchez, and R. J. Thomas. MATPOWER: Steady-State Operations, Planning, and Analysis Tools for Power Systems Research and Education. *IEEE Transactions on Power Systems*, 26(1):12–19, 2011. ISSN 0885-8950. doi: 10.1109/TPWRS.2010.2051168. URL http://ieeexplore.ieee.org/lpdocs/epic03/wrapper.htm?arnumber=5491276. 5

Appendix

Appendix A

Publications During Ph.D. Study

A.1 Journal Papers

1. **Hantao Cui**, Fangxing Li, Xin Fang and et. al, "Bi-Level Arbitrage Potential Evaluation for Grid-Scale Energy Storage Considering Wind Power and LMP Smoothing Effect", IEEE Transactions on Sustainable Energy, vol. 9, no. 2, pp. 707-718, Apr. 2018.

2. **Hantao Cui**, Fangxing Li, Qinran Hu and et. al, "Day-ahead coordinated operation of utility-scale electricity and natural gas networks considering demand response base virtual power plants", Applied Energy, 2016, 176 (15), 183-195.

3. Linquan Bai, Fangxing Li, **Hantao Cui** and et.al, "Interval Optimization based Operating Strategy for Gas-Electricity Integrated Energy Systems Considering Demand Response and Wind Uncertainty," Applied Energy (Elsevier), vol. 167, pp. 270-279, Apr. 2016.

A.2 Conference Papers

1. **Hantao Cui**, Fangxing Li, "ANDES: A Python-Based Cyber-Physical Power System Simulation Tool", 2018 North America Power Symposim, Fargo, Sep 2018.

2. **Hantao Cui**, Fangxing Li, Haoyu Yuan, "Control and Limit Enforcement for VSC Multi-Terminal HVDC in Newton Power Flow", 2017 Power & Energy Society General Meeting (PES GM 2017), Chicago, July 2017.

3. **Hantao Cui**, Fangxing Li, Xin Fang and Runsha Long, "Distribution Network Reconfiguration with Aggregated Electric Vehicle Charging Strategy", 2015 Power & Energy Society General Meeting (PES GM 2015), Denver, Colorado, July 2015.

A.3 Patent Applications

1. Li, Fangxing, **Hantao Cui**, MohammadReza AhmadzadehRaji and et. al, "Real-time simulator and controller of power system using distributed data streaming server." U.S. Patent Application 15/457,428, filed September 13, 2018.

Vitae

Hantao Cui was born in Lichuan, Jiangxi, China, on 17 April 1991. He received both his B.S. degree (with honors) and M.S. degree from Southeast University, Nanjing, China, in 2011 and 2013. He joined the University of Tennessee, Knoxville in August 2013 to pursue his Ph.D. degree in Electrical Engineering. He became a full-time research associate with Center for Ultra-Wide-Area Resilient Energy Transmission Networks (CURENT) at the University of Tennessee, Knoxville, in January 2017. His research interests include computer applications in power systems, cyber-physical system modeling, and high performance computing.